Measurement of the strange quark forward-backward asymmetry around the Z^0 peak

ACADEMISCH PROEFSCHRIFT

TER VERKRIJGING VAN DE GRAAD VAN DOCTOR AAN DE
UNIVERSITEIT VAN AMSTERDAM OP GEZAG VAN DE
RECTOR MAGNIFICUS PROF. DR. J.J.M. FRANSE TEN OVERSTAAN VAN
EEN DOOR HET COLLEGE VOOR PROMOTIES INGESTELDE COMMISSIE,
IN HET OPENBAAR TE VERDEDIGEN IN DE AULA DER UNIVERSITEIT
OP MAANDAG 19 JUNI 2000 TE 12.00 UUR

door

Edouard Boudinov

geboren te Astrakhan, Rusland

Promotor: **Prof. Dr. W. Hoogland**
Co-promotor: **Dr. P. M. Kluit**

Faculteit der Natuurwetenschappen, Wiskunde en Informatica.

This work described in this thesis is part of the research program of 'het Nationaal Instituut voor Kernfysica en Hoge-Energie Fysica (NIKHEF)' in Amsterdam, the Netherlands. The Author was £nancially supported by 'de Stichting voor Fundamenteel Onderzoek der Materie (FOM)', which is funded by 'de Nederlandse Organisatie voor Fundamenteel Onderzoek der Materie (NWO)'.

to my parents

Contents

Introduction

It is well known that matter consists of atoms and that the atom comprises a nucleus surrounded by a cloud of electrons. In turn the nucleus is made up from neutrons and protons. These nucleons are themselves complex structures made from quarks—*up* (u) and *down* (d) quarks. Such quarks together with the leptons, of which the electron is the best-known example, appear to be the ultimate constituents of matter and are called *matter* particles. Leptons and quarks are fermions as they have half-integral (1/2) spin and obey Fermi-Dirac statistics. They are also point-like, i.e. there is no experimental evidence for a possible substructure in these particles at distances down to $\approx 10^{-16}$ cm. Each quark has its antiparticle, which has the same quantum numbers and mass as the particle except for the charge which is opposite for particles and antiparticles. The particle and its antiparticle can annihilate when they collide.

There exist other fundamental matter particles; they are charged and uncharged leptons as well as their antiparticles. The charged leptons are called *electron* (e), *muon* (μ) and *tau* (τ), which have all the same charge (-1) and differ only in the masses they have. Each of them has its corresponding uncharged counterpart called *neutrino* (denoted by ν_{e}, ν_μ, ν_τ). They are assumed to be massless as the experiments give only upper limits on their masses. One charged lepton and its uncharged counterpart form one of three fermion generations: (e, ν_{e}), (μ, ν_μ) and (τ, ν_τ).

The quarks (q) are all charged fermions. They can either have charge +2/3, *up* (u), *charm* (c) and *top* (t), or charge -1/3, *down* (d), *strange* (s) and *bottom* (b). The quarks with charge +2/3 are called up-type quarks and the quarks with charge -1/3 down-type quarks. Like the leptons, the quarks are also grouped in pairs to form three quark generations. These pairs consist of an up-type and a down-type quarks: (u, d), (c, s) and (t, b). Thus, the difference in charges between members of a generation is the same for quarks and leptons. From one generation to another the charged leptons and the quarks increase in mass. Our world is mainly build up from the quarks and leptons of the £rst generation $\{(\mathrm{e}, \nu_{\mathrm{e}}), (u, d)\}$. Other matter particles have been discovered in cosmic rays and in accelerator experiments.

The quarks have not been observed as free particles. They appear bounded inside hadrons, of which the proton and neutron are the best-known examples. Therefore, a hadron is not really an elementary particle as it is made up from quarks.

In this thesis we will study a quark from the second generation: the *strange* (s) quark. It forms together with a u or d quark strange hadrons like the charged kaons, $\mathrm{K}^{\pm}$. The DELPHI detector is equipped with Cherenkov detectors that allow us to identify the charged kaons individually.

Other fundamental particles called *£eld* particles are carriers of the forces between matter particles. They are the photon (γ), the gluons (g), the $W^{\pm}$ and Z^0. Of these the best-known example is the photon, the carrier of the electromagnetic force. All the £eld particles are *bosons*, and obey Bose-Einstein statistics. They are considered to be as fundamental as the quarks and leptons. The interactions they represent are the electromagnetic (γ), weak ($W^{\pm}, \mathrm{Z}^0$) and strong (g) interactions. These three interactions[1] differ in strength. The electromagnetic interaction is a long-range force. The strong and weak interactions play an important role on distances of $\leq 10^{-13}$ cm, i.e. at high-energy interactions. The electromagnetic and weak interactions are uni£ed in the so-called electroweak force in the framework of the Electroweak Standard Model. The model predicts that at short-distances (or at high-energies) the two components of this force have comparable strengths.

At the energy scale of LEP (Large Electron and Positron collider) at CERN (Centre Europeén de Recherche Nucleaire—the European centre for particle physics research, Switzerland), we probe the electroweak model by analysing the decay properties of the Z^0 boson. At LEP, beams of electrons and positrons of equal energies collide with a centre-of-mass energy of about 91.2 GeV, the mass of the Z^0. These Z^0 particles are therefore created at rest. The Z^0 decays into a fermion - antifermion (either lepton - antilepton, or quark - antiquark) pair. The sample of events where the Z^0 decays to a pair of strange quarks ($s\bar{s}$) will be the subject of this thesis.

An important aspect of the interactions between elementary particles is the fact that they conserve certain symmetries. Some of these symmetries are *universal*, like the conservation of momentum, energy and angular momentum. Others are not universal as they can be broken in some interactions. Non-universal symmetries are, for instance, the symmetries for space inversion (P), time reversal (T), and charge conjugation (C) (or particle and antiparticle interchange). The P, T, C symmetries are exact symmetries of the strong and electromagnetic interactions. The weak interaction violates each of these symmetries.

Parity (P) violation in the electroweak interaction results in an asymmetric production of s and $\bar{s}$ quarks with respect to the direction of incidence of the initial electrons and positrons. The electroweak Standard Model quantitatively predicts this forward-backward asymmetry. It predicts different values of the asymmetry for down-type and up-type quarks, but the same values for all down-type (or up-type) quarks. The forward-backward asymmetry for $b\bar{b}$ and $c\bar{c}$ pairs has already been measured by experiments at LEP. The measurement of the s quark (a down-type quark) forward-backward asymmetry provides a test of the prediction that the down-type quark asymmetries are equal. The subject of this thesis is the measurement of the s quark forward-backward asymmetry in Z^0 decays:

$$\mathrm{e}^+\mathrm{e}^- \to \mathrm{Z}^0 \to s\bar{s}$$

The thesis is organised as follows. The £rst chapter discusses the theoretical background relevant for the experimental analysis. It presents the predicted cross-section and forward-backward asymmetry of the fermion pair production at the LEP collider. It shows how

[1]In fact there is a fourth force: gravity. But this force is in practice so small that it can be ignored at the distance scale we consider.

the forward-backward asymmetries measured at the Z^0 peak are sensitive through the electroweak corrections to the mass of the top quark and to the mass of the hypothetical Higgs particle (predicted by the electroweak Standard Model). Chapter 2 introduces the DELPHI detector. It contains a short functional description of all its components and their performances. Chapter 3 is devoted to the DELPHI Ring-Imaging Cherenkov detector system (the gaseous and liquid radiator RICHs in the central (barrel) and forward/backward regions) that is designed for charged hadron identi£cation. It gives extensive details on the ring-£nding algorithm, which has been applied for the charged kaon identi£cation in this analysis. Chapter 4 describes the event sample selection and background rejection. It also presents the performance of the high-energy kaon identi£cation in the gaseous radiator of the forward and barrel RICHs. Chapter 5 and 6 present the experimental measurements of the charged kaon and s (strange) quark forward-backward asymmetries, respectively. The measurements are interpreted in terms of the electroweak model parameters in Chapter 6.

Chapter 7 summarises the main results of the thesis and makes some concluding remarks.

Appendix B presents the derivation of an algorithm for unconstrained optimization—the Manevich's conjugate directions method—that was further developed and applied in this thesis.

At the end a summary of the thesis is given.

Chapter 1

Theory

1.1 Standard Model

In its present form, the *Standard Model* describes a world consisting of spin 1/2 *fermions* that interact through the exchange of *bosons* of integer spin. These fermions are either leptons or quarks. The leptons and quarks are considered to be point-like particles. The particles are subject to the following interactions:

Electromagnetic interaction between all charged particles is mediated by the exchange of a massless photon (γ). The gauge theory describing this interaction is Quantum Electro-Dynamics (QED).

Weak interaction between all quarks and leptons is mediated by massive vector bosons. There are two kinds of these bosons: the charged one, $\mathrm{W}^{\pm}$, and the neutral one, Z^0. The W (W^{+}or W^{-}) changes the charge and the type of the fermion. It couples to left-handed particles[1] only. The Z^0 couples to the left- and right-handed particles but with different strengths (couplings). It changes neither the charge, nor the type of the fermion that emits this boson. The gauge theory describing this interaction is the Glashow-Salam-Weinberg (GSW) theory of electroweak interactions [1]. It treats the weak and electromagnetic interactions as different components of a single electroweak force.

Strong interaction between quarks is mediated by the exchange of massless gluons. The gauge theory describing this interaction is Quantum Chromo-Dynamics (QCD).

The Standard Model is characterised by the gauge group $SU(3)_C \times SU(2)_L \times U(1)_Y$. The gauge group $SU(3)_C$ corresponds to the strong interactions. It allows quarks to carry one of three conserved color charges. It has 8 gauge bosons, gluons, that carry color charge

[1]One says that a particle is left-handed (right-handed) or has a helicity $\lambda = -1$ ($\lambda = +1$) if the velocity and spin directions are anti-parallel (parallel). Since the de£nition of the helicity is not Lorentz-invariant, the fermion's "current" is considered to have the two components: right and left. The W couples to the left component of the fermion's current.

as well[2]. $SU(3)$ is a non-Abelian symmetry, so it is not only possible for £eld bosons to couple to fermions but it is also possible for them to couple to one another at three or four boson vertices. The gauge group $SU(2)_L \times U(1)_Y$ corresponds to the GSW theory and is referred to as the Standard Model of electroweak interactions. To agree with the experimental observation that right-handed fermions do not interact with the W £eld, $SU(2)_L$ arranges the left-handed fermions in weak isodoublets and the right-handed fermions in weak isosinglets; right-handed neutrinos should not exist, unless those neutrinos have a non-zero mass. This group is also a non-Abelian group and has three massless bosons, W^+, W^0 and W^-, with a coupling strength g. The third weak-isospin component characterises the weak-charge, to which the bosons couple. Table 1.1 gives the weak isospins of the various fermions. $U(1)_Y$ has one massless boson, B, with a coupling strength g'. This boson interacts with the conserved weak-hypercharge Y of a fermion, which is related to the electric charge and weak isospin of the fermions. Both left- and right-handed particles interact with this £eld. To comply with the experimental fact that the weak force is a short-range force, the bosons of the weak interaction must have a large mass. The weak bosons acquire mass by assuming the compound symmetry $SU(2)_L \times U(1)_Y$ to be spontaneously broken by the Higgs mechanism [2].

Fermions	Generation			Q/e	I_3	
	1	2	3		left-handed	right-handed
Leptons	ν_{e}	ν_μ	ν_τ	0	1/2	—
	e^-	μ^-	τ^-	-1	-1/2	0
Quarks	u	c	t	2/3	1/2	0
	d	s	b	-1/3	-1/2	0

Table 1.1: *The three lepton and quark generations. The values of the electric charge Q and of the component of the weak isospin I_3 are listed for various fermions. The neutrinos are assumed to be massless.*

The effect of the Higgs mechanism is for the primitive £eld bosons to absorb the so-called Goldstone bosons and to mix giving the set of observable £eld bosons:

$$\begin{aligned} &\mathrm{W}^+, \ \mathrm{W}^- \\ \mathrm{Z}^0 &= W^0 \cos\theta_W - B \sin\theta_W \\ A &= W^0 \sin\theta_W + B \cos\theta_W . \end{aligned}$$

Among these, W^+, W^- and Z^0 are now massive but the photon (A) remains massless; θ_W is the electroweak mixing angle. Of course, the coupling strength of the photon, $e = \sqrt{4\pi\alpha}$, is well known and constrains the values of g and θ_W,

[2]Traditionally, these color charges are called *blue*, *red* and *green*. Different quarks are said to have different ¤*avours*. So far, six quark ¤avours have been found.

$$\begin{aligned} e &= g \sin\theta_W \\ \frac{1}{e^2} &= \frac{1}{g^2} + \frac{1}{g'^2} \end{aligned} \quad (1.1)$$

The known electromagnetic charges Q of the fermions give the relation of weak hypercharge (Y) and weak isospin (I_3):

$$Q = I_3 + Y/2$$

Further, there exists a relation between the masses of the W and Z^0:

$$m_Z = m_{\mathrm{W}}/\cos\theta_W \quad \text{or} \quad \sin^2\theta_W = 1 - \frac{m_W^2}{m_Z^2} \quad (1.2)$$

The massive W^+ and W^- continue to couple only to the left-handed particles, but the Z^0 now couples to the left- and right handed fermions with the corresponding couplings :

$$\begin{aligned} c_L^f &= I_3^f - Q_f \sin^2\theta_W \\ c_R^f &= -Q_f \sin^2\theta_W \end{aligned}$$

The simplest form for the Goldstone £eld is a $Y = 1$ weak-isospin doublet (weak isodoublet) of scalar £elds:

$$\phi = \begin{pmatrix} \phi^+ \\ \phi^0 \end{pmatrix}$$

Taking into account their antiparticles there are four scalar £elds—ϕ^+, ϕ^0, ϕ^- and $\tilde{\phi}^0$. The bosons, W^-, W^+ and Z^0, acquire mass by absorbing three Goldstone bosons. The one neutral scalar £eld that is left is the so-called Higgs £eld. The corresponding Higgs particle has a large mass. Its mass is not predicted by the theory; it must be determined by experiment. The averaged m_W value measured at CDF, UA2, D0, and at LEP 2 is 80.394 ± 0.042 GeV/c^2 [3]. The m_Z value measured at LEP 1 (ALEPH, DELPHI, L3 and OPAL) is 91.187 ± 0.002 GeV/c^2 [3]. From LEP and other electroweak data one can conclude that the Higgs mass (if this particle exists) should be larger than $\sim$ 95 GeV/c^2 and smaller than 215 GeV/c^2 at the 95% con£dence level (CL) [3].

The tree level diagrams of the electroweak couplings to fermions and the coupling constants are summarised hereafter :

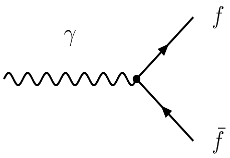

$= ieQ_f\gamma_\mu$

f is any quark or lepton and $e = \sqrt{4\pi\alpha}$

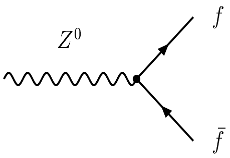

$$= \frac{ie\gamma_\mu(v_f - a_f\gamma_5)}{2\sin\theta_W\cos\theta_W}$$

f is any quark or lepton

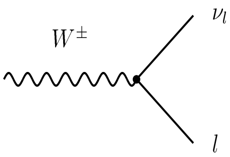

$$= \frac{ie\gamma_\mu(1-\gamma_5)}{2\sqrt{2}\sin\theta_W}$$

for the $\mathrm{W}^-(\mathrm{W}^+)$ vertex l is any charged lepton (antilepton) and ν_l the corresponding anti-neutrino (neutrino).

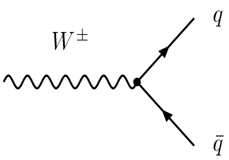

$$= \frac{ie\gamma_\mu(1-\gamma_5)}{2\sqrt{2}\sin\theta_W}\cdot V_{ij}$$

i and j correspond to quarks having different ¤avours, one quark must be an up-type quark, the other one a down-type quark, e.g., if this is a W^+ vertex then $i = u, c$ or t and $j = d, s$ or b; V is the Cabibbo-Kobayashi-Maskawa matrix.

The $\gamma_\mu(\mu = 0,1,2,3)$ and γ_5 are the Dirac gamma matrices. We use the vector and axial-vector coupling constants, which are related to the coupling constants of left- and right-handed currents through the relations:

$$v_f = c_L^f + c_R^f, \quad a_f = c_L^f - c_R^f,$$

so that we have:

$$\begin{aligned} v_f &= I_3^f - 2Q_f\sin^2\theta_W \\ a_f &= I_3^f \end{aligned} \tag{1.3}$$

where Q_f is the electric charge of a given fermion species and I_3^f is the third isospin component for the left-handed fermion, as listed in Table 1.1. Table 1.2 shows the vector and axial-vector coupling of various fermions.

At low energies the electroweak amplitude involving charged W-boson exchange reduces to the Fermi point-interaction amplitude [4], so there exists a connection between g and G_F[3]:

[3]From the muon (μ) lifetime measurement the Fermi constant was very precisely determined to be $G_F = 1.16639(1)\times10^{-5}$ GeV^{-2}

Fermions	a_f	v_f
ν_e, ν_μ, ν_τ	$\frac{1}{2}$	$\frac{1}{2}$
e, μ, τ	-$\frac{1}{2}$	-$\frac{1}{2} + 2\sin^2\theta_W$
u, c, t	$\frac{1}{2}$	$\frac{1}{2} - \frac{4}{3}\sin^2\theta_W$
d, s, b	-$\frac{1}{2}$	-$\frac{1}{2} + \frac{2}{3}\sin^2\theta_W$

Table 1.2: *Vector and axial-vector couplings of the fermions to the* Z^0.

$$\begin{aligned} G_F = G_\mu &= \frac{g^2}{4\sqrt{2}m_W^2} \cdot \frac{1}{1-\Delta r} = \frac{\pi\alpha}{\sqrt{2}} \frac{1}{\sin^2\theta_W m_W^2} \cdot \frac{1}{1-\Delta r} \\ &= \frac{\pi\alpha}{\sqrt{2}} \frac{1}{\sin^2\theta_W \cos^2\theta_W m_Z^2} \cdot \frac{1}{1-\Delta r} \end{aligned} \tag{1.4}$$

Δr includes higher order corrections to the decay amplitude of muon[4], it is a function of both the top quark mass and the Higgs mass.

The analysis presented in this thesis concerns the strange (s) quark production from e^+e^- annihilation, hence the case of interest are $f \equiv$ e and $f \equiv s$. We also will consider other quark £nal states.

1.2 Cross sections around the Z^0 peak

The process of e^+e^- annihilation with production of a quark and anti-quark pair, $e^+e^- \rightarrow q\bar{q}$, is described (in the lowest order, so-called Born approximation) by the two Feynman diagrams shown in Figure 1.1. The £rst diagram represents the annihilation through a virtual photon, which is dominating at centre-of-mass energies below the Z^0 mass. The second one represents the annihilation through the production of a real Z^0 particle. The lifetime of the Z^0 is extremely short, and it immediately decays into a fermion and anti-fermion pair. If s is the centre-of-mass energy squared, $\mu_q = m_q^2/s$, then the differential cross-section for this process can be written as follows [5]:

$$\begin{aligned} \frac{d\sigma}{d\Omega}(s) = \frac{\alpha^2}{4s} N_C^q \sqrt{1-4\mu_q} \quad \cdot \quad & [G_1(s) \cdot (1+\cos^2\theta) + G_3(s) \cdot 2\cos\theta \cdot \sqrt{1-4\mu_q} \\ & + G_2(s) \cdot \sin^2\theta \cdot 4\mu_q] \end{aligned} \tag{1.5}$$

where $N_C^q = 3$ is the QCD colour factor for quarks, $d\Omega = d\phi d\cos\theta$ with ϕ the azimuthal

[4]The higher order corrections must be calculated for each observable individually. For example, the higher order corrections to the forward-backward asymmetry are discussed in section 1.4

Figure 1.1: *Feynman diagrams for the process* $e^+e^- \rightarrow Z/\gamma \rightarrow f\bar{f}$ *in the lowest order.*

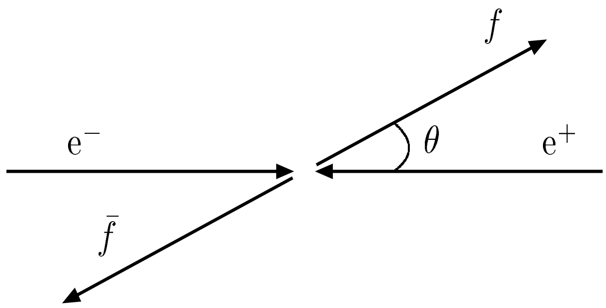

Figure 1.2: *De£nition of the polar angle* θ *between the incoming* e^- *and the outgoing* f*.*

angle and θ the polar angle that is the scattering angle in the centre-of-mass system, as de£ned in Figure 1.2, and

$$\begin{aligned} G_1(s) &= Q_e^2 Q_q^2 + F^2 \cdot 2Q_e Q_q v_e v_q \mathrm{Re}\chi_0(s) \\ &\quad + F^4 \cdot (v_e^2 + a_e^2)(v_q^2 + a_q^2 - 4\mu_q a_q^2)|\chi_0(s)|^2 \\ G_2(s) &= Q_e^2 Q_q^2 + F^2 \cdot 2Q_e Q_q v_e v_q \mathrm{Re}\chi_0(s) \\ &\quad + F^4 \cdot (v_e^2 + a_e^2) v_q^2 |\chi_0(s)|^2 \\ G_3(s) &= F^2 \cdot 2Q_e Q_q a_e a_q \mathrm{Re}\chi_0(s) + F^4 \cdot 4 v_e a_e v_q a_q |\chi_0(s)|^2 \end{aligned} \tag{1.6}$$

Equations (1.3) de£ne the vector and axial-vector couplings, $F = (2\sin\theta_W \cos\theta_W)^{-1}$ is the overall factor for these couplings; $\chi_0(s)$ is the Z^0 propagator that is normalised to the photon propagator :

$$\chi_0(s) = \frac{s}{s - m_Z^2 + i m_Z \Gamma_Z^0} \tag{1.7}$$

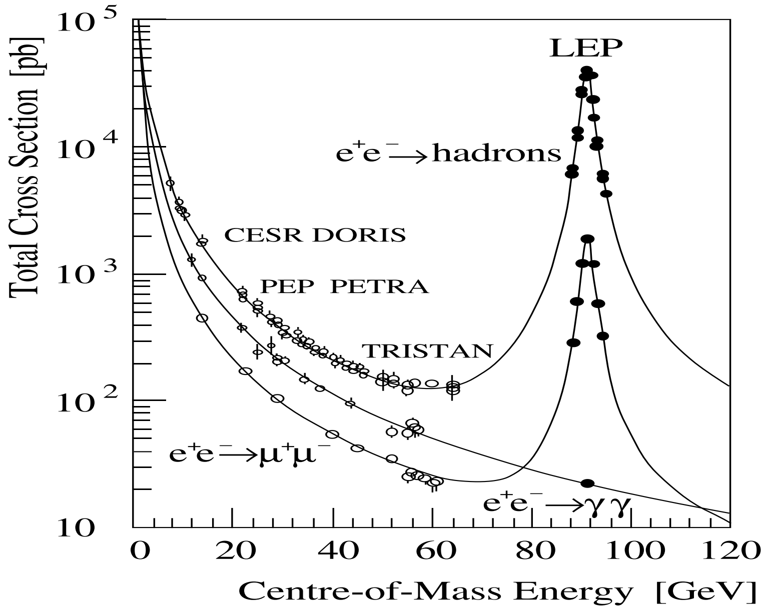

Figure 1.3: $\mathrm{e^+e^-}$ *cross-section vs. centre-of-mass energy. The two s-channel processes are shown:* $\mathrm{e^+e^-} \to Z/\gamma \to \mu^+\mu^-$ *and* $\mathrm{e^+e^-} \to Z/\gamma \to q\bar{q} \to \mathrm{hadrons}$. $\mathrm{e^+e^-} \to \gamma\gamma$ *is the t-channel annihilation process. The lines indicate the prediction of the Standard Model [6].*

Γ_Z^0 is the total width of the Z^0 ($= \tau_Z^{-1}$), which is a sum of the partial widths Γ_f of $\mathrm{Z}^0 \to f\bar{f}$, with the QCD color factor $N_C^f = 1$ for leptons and $N_C^f = 3$ for quarks :

$$
\begin{aligned}
\Gamma_Z^0 &= \sum_f \Gamma_f \; ; \qquad f = \mathrm{e}, \mu, \tau, \nu_\mathrm{e}, \nu_\mu, \nu_\tau, u, c, d, s, b \\
\Gamma_f &= N_C^f \frac{\alpha}{3} m_Z \sqrt{1-4\mu_f} \left(v_f^2(1+2\mu_f) + a_f^2(1-4\mu_f) \right) F^2 \\
&\approx N_C^f \frac{\alpha}{3} m_Z \, (v_f^2 + a_f^2) F^2
\end{aligned}
\tag{1.8}
$$

Integrating the expression for the differential cross-section (1.5) over the full solid angle (the term containing the function G_3 vanishes as it is asymmetric in the polar angle) gives the total cross-section:

$$
\begin{aligned}
\sigma(s) &= \frac{s}{(s-m_Z^2)^2 + m_Z^2(\Gamma_Z^0)^2} \left\{ \frac{12\pi\Gamma_\mathrm{e}\Gamma_q}{m_Z^2} + \frac{(s-m_Z^2)I}{s} \cdot \sqrt{1-4\mu_q}(1+2\mu_q) \right\} \\
&\quad + \frac{4\pi\alpha^2}{3s} \cdot N_C^q Q_q^2 \cdot \sqrt{1-4\mu_q}
\end{aligned}
\tag{1.9}
$$

The last term in Equation (1.9) represents the annihilation through the photon (σ_γ), the £rst term is the resonance production of the Z^0 (σ_Z), and the second term is the $\gamma - \mathrm{Z}^0$ interference term ($\sigma_{\gamma-Z}$), with

$$I = \frac{8}{3}\pi\alpha^2 v_q a_q Q_q N_C^q$$

The total cross-section as a function of the centre-of-mass energy is shown in Figure 1.3.

In the LEP running period from 1989 until 1995 (the so-called LEP 1 period) the centre-of-mass energy of the colliding particles was around 91.2 GeV, which is almost the mass of the Z^0.[5] At the Z^0 mass for a £nal state consisting of a $s\bar{s}$ pair, we have

$$\begin{aligned}
\sigma_Z(\sqrt{s} = m_Z) &= \frac{12\pi Br_{\mathrm{e}} Br_s}{m_Z^2} \approx 90 \cdot 10^{-34}\mathrm{cm}^2 = 9\ \mathrm{nbarn} \\
\sigma_{\gamma-Z}(\sqrt{s} = m_Z) &= 0 \\
\sigma_\gamma(\sqrt{s} = m_Z) &= \frac{4\pi\alpha^2}{3s} \cdot 3(\frac{1}{3})^2 \approx 4 \cdot 10^{-36}\mathrm{cm}^2 = 4\ \mathrm{pbarn} \\
\frac{\sigma_Z}{\sigma_\gamma}(\sqrt{s} = m_z) &= \frac{9Br_{\mathrm{e}}Br_s}{\alpha^2} \cdot 3 \approx 2250
\end{aligned} \tag{1.10}$$

where the branching ratios $Br_{\mathrm{e}} \equiv \Gamma_{\mathrm{e}}/\Gamma_Z^0$ and $Br_s \equiv \Gamma_s/\Gamma_Z^0$ have values of 0.034 and 0.15, respectively. The inverse electromagnetic coupling at the m_Z has a value $\alpha^{-1} = \alpha^{-1}(m_Z^2) = 128.9$ compared to $\alpha^{-1}(0) = 137$ (see section 1.4).
Equations (1.10) show that at the Z^0-pole the interference term disappears and $\sigma_Z \gg \sigma_\gamma$.
Even for the heaviest fermion b, the terms containing μ_f in (1.5)-(1.6) and (1.8)-(1.9) give contributions of order $\leq$0.8% and can be neglected in the framework of our measurement of $s\bar{s}$ asymmetry (see section 1.3)
One can also see that for all down-type quarks the corresponding partial widths are the same (without accounting for μ_q-terms) as they have the same couplings to the Z^0.

1.3 Forward-backward asymmetries around the Z^0 peak

Due to the asymmetric term G_3 in equation (1.5) the production cross-section for the forward (polar angle $\theta < 90°$) and backward (polar angle $\theta > 90°$) hemispheres are different. We de£ne the forward-backward asymmetry for the process $\mathrm{e}^+\mathrm{e}^- \rightarrow q\bar{q}$ as

$$A_{FB}^q(s) = \frac{\sigma_F^q(s) - \sigma_B^q(s)}{\sigma_F^q(s) + \sigma_B^q(s)} \tag{1.11}$$

[5] Since 1996, LEP is running at centre-of-mass energies of 160-208 GeV.

with

$$\begin{aligned} \sigma_F^q(s) &= \int_{c_0}^{c} \frac{d\sigma}{d\cos\theta}(s)\, d\cos\theta \qquad \sigma_B^q(s) = \int_{-c}^{-c_0} \frac{d\sigma}{d\cos\theta}(s)\, d\cos\theta\,; \\ \frac{d\sigma}{d\cos\theta}(s) &= \int_0^{2\pi} \frac{d\sigma}{d\Omega}(s)\, d\phi = 2\pi \cdot \frac{d\sigma}{d\Omega}(s) \end{aligned} \tag{1.12}$$

where the c_0 and c ($1 \geq c > c_0 \geq 0$) are the integration limits in the cosine of the polar angle. For this study the asymmetry is determined for the $s\bar{s}$ £nal state. Upon integration of equation (1.5) we obtain

$$\begin{aligned} A_{FB}^q(s) &= \frac{3(c^2 - c_0^2) \cdot G_3(s)}{3(c - c_0)[G_1(s) + 4\mu_q G_2(s)] + (c^3 - c_0^3)[G_1(s) - 4\mu_q G_2(s)]} \\ &\quad \times \sqrt{1 - 4\mu_q} \end{aligned} \tag{1.13}$$

The μ_q-terms give an extremely small correction to the asymmetry because $m_q/m_Z \ll 1$. For a b quark there is a 0.5% contribution, which is far below the experimental accuracy. Neglecting these terms, Equation (1.13) simpli£es to

$$A_{FB}^q(s) = \frac{3(c + c_0)}{(3 + c^2 + cc_0 + c_0^2)} \cdot \frac{G_3(s)}{G_1(s)} \tag{1.14}$$

This analysis deals with the data collected in the period from 1992 till 1995. The largest fraction of the data is collected at the Z^0 peak at the centre-of-mass energy of about 91.2 GeV. These data will be used to determine the s quark *pole* asymmetry. In 1993 and 1995 also some statistics has been collected at energies of 89.5 and 93.0 GeV. These data will be used to investigate the energy dependence of the asymmetry near the Z^0 peak.

The *pole* asymmetry is de£ned as the asymmetry at centre-of-mass equal to the mass of the Z^0, $s = m_Z^2$ in the absence of the γ exchange diagram. Consider Formula (1.14) with $s = m_Z^2$, $c_0 = 0$, $c = 1$:

$$A_{FB}^q(m_Z^2) = \frac{3}{4} \cdot \frac{2v_e a_e \cdot 2v_q a_q \cdot F^4}{(v_e^2 + a_e^2)(v_q^2 + a_q^2) \cdot F^4 + \left(\frac{\Gamma_Z^0}{m_Z}\right)^2 Q_q^2} \tag{1.15}$$

The $\left(\frac{\Gamma_Z^0}{m_Z}\right)^2$-term is due to the γ exchange diagram. As we want to analyse the asymmetry for the Z^0 vertex only, we omit this term. (In this analysis we will correct the quark asymmetry for this γ exchange diagram in order to obtain the pole asymmetry.) Then Equation (1.15) simpli£es to

$$A^q_{FB}(m_Z^2) = \frac{3}{4} \cdot A_{\mathrm{e}}\, A_q \tag{1.16}$$

with

$$A_f = \frac{2v_f a_f}{v_f^2 + a_f^2} \overset{(1.3)}{=} \frac{2(1 - 4|Q_f|\sin^2\theta_W)}{1 + (1 - 4|Q_f|\sin^2\theta_W)^2} \tag{1.17}$$

This shows that in lowest order the on-peak asymmetry is determined exclusively by the value of $\sin^2\theta_W$. The pole asymmetry will be used to determine the electroweak mixing angle.

To show how the asymmetry changes near the peak, we neglect the $\left(\frac{\Gamma_Z^0}{m_Z}\right)^2$-terms in (1.14) and use the fact that $v_{\mathrm{e}}^2 \ll a_{\mathrm{e}}^2$. For $c_0 = 0$ and $c = 1$, Formula (1.14) reduces to

$$\begin{aligned} A^q_{FB}(s) \quad &\approx \quad A^q_{FB}(m_Z^2) - \frac{2Q_q a_{\mathrm{e}} a_q}{a_{\mathrm{e}}^2(v_q^2 + a_q^2)} \cdot \left(1 - \frac{m_Z^2}{s}\right) \\ &\overset{(q=s)}{\approx} \quad 0.15 + 1.8 \cdot \left(1 - \frac{m_Z^2}{s}\right) \end{aligned} \tag{1.18}$$

This approximate formula predicts that the strange quark asymmetry increases almost linearly as a function of centre-of-mass energy squared near the Z^0 peak. The actual change in the asymmetry for different quarks around the Z^0 peak will be calculated by ZFITTER [7], which takes into account all kinds of contributions to the asymmetry (see section 1.4).

In Chapter 4 we will show that the DELPHI detector has two polar angle regions where the s-asymmetry analysis can be performed: $0.04 < |\cos\theta| < 0.68$—the barrel region and $0.82 < |\cos\theta| < 0.94$—the forward region. Although, we have less statistics in the forward region than in the barrel region, the forward region is relevant for the s-asymmetry measurement because the asymmetry is maximal in this region. This can be seen by rewriting equation (1.14) as follows

$$\begin{aligned} A^q_{FB}(s, c, c_0) \quad &= \quad \frac{3(c + c_0)}{3 + c^2 + cc_0 + c_0^2} \cdot \frac{G_3(s)}{G_1(s)} \\ &= \quad K_{cc_0} \cdot A^q_{FB}(s, c = 1, c_0 = 0) \\ \text{with} \quad K_{cc_0} &= \frac{4(c + c_0)}{3 + c^2 + cc_0 + c_0^2} \end{aligned} \tag{1.19}$$

where $A^q_{FB}(s, c = 1, c_0 = 0)$ is the quark asymmetry without cuts on the detector acceptance.

The values of c_0 and c are respectively equal to 0.04 and 0.68 in the barrel region and equal to 0.82 and 0.94 in the forward region. With these values the coef£cient K_{cc_0} is 0.82 for the barrel analysis and 1.32 for the forward analysis. The sensitivity to the forward-backward asymmetry in the forward region is accordingly $1.32/0.82$-times larger than that in the barrel region.

1.4 Radiative corrections

As mentioned before, the forward-backward asymmetry in the £rst (lowest) order (or Born approximation) depends on a single parameter—the electroweak mixing angle $\sin\theta_W$. This is not true anymore after including higher order contributions:

$$A_{FB}^{f} \quad = \quad A_{FB}^{f} + \Delta A_{FB}^{RC} \tag{1.20}$$

The radiative correction term ΔA_{FB}^{RC} depends on all parameters of the Standard Model, i.e. those of the Electroweak Standard Model (GSW) $(\alpha, m_Z, m_W, m_H, m_f)$ and of QCD (α_s).

The mixing angle is de£ned as

$$\sin^2\theta_W = 1 - \frac{m_W^2}{m_Z^2}$$

For the process $\mathrm{e}^+\mathrm{e}^- \to f\bar{f}$ the radiative corrections can be divided into the following subclasses:

1. The $O(\alpha)$ (photon bremsstrahlung) QED corrections.

2. The $O(\alpha^2)$ and higher order QED corrections.

3. 'Weak corrections', which collect the electroweak diagrams not included in the QED corrections—propagator corrections, vertex corrections and box diagram contributions.

4. The $O(\alpha_s)$ (gluon bremsstrahlung) QCD corrections.

In the following we discuss the general philosophy of the corrections and give the definitions of the parameters that are important for the asymmetry measurement. All radiative corrections are calculated by ZFITTER. A discussion of the most important ingredients of the radiative corrections included in ZFITTER is given in reference [8]. First we will discuss the weak corrections and then the QED and QCD corrections.

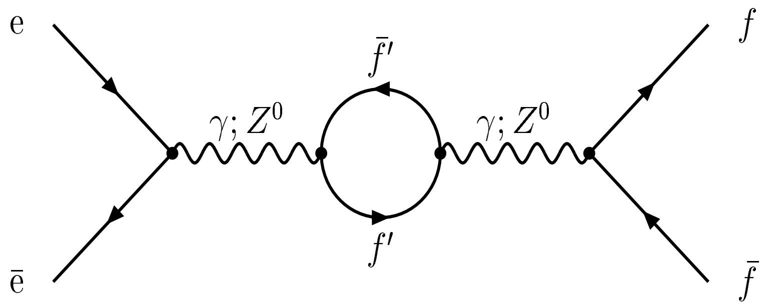

Figure 1.4: *Propagator corrections to* $e^+e^- \to f\bar{f}$

1.4.1 Weak corrections to A_{FB}

Propagator corrections

For the processes with light external fermions ($f \neq t$) corrections like those shown in Figure 1.4 have to be included for the γ and Z^0 propagators.

- In the photon exchange amplitude the corrections are absorbed by a rede£nition of the electromagnetic coupling constant:

$$\frac{\alpha}{s} \quad \to \quad \frac{\alpha(s = m_Z^2)}{s} = \frac{\alpha}{s} \cdot \frac{1}{1 - \Delta\alpha} = \frac{1.064 \cdot \alpha}{s}$$

- In the Z^0 boson exchange amplitude the corrections are absorbed by a rede£nition of the neutral current coupling constant (αF^2) and by the use of the physical Z^0 width $\Gamma_Z = \Gamma_Z^0 + \Delta\Gamma$:

$$\alpha F^2 = \frac{\alpha}{4\sin^2\theta_W \cos^2\theta_W} \quad \to \quad \frac{\alpha(s = m_Z^2)}{4\sin^2\theta_W \cos^2\theta_W} \cdot \frac{1}{(1 + \frac{\cos^2\theta_W}{\sin^2\theta_W}\Delta\rho)(1 - \Delta\rho)}$$

$$m_Z\Gamma_Z^0 \quad \to \quad \frac{s}{m_Z^2} m_Z \Gamma_Z;$$

with

$$\Delta\rho \simeq \frac{\alpha}{4\pi} \frac{3}{4\sin^2\theta_W \cos^2\theta_W} \left(\frac{m_t}{m_Z}\right)^2 \tag{1.21}$$

where m_t is the mass of the top quark. The term $\Delta\Gamma$ summarises all contributions to the width due to QED and QCD corrections up to $O(\alpha^2)$ and $O(\alpha_s)$, respectively. The QCD correction only contributes to the hadronic width and takes the simple form :

$$\Gamma_h \equiv \Gamma(Z^0 \to q\bar{q}) = \Gamma_h^0 \cdot (1 + \frac{\alpha_s(s = m_Z^2)}{\pi}); \qquad \alpha_s(s = m_Z^2) = 0.119 \pm 0.003$$

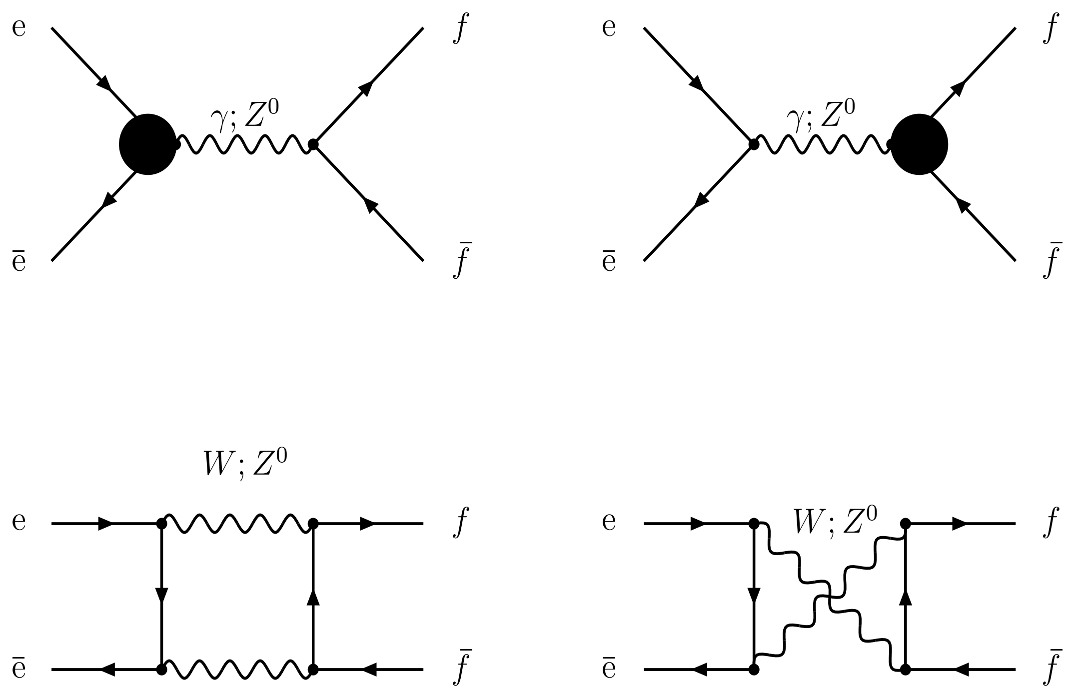

Figure 1.5: *Vertex corrections and box contributions to* $e^+e^- \to f\bar{f}$

- In the γZ^0 interference amplitude corrections can be absorbed by a rede£nition of the mixing angle. For this, we introduce the effective mixing angle $\bar{\theta}$:

$$\sin^2\theta_W \quad\to\quad \sin^2\bar{\theta}_W \simeq \sin^2\theta_W + \cos^2\theta_W \Delta\rho$$

This modi£es the vector and axial-vector couplings:

$$\begin{aligned} v_f &\to \bar{v}_f = I_3^f - 2Q_f \sin^2\bar{\theta}_W \\ a_f &\to \bar{a}_f = I_3^f \end{aligned}$$

All these corrections are universal—they are independent of the quantum numbers of the external fermions $f\bar{f}$.

Weak vertex corrections and box diagrams

Figure 1.5 illustrates the vertex corrections to the electromagnetic and weak neutral current vertex (excluding virtual photons) as well as the box diagrams with two Z^0 and W bosons. For known fermions the vertex corrections can be represented in terms of s-dependent vector and axial-vector form factors. The corrections to the box diagrams allow a similar decomposition but with form factors depending on both s and t. In contrast to the propagator corrections these form factors are not universal but depend explicitly on the quantum numbers of the external fermions.

The on-peak asymmetry, which in lowest order is given by (1.16), becomes including the weak corrections :

$$A^f_{FB}(m_Z^2) = \frac{3}{4} \cdot \bar{A}_{\mathrm{e}}\,\bar{A}_f + \Delta A^f_{FB}(\mathrm{vertex,box}) \tag{1.22}$$

with

$$\bar{A}_f = \frac{2(1-4|Q_f|\sin^2\bar{\theta}_W)}{1+(1-4|Q_f|\sin^2\bar{\theta}_W)^2} \tag{1.23}$$

$\bar{A}_f$ is called the parity violating coupling of the fermion f to the Z^0 boson. We de£ne the *pole* asymmetry as

$$A^0_{f\bar{f}} = \frac{3}{4} \cdot \bar{A}_{\mathrm{e}}\,\bar{A}_f\ , \tag{1.24}$$

which is determined exclusively by the value of $\sin^2\bar{\theta}_W \equiv \sin^2\theta^{lept}_{eff}$.

1.4.2 $O(\alpha)$ QED and $O(\alpha_s)$ QCD corrections to A_{FB}

The $O(\alpha)$ QED and $O(\alpha_s)$ QCD corrections are the result of an incoherent superposition of 2-particle and (inclusive) 3-particle £nal states, where the third particle is an isolated photon or gluon. They depend, in contrast to the weak corrections discussed before, on the experimental set up.

Final state corrections

The QCD corrections contribute only to the £nal state corrections as quarks can only be present in the £nal state, see Figure 1.6. The QED corrections contain contributions from both initial and £nal states as both the electron-positron pair in the initial state and the charged fermion pair in the £nal state can radiate a photon, see Figures 1.7 and 1.8.
First, we consider the QED £nal state corrections. According to (1.11) A^f_{FB} is the ratio of the anti-symmetric to the symmetric part of the cross-section. The effect of the QED corrections can be summarised as follows:

If no cut is applied to the energy of the emitted photon (which is our case), then the symmetric part gets a correction:

$$(\sigma^f_F(s) + \sigma^f_B(s)) \quad\rightarrow\quad (\sigma^f_F(s) + \sigma^f_B(s)) \cdot (1 + \frac{3\alpha}{4\pi}Q_f^2)$$

whereas

$$\delta(\sigma^f_F(s) - \sigma^f_B(s)) = 0.$$

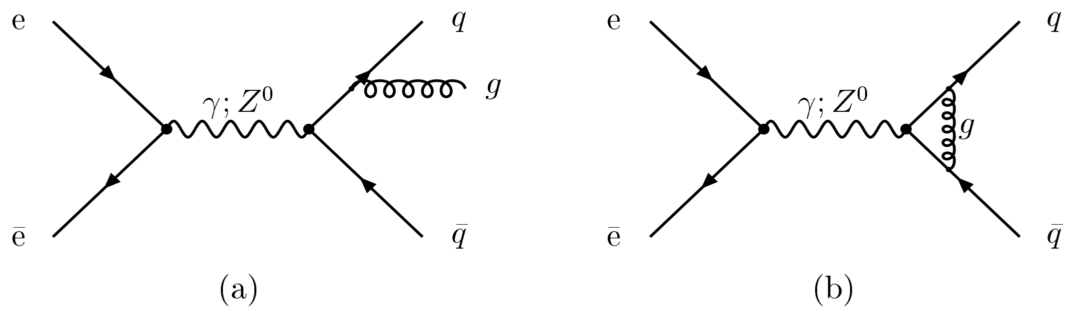

Figure 1.6: *QCD £nal state corrections to* $e^+e^- \rightarrow q\bar{q}$*: a) real gluon £nal state bremsstrahlung; b) virtual one gluon vertex correction.*

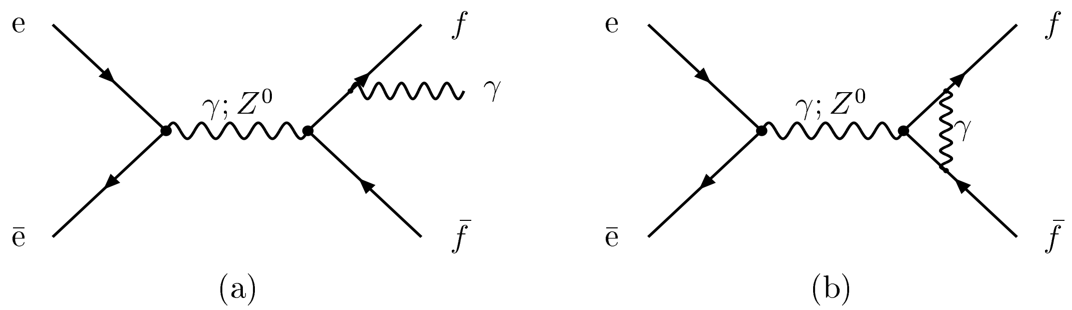

Figure 1.7: *QED £nal state corrections to* $e^+e^- \rightarrow f\bar{f}$, $f \neq \nu$*: a) real photon £nal state bremsstrahlung; b) virtual one photon vertex correction.*

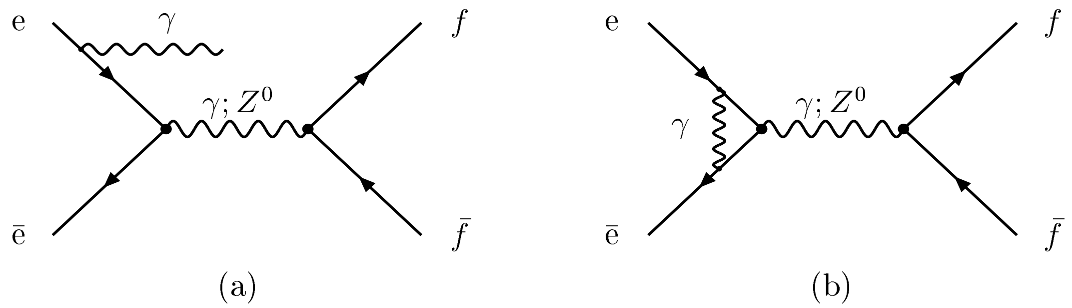

Figure 1.8: *QED initial state corrections to* $e^+e^- \rightarrow f\bar{f}$*: a) real photon initial state bremsstrahlung; b) virtual one photon vertex correction.*

This results in a very small negative contribution ($< 0.17\%$ relative to A^f_{FB}) to the asymmetry

$$A^f_{FB} \quad \rightarrow \quad A^f_{FB} \cdot (1 - \frac{3\alpha}{4\pi} Q^2_f). \tag{1.25}$$

The QCD £nal state corrections to the asymmetry can similarly, for massive quarks, be represented by a multiplying factor to the asymmetry:

$$A^f_{FB} \quad \rightarrow \quad A^f_{FB} \cdot (1 - \frac{\alpha_s}{\pi} \cdot \Delta_q); \qquad \Delta_q = 1 - \frac{4}{3}\pi \frac{m_q}{m_Z}. \tag{1.26}$$

Initial state corrections

The $O(\alpha)$ QED initial state corrections are responsible for some 40% reduction of the Z^0 resonance peak height with respect to that when no initial state radiation is taken into account (1.9). This is due to the rapid variation of $\sigma^f(s)$ with energy, see formula (1.9). Since the asymmetry $A^f_{FB}(s)$ is a steeply increasing function around the Z^0 pole (for example, see formula (1.18)), the energy loss from initial state radiation leads to a reduction in the effective centre-of-mass energy, which reduces the asymmetry.

These corrections are incorporated by convoluting the cross-section σ^f_{imp} with the initial state radiation function $H_{\mathrm{e}}(z)$:

$$\sigma^f(s) = \int_{z_0}^{1} \sigma^f_{imp}(zs) H_{\mathrm{e}}(z)\, dz, \qquad z_0 \geq \frac{4m_f^2}{s}$$

where σ^f_{imp} is the improved Born cross-section, which incorporates the radiative corrections not connected with initial state radiation as described in section 1.4.1.

Initial - £nal state interference

If no cut is applied on the energy of the emitted photon, then the total contribution to the asymmetry is negligibly small.

1.4.3 Higher order QED corrections to A_{FB}

A realistic treatment of A^f_{FB} requires the inclusion of QED corrections in higher than $O(\alpha)$ order. Here, the most important case is the initial state radiation of two photons—$O(\alpha^2)$.

		$\sqrt{s}$ (GeV)		
		89.5	91.2	93.0
A^s_{FB} (Born)	$\sin^2\theta_W = 0.2230$	0.1160	0.1509	0.1852
A^s_{FB} (Born)	$\sin^2\theta_W = 0.2313$	0.0681	0.1046	0.1408
A^s_{FB} (Exact)	$\sin^2\theta^{lept}_{eff} = 0.2313$	0.0623	0.0995	0.1248
A^c_{FB} (Born)	$\sin^2\theta_W = 0.2230$	0.0219	0.1119	0.2001
A^c_{FB} (Born)	$\sin^2\theta_W = 0.2313$	-0.0192	0.0751	0.1681
A^c_{FB} (Exact)	$\sin^2\theta^{lept}_{eff} = 0.2313$	-0.0313	0.0642	0.1297

Table 1.3: *The forward-backward asymmetry of quarks around the* Z^0 *peak for the Born approximation (1.14) with* $\sin^2\theta_W = 0.223$ *and with the value* $\sin^2\theta^{lept}_{eff} = 0.2313$*, and for the ZFITTER prediction that includes the radiative corrections described in this section. The asymmetries shown are for the* s *quark (down-type quark) and for the* c *quark (up-type quark).*

1.4.4 Discussion

This thesis deals with the strange quark forward-backward asymmetry at the Z^0 peak. The measured asymmetry at $\sqrt{s} = 91.2$ GeV is used to extract the s quark pole asymmetry. According to (1.24) this measurement will contribute to the measurement of the effective electroweak mixing angle $\sin^2\theta^{lept}_{eff}$. With this and with the measured values of m_W and m_Z from LEP/CDF/D0 one can determine the $\Delta\rho$ parameter (see Eq. (1.21)). $\Delta\rho$ is sensitive to the mass of the top quark and in combination with other electroweak measurements sets a constraint on the Higgs mass m_H.

From the pole asymmetry measurement one can also extract the parity violating coupling of the s-quark to the Z^0 boson, $\bar{A}_s$, de£ned in (1.24) and compare it with that for the b-quark. The Standard Model predicts the two couplings to be the same.

We will also measure the s quark forward-backward asymmetry (1.11) at centre-of-mass energies of 89.5 and 93.0 GeV, hoping that the statistical precision will be enough to get the sign of the axial-vector coupling a_s and compare it with the prediction (1.18). Table 1.3 shows the asymmetries at these energies from the Born approximation (1.14) and those from the exact calculation by ZFITTER with $m_Z = 91.1866$ GeV/c^2, $m_t = 173$ GeV/c^2, $m_H = 115$ GeV/c^2, $\alpha_s = 0.122$ as input parameters. This shows the importance of including radiative corrections.

1.5 Fragmentation and hadronisation of quarks

As we are interested in the s quark asymmetry measurement, we consider only quark pair ($q\bar{q}$-pair) production in the £nal state. Our goal is to determine how the quark pair is oriented in space and for this we have to distinguish the quark from the antiquark. Quarks do not appear to an observer as free particles; they are bounded inside hadrons and these hadrons are observable. According to QCD, quarks can radiate high-energy gluons. This is called

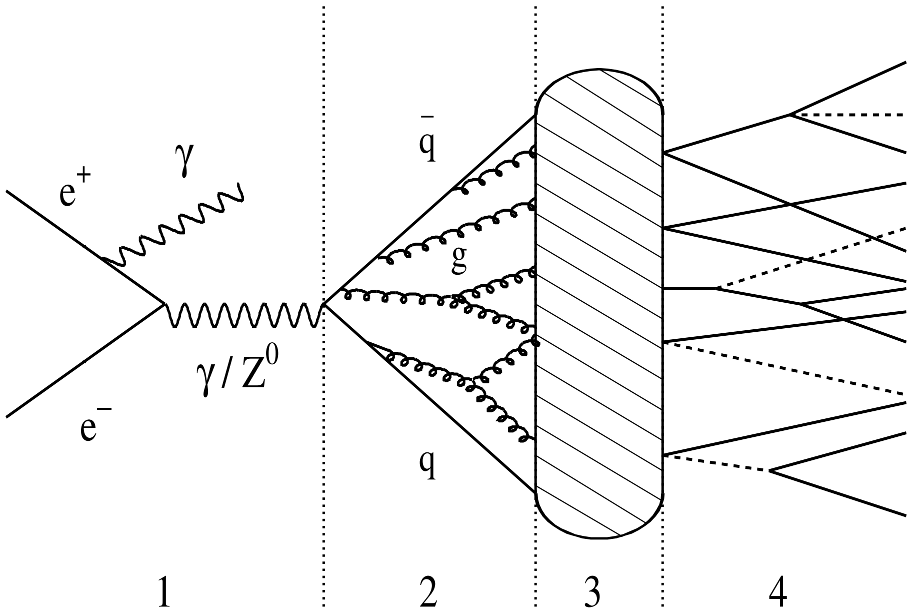

Figure 1.9: *Schematic illustration of the four phases distinguished in the text for the process* $\mathrm{e^+e^-} \rightarrow q\bar{q} \rightarrow \mathrm{hadrons}$.

the *perturbative* QCD phase, which can be simulated by Monte Carlo programs that include the perturbative QCD calculations. Here, all the quarks and gluons produced in this stage are called partons. These partons form hadrons. The process of hadron production belongs to the *non-perturbative* QCD phase (also called the *hadronisation* phase) which cannot be calculated exactly in QCD. Hence, it must be described by phenomenological models. These models can be coded into Monte Carlo programs. Finally, the hadrons freely decay into stable particles—hadrons, leptons and photons. These particles can be detected using particle detectors. This leads to the schematic description of hadronic event production shown in Figure 1.9. Four regions can be distinguished :

- **Region 1:** The $\mathrm{e^+e^-}$ annihilation process into $\mathrm{Z^0}$ or γ with their decay into the $q\bar{q}$-pair. This has been discussed in detail in sections 1.2, 1.3 and 1.4. Various Monte Carlo programs have been written to describe this stage, see for example [9].

- **Region 2:** The $q\bar{q}$-pair radiates hard gluons, the gluons in turn can split into quark-antiquark or gluon-gluon pairs. Perturbative QCD is used here to describe the process. One can calculate the matrix elements for £nal states with three partons $q\bar{q}g$ ($O(\alpha_s)$) and with four partons $q\bar{q}q'\bar{q}'$ or $q\bar{q}gg$ ($O(\alpha_s^2)$). Another way to describe this process is the so-called Parton Shower model. In this model three basic interactions between partons are used repeatedly in order to describe the evolution of the process. Those interactions are: $q \rightarrow qg$, $g \rightarrow q\bar{q}$ and $g \rightarrow gg$. The probabilities of these processes depend on the type of vertex, the momenta of the partons, and on a mass scale at which the coupling constant $\alpha_s(Q^2)$ has to be calculated. The Altarelli-Parisi equations de-

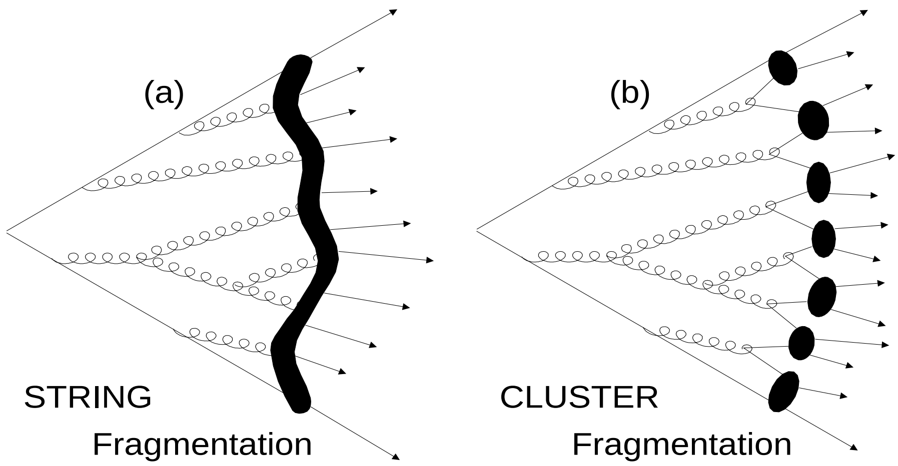

Figure 1.10: *An illustration of string fragmentation (a) and cluster fragmentation (b).*

scribe the evolution of those probabilities when the partons proceed from initial state to £nal state. At a mass scale for virtual partons of about 1.5 GeV/c^2 the cascade is stopped. The Monte Carlo program JETSET [9] includes these two alternative strategies to simulate the production of a multi-parton £nal state.

- **Region 3:** here coloured partons have to £nd one or more partners to form colourless hadrons. Currently, there are several models that describe this process: the model of Independent Fragmentation [10], the *String* model [11], and the *Cluster* model [12].

  The approach applied in the Independent Fragmentation model assumes that the fragmentation of any system of partons can be described as an incoherent sum of the fragmentation of each individual quark. A quark q carrying a certain energy combines with antiquark $\bar{q}$ to form a meson $q\bar{q}_1$-state. The antiquark $\bar{q}_1$ stems from a quark-antiquark pair $q_1\bar{q}_1$ created out of the vacuum. The meson gets an energy fraction z of the initial quark q with the probability $f(z)$:

  $$f(z) = 1 - a + 3a(1-z)^2, \text{ with } a \approx 0.77.$$

  The remaining quark q_1 has an energy fraction $1 - z$, it can pick up another antiquark $\bar{q}_2$ from the vacuum.

  The Cluster model forces gluons produced in the perturbative phase to split into quark-antiquark pairs and then forms colourless clusters from the quarks, see Figure 1.10 b. Each of these clusters either decays into lower class clusters or decays directly into two hadrons, depending on its mass.

  The String model is a phenomenological QCD-motivated model. It realises the QCD con£nement (quark and gluons cannot be free particles) by assuming that a colour-¤ux tube spans all the partons produced in the perturbative phase, see Figure 1.10 a. As the distance between the partons becomes larger, the potential between them rises linearly (the tube (or string) is stretched) with a coef£cient k ($k \approx 1$ GeV/fm) leading to con£nement. Eventually the string breaks up, producing a new quark-antiquark pair $q\bar{q}$. The new $q\bar{q}$ pair gains its energy from the potential energy of the string. This implies that the massive quarks must travel a distance to materialise, which depends on their mass. Thus quark-antiquark pair production in the string is suppressed by a factor

$$exp(\frac{\pi}{k}(-m_q^2 - p_t^2)). \tag{1.27}$$

Each new quark obtains a transverse momentum p_t (with respect to the string). The p_t is assumed to be Gaussian distributed with σ_t ($\sigma_t \approx 0.3$GeV/c) and to be ¤avour independent. From the tunnelling probability it follows that heavy ¤avour (c and b) production in the string is strongly suppressed and this is supported by the experimental fact that heavy quarks are almost always primary quarks. The production of s-quark is suppressed by a factor ≈ 0.3 with respect to u or d; this strangeness suppression factor γ_s is a free parameter of the Monte Carlo model. The longitudinal momentum distribution is determined by the fragmentation function:

$$f(z) \sim \frac{(1-z)^a}{z} exp(-b\frac{m_t^2}{z}); \qquad z \equiv \frac{(E+p_{||})_{hadron}}{(E+p)_{quark}}, \tag{1.28}$$

Herein, $p_{||}$ is the hadron momentum component that is parallel to the momentum of the original quark; $m_t^2 = m_q^2 + p_t^2$; a and b are the so-called fragmentation parameters. This parameterisation describes rather well the light quark (u, d, s) fragmentation, but fails to do so for heavy quarks (c, b). It was observed at LEP that the Peterson fragmentation function [13]:

$$f(z) \sim \frac{1}{z} \cdot \left(1 - \frac{1}{z} - \frac{\epsilon_q}{1-z}\right)^{-2}; \qquad q = c, b \tag{1.29}$$

gives a good description of the fragmentation of heavy quarks. ϵ_q is a ¤avour dependent parameter which is proportional to $1/m_q^2$ and has to be determined experimentally. The values of ϵ_q for b- and c-quarks are $-2.8 \cdot 10^{-3}$ and $-3.7 \cdot 10^{-2}$ [14], respectively.

- **Region 4:** hadrons created during the fragmentation phase will, if unstable, decay into stable particles. The Monte Carlo programs rely here on measured masses, decay widths, branching ratios and quantum numbers of the particles.

The Monte Carlo program used in the analysis is JETSET 7.3 PS. It incorporates the $\mathrm{e^+e^-} \to \mathrm{Z}^0/\gamma \to q\bar{q}$ process, the Parton Shower model, the string fragmentation model and all available information about particles lifetimes, branching ratios etc. More details on the determination of the free parameters of the JETSET model will be given in Chapter 6.

Chapter 2

DELPHI experiment

DELPHI (DEtector with Lepton, Photon and Hadron Identi£cation), is a detector for e^+e^- physics, with special emphasis on particle identi£cation, three-dimensional tracking information, high granularity and precise vertex determination. It is installed at the Large Electron and Positron collider (LEP) at CERN where it has operated since 1989. Figure 2.1 shows a cut-away view of the DELPHI detector, which consists of a central cylindrical (or "barrel") section and two end-caps (or "forward" sections), one of which is shown; the overall length and diameter are over 10 m.

Bunches of electrons and positrons travel in opposite directions inside the vacuum pipe (shown as the black tube through the centre) and meet in the middle of the detector. Occasionally an electron and a positron pass close enough to each other to collide and annihilate each other. The products of the annihilation ¤y radially outwards.

The DELPHI detector has been described in detail elsewhere [15]. Only the components relevant for this analysis will be discussed. The adopted reference frame is a right-handed frame with the z axis along the direction of the incoming e^- beam. The polar angle θ is de£ned with respect to this axis, the azimuthal angle ϕ in the $R\phi$ plane orthogonal to this direction.

2.1 The tracking system

In the barrel region, the Tracking System is composed of cylindrical coaxial detectors: the Vertex Detector (VD), the Inner Detector (ID), the Time Projection Chamber (TPC) and the Outer Detector (OD). In the forward region ($11^\circ \leq \theta \leq 33^\circ$ and $147^\circ \leq \theta \leq 169^\circ$) the tracking system is completed with two sets of drift chambers placed at $\pm$ 160 cm (FCA) and $\pm$ 270 cm (FCB) in z.

A super-conducting solenoid surrounding the whole tracking system—7.5 m long and with inner diameter R_{in} = 5.2 m—generates a high magnetic £eld of 1.23 T coaxial with the beam direction. It is used for the measurement of the charged particle momenta. The trajectory of each charged particle is a helix in this magnetic £eld with a radius proportional

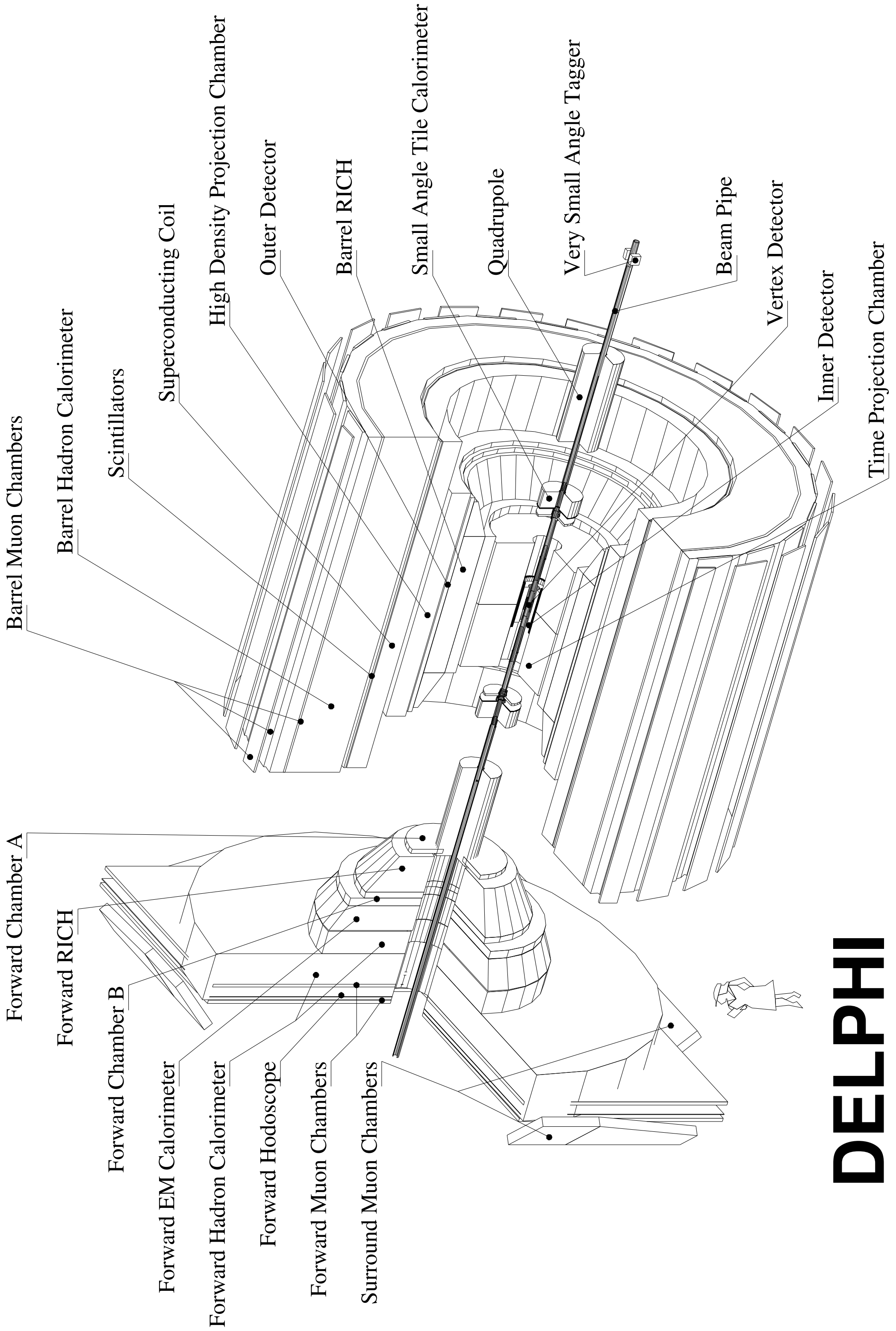

Figure 2.1: *A schematic cut-view of DELPHI detector*

to the transverse momentum of the particle. The average momentum resolution, depending on the detectors included in the £t, ranges from $\delta p/p^2 \simeq 0.001$ to $0.01\ (\mathrm{GeV/c})^{-1}$.

In the following DELPHI's tracking sub-detectors are described starting from the centre of the detector towards larger radii.

The Vertex Detector

The Vertex Detector (VD) is the detector nearest to the interaction region. It consists of 3 concentric layers of silicon micro-strips located at average radii of 6.3 cm, 8.8 cm and 10.9 cm. Each layer has 4 modules in the z direction and 24 modules in $R\phi$. For polar angles of $44^\circ \leq \theta \leq 136^\circ$, a particle crosses all three layers of the VD. The VD provides $R\phi$ coordinates of charged tracks close to the interaction point. This improves the reconstruction of the primary vertex and of secondary vertices from heavy ¤avour decays. At the start of 1994, the £rst (Inner) and third (Outer) layers were equipped with double-sided silicon detectors, giving also measurements in the z direction. The polar angle coverage of the inner layer was increased to $25^\circ \leq \theta \leq 155^\circ$. The performance indicator for a vertex detector is the resolution on the impact parameter. The impact parameter is the distance between the primary vertex and the track at its closest approach to this vertex. The uncertainty of the impact parameter as a function of momentum and polar angle, θ, can be parameterised for the DELPHI detector by:

$$\sigma_{R\phi} = 20 \oplus \frac{65}{p[\mathrm{GeV/c}]\sin^{\frac{3}{2}}\theta}\ \mu\mathrm{m}$$
$$\sigma_{Rz} = 39 \oplus \frac{75}{p[\mathrm{GeV/c}]\sin^{\frac{5}{2}}\theta}\ \mu\mathrm{m}$$

There are two contributions: the £rst one comes from the single point (hit) resolution of the silicon detector and the second one is determined by the multiple scattering in the material of the detector. On average the equivalent point precision is 10.8 μm in $R\phi$ and 13 μm in Rz.

The Inner Detector

The Inner Detector (ID) is a cylindrical wire chamber covering polar angles between 29° and 151° with inner radius of 12 cm and outer radius of 28 cm. It immediately surrounds the Vertex Detector and consists of two major parts: the Jet Chamber and the Trigger Layers.

The Jet Chamber occupies the region between 12 cm and 22 cm radii and is segmented azimuthally into 24 sectors. Each sector is a separate drift chamber with the electric £eld arranged in such a way that drifting electrons—ionization electrons created in the gas by charged particles passing through the chamber—have a constant angular velocity towards the centrally located anode plane. The anode plane comprises 24 anode wires. The drift time information of (up to) 24 anode wires gives an accurate $R\phi$ track element of about 10 cm long. The single wire precision varies from 75μm to 125 μm depending on the drift distance.

This corresponds to a local track element precision of $\sigma(R\phi) = 50\mu\mathrm{m}$ and $\sigma(\phi) = 1.5$ mrad. The measured position of the local track element has a left-right ambiguity.

The Trigger Layers are located between radii of 23 cm and 28 cm. They consist of 5 layers of Multi Wire Proportional Chambers (MWPC's). For an isolated track the z precision from a single MWPC layer varies from 0.5 to 1.0 mm depending on θ.

From the beginning of 1995 a new longer ID is in use. The polar angle acceptance has been increased to $15° \leq \theta \leq 165°$. The Jet Chamber has exactly the same wire con£guration as the previous one. It has an average single wire precision of $85\mu\mathrm{m}$ and local track element precision of $\sigma(R\phi) = 40\mu\mathrm{m}$ and $\sigma(\phi) = 0.89$ mrad. Surrounding the Jet Chamber there are now 5 cylindrical layers of straw tube detectors (192 tubes per layer) measuring $R\phi$. There is no longer any z measurement.

The Time Projection Chamber

The Time Projection Chamber (TPC) is the main tracking device of DELPHI. It provides three-dimensional information on the trajectories of charged tracks. It is a cylinder—inner radius 30 cm, outer radius 122 cm and 2.7 m long—divided into two drift volumes which are separated by a HT (High Tension, -20kVolts) plate producing an electric £eld of 150 Volts/cm. A charged particle crossing the TPC produces by ionization around 70 electrons per cm traversed in the gas—a mixture of 80% Argon (Ar) and 20% Methane (CH_4) at atmospheric pressure. Under the action of the electric £eld these primary electrons drift towards the end plates, which are equipped with MWPCs. The MWPCs are arranged in $60°$ segments. In total there are 2x6 segments. Each MWPC has 16 cathode pad rows concentric with the beam pipe. For polar angles in the range $39° \leq \theta \leq 141°$, they allow the reconstruction of (up to) 16 space points per particle trajectory at radii between 40 and 110 cm. For polar angles $20° \leq \theta \leq 160°$ at least three space points are available per track. In front of the pad plates there is the anode grid which contains 192 sensitive wires per sector. The charge deposited by each track on these wires is used to estimate the energy loss of the particle (dE/dx).

The TPC has an average single point resolution of 230 $\mu\mathrm{m}$ in the $R\phi$ plane and 900 $\mu\mathrm{m}$ in z. The double track separation was measured to be $\Delta_{R\phi} = $ 2cm and $\Delta_z = 1\mathrm{cm}$. The resolution of the dE/dx measurement for minimum ionising particles is 6.2%.

The Outer Detector

The Outer Detector (OD) consists of 5 layers of drift tubes located between radii of 197 and 206 cm. The 4.7 m long drift tubes with cross-sections of 1.65x1.65 cm^2 operate in the limited streamer mode. Successive layers are staggered and adjacent modules of 24 azimuthal sectors overlap, giving full azimuthal coverage. The polar angle acceptance is $42° \leq \theta \leq 138°$. The single point precision in $R\phi$ is 110 $\mu\mathrm{m}$ independent of the drift distance. Three internal layers are equipped with TDCs to measure the z coordinate by timing the signals at the ends of the anode wires. The precision in the z coordinate is $\sigma(z)$ = 3.5 cm.

The OD has a fast readout, which allows the information to be used in the trigger.

The Forward Chamber A

At each side of the TPC, three modules of the Forward Chamber A (FCA) are mounted. Their distance to the interaction point amounts to about 160 cm in z. A module consists of 2 staggered planes of drift tubes, operated in limited streamer mode. The wire orientation in successive modules is rotated by $120°$. The FCA covers polar angles of $11° \leq \theta \leq 32°$ and $148° \leq \theta \leq 169°$. The reconstructed track elements have a precision of $\sigma(x) = 290\mu\text{m}$, $\sigma(y) = 240\mu\text{m}$, $\sigma(\theta) = 8.5\text{mrad}$. $\sigma(\phi)$ averaged over θ is 24 mrad.

The Forward Chamber B

The Forward Chamber B (FCB) is a drift chamber at a distance of about $|z|$=275 cm from the interaction point. The chamber consists of 12 sense-wire planes. The planes in groups of four have wire orientations of $\pm 60°$ with respect to the x-axis. The sensitive area of FCB corresponds to polar angles of $11° \leq \theta \leq 36°$ and $144° \leq \theta \leq 169°$. The track elements are reconstructed with resolutions $\sigma(x, y)$ = 150 μm, $\sigma(\theta)$ = 3.5 mrad and $\sigma(\phi)$ = 4.0 mrad/sin θ.

The Muon detection system

The Muon detection system is divided into three parts: the Barrel MUon chambers (MUB), The Forward MUon chambers (MUF), and, since 1994, an additional layer of Surrounding Muon Chambers (SMC). All chambers are simple drift chambers positioned inside and on the outside of the iron yoke (see Figure 2.1).

The MUB consist of 1372 drift chambers arranged in 24 sectors on the A ($z < 0$: $91.5° \leq \theta \leq 127.0°$) end and C ($z > 0$: $53.0° \leq \theta \leq 88.5°$) end of DELPHI. Each sector contains three modules of chambers, the inner module is embedded in the HCAL, the outer and peripheral modules lie on the outside of DELPHI. The peripheral modules cover the holes in the coverage of the other modules in adjoining sectors. The resolution obtained for extrapolated tracks is $\sim$ 0.3 cm in $R\phi$ and $\sim$ 1.8 cm in z.

Both arms of the MUF consist of two layers of chambers covering the angular regions $9° \leq \theta \leq 42°$ and $138° \leq \theta \leq 171°$. One layer is located inside the yoke after 85 cm of iron and the second is 30-cm away from the yoke. The resolution is $\sim$ 5 mm in the xy plane.

The SMC £lls the gap between the barrel and forward regions: $42° \leq \theta \leq 53°$ and $127° \leq \theta \leq 138°$. It provides space point measurements with an accuracy of about 1 cm.

2.2 Energy measurement

The energy of electrons and photons is measured with an electromagnetic calorimeter. It is based on the fact that electrons and positrons radiate a considerable part of their energy as photons when decelerated in the intense £eld close to a nucleus. This radiation is called bremsstrahlung. The intensity of this radiation is inversely proportional to the square of the mass of the incident particle. This affects in particular electrons and positrons, which are stopped in the calorimeter, while hadrons ($\pi^{\pm}$, $\mathrm{K}^{\pm}$, p, $\overline{\mathrm{p}}$) and muons, μ, will generally pass through. Moreover, photons with energy above $2m_ec^2$ may convert to an electron-positron pair in the electric £eld of a nucleus. Electrons and positrons which emerge from a conversion can, if energetic enough, radiate further bremsstrahlung photons which in their turn may convert. The result is that an electromagnetic shower develops containing a roughly equal mixture of electrons, positrons and photons.

The barrel electromagnetic calorimeter, HPC, is located inside the magnetic £eld. It consists of 144 modules arranged in 6 rings inside the magnetic £eld along the length of the detector. Each ring consists of 24 modules, each with an inner radius of 208 cm and an outer radius of 260 cm. A module is a small TPC. Lead layers serve as converter material and provide a drift £eld. The total converter thickness is $18X_0/\sin\theta$. In the module there are 128 pads arranged in 9 rows. Electron and positrons produced in the electromagnetic shower create ionisation electrons in the gas volume, and these electrons deposit the charge on pads. The charge collected on a pad is sampled in 256 time slots, providing very high granularity in z. The shower position is measured with σ_θ = 1 mrad and σ_ϕ = 1.7 mrad. The energy resolution of photons/electrons can be parametrised as $\sigma(E)/E = 0.043 \oplus 0.32/\sqrt{E[\mathrm{GeV}]}$.

The forward electromagnetic calorimeter, FEMC, consists of two arrays of 4532 Cherenkov lead glass blocks; the front faces are placed at $|z| \approx 284$ cm, covering the polar angles $8^\circ \leq \theta \leq 35^\circ$ and $145^\circ \leq \theta \leq 172^\circ$. The blocks are truncated pyramids with inner (outer) face dimensions of 5.0×5.0 (5.6×5.6) cm^2 and depths of 40 cm, corresponding to 20 radiation lengths. Each block is mounted in such a way that it points towards the interaction region. A tilt of $\sim 1^\circ$ was applied to avoid particles escaping undetected, through the cracks between the blocks. The Cherenkov photons induced by the electron and positrons in the shower are read out by a photo-multiplier, coupled to a low noise preampli£er. The energy resolution can be parametrised as $\sigma(E)/E = 0.03 \oplus 0.12/\sqrt{E[\mathrm{GeV}]} \oplus 0.11/E$.

The energy of neutral and charged hadrons—π^+, K^+, p, K^0_L, n and their antiparticles—is measured in hadron calorimeters. In order for hadrons to stop many interaction lengths of material are required. In DELPHI an iron-gas hadron calorimeter is used, the HAC. The HAC consists of the iron return yoke of the super-conducting magnet instrumented with limited streamer mode detectors. The resulting sampling gas detector detects showers either already initiated in the material detector in front of the HAC, or in the calorimeter itself by the incidence of neutral and charged hadrons. The hadron calorimeter covers almost the full solid angle: $11^\circ \leq \theta \leq 169^\circ$. In the barrel region $52^\circ \leq \theta \leq 128^\circ$ the total thickness is 7/$\sin\theta$ hadronic interaction lengths and the energy resolution is found to be $\sigma(E)/E = 0.21 \oplus 1.12/\sqrt{E[\mathrm{GeV}]}$. The £xed term in this expression is due to the material between the hadron calorimeter and the electromagnetic calorimeter. The resolution achieved in z is approximately 10 cm.

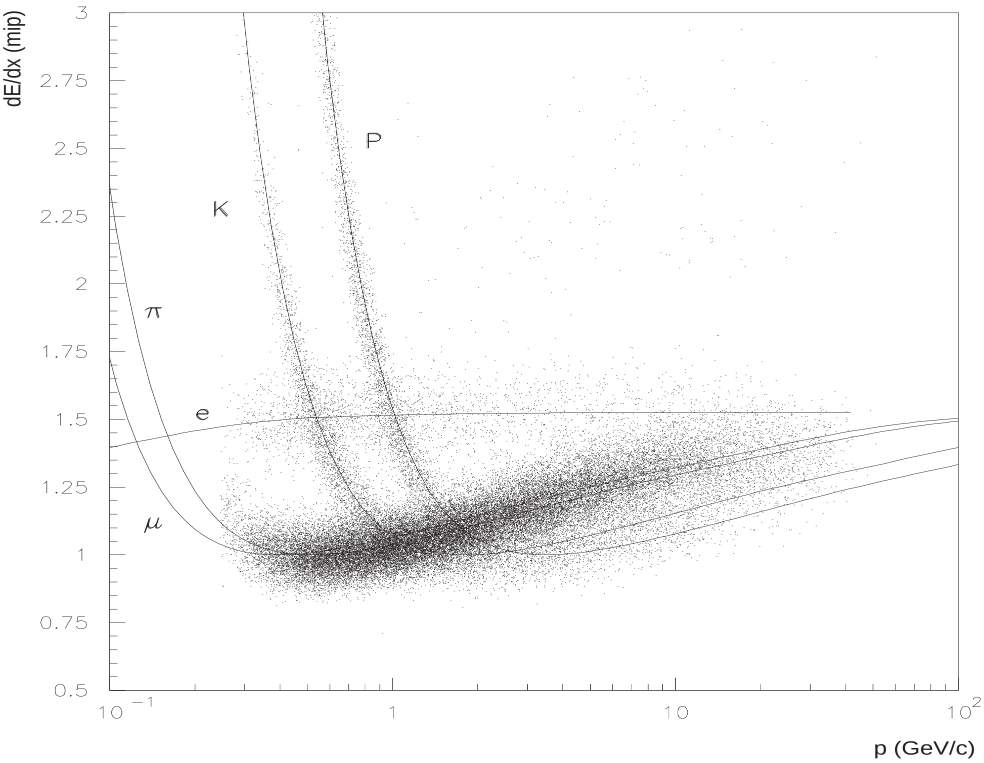

Figure 2.2: *The TPC dE/dx measurement versus momentum.*

2.3 The identi£cation system

As mentioned in the beginning, DELPHI is a detector with special emphasis on particle identi£cation. It has determined the choice as well as the position of the sub-detectors, i.e., the TPC, the electromagnetic calorimeters (HPC and FEMC), the hadron calorimeter (HAC), the muon chambers (MUB, MUF and SMC) and the ring imaging Cherenkov detectors (BRICH and FRICH). The use of Cherenkov detectors makes DELPHI unique among the four detectors installed and operated at LEP.

The identi£cation of particles makes use of the measured ionization loss per unit path length (dE/dx) in the TPC, information of the Ring Imaging Cherenkov detectors, information from the electromagnetic and hadronic showers in the electromagnetic and hadron calorimeters, and information about a possible track in the muon chambers.

The Charged Hadron identi£cation: $\mathrm{p\overline{p}}, \mathrm{K}^{\pm}, \pi^{\pm}$

The ionization loss per unit path length in a medium (e.g., the gas of the TPC) of a singly charged particle with velocity βc ($\beta = p/E$) is inverse-proportional to β and directly proportional to a logarithm of γ ($\gamma = 1/\sqrt{1-(\beta c)^2}$). If the momentum of a charged particle is measured, one can say which mass hypothesis is more probable to have a particular ionization loss—$\mathrm{p}, \mathrm{K}, \pi, \mu, \mathrm{e}$ (see Figure 2.2). The RICH provides a more powerful tool for $\mathrm{p\overline{p}}, \mathrm{K}^{\pm}, \pi^{\pm}$-identi£cation. These detectors and their use for particle identi£cation will be discussed in detail in the following two chapters.

The Electron and Photon identi£cation

Electron and photon identi£cation is provided by the electromagnetic calorimeters—the High density Projection Chamber (HPC) in the barrel region and the Forward Electro-Magnetic Calorimeter (FEMC) in the forward region—using the tracking information from the Tracking System. The clusters of energy deposition in the calorimeters are associated with tracks reconstructed by the Tracking System. If a cluster cannot be associated with a track, then it is assumed to be due to a photon. If a cluster can be associated with a track and the momentum of the track corresponds to the energy of the cluster then the track is identi£ed as an electron.

The Muon identi£cation

Muons are identi£ed by comparing the extrapolations of reconstructed tracks with hits in the muon drift chambers. Muons with momentum larger than 2 GeV/c reach the Muon Chambers.

Chapter 3

DELPHI RICHs

3.1 Cherenkov radiation

P.A.Cherenkov and S.I.Wawilow [16] £rst showed that charged particles moving in a transparent medium may, under certain circumstances, produce electro-magnetic radiation. This Cherenkov radiation was theoretically interpreted by I.E.Tamm and I.M.Frank [17]. The radiation is emitted by the medium under the action of the electro-magnetic £eld of the particle moving in the medium. In particular, electro-magnetic radiation with a frequency ω is produced when a particle has a velocity v that exceeds the phase velocity of waves of that frequency in the medium concerned:

$$v > c/n(\omega), \tag{3.1}$$

where $n(\omega)$ is the refractive index and c is the velocity of light in vacuum. The radiation is emitted in a cone of opening angle $2\theta_c$:

$$\cos\theta_c = c/nv. \tag{3.2}$$

It is distributed over the surface of this cone. The emission of these electro-magnetic waves involves an energy loss by the moving particle[1]. The intensity of the radiation in a frequency interval dω is :

$$\mathrm{d}I = \frac{Q^2e^2}{c^2}(1 - \frac{c^2}{v^2n^2})\omega\mathrm{d}\omega. \tag{3.3}$$

Q is the charge of the particle in units of the electron charge e. This radiation is emitted in an angular interval

[1]It is a fraction of the total energy loss due to the work done against the force exerted on the particle by the £eld which it produces. The value of the effective electric £eld is the difference between the £eld which would be present if the particle was moving in vacuum and the £eld in the dielectric medium. Although the dielectric permeability is assumed to be real (the medium being transparent), it actually has a small imaginary part around $\omega = 0$. This is responsible for the small energy loss due to the Cherenkov radiation. A detailed and simple derivation of this is given by L. D. Landau and E. M. Lifshitz[18].

$$\mathrm{d}\theta = \frac{c}{vn^2 \sin\theta_c} \frac{\mathrm{d}n}{\mathrm{d}\omega} \mathrm{d}\omega \tag{3.4}$$

The number of photons in a given energy interval ΔE, for which the medium is transparent, is obtained by integrating (3.3) over the corresponding frequencies and over the time interval during which the particle traversed the medium of length L. The result is :

$$\Delta N = \frac{Q^2 \alpha}{c\hbar} L \sin^2\theta_c \Delta \mathrm{E} \tag{3.5}$$

α is the electro-magnetic £ne-structure constant, $\hbar$ is Plank's constant, L is the length (in cm) of the particle path in the radiator medium.

3.2 The ring-imaging Cherenkov technique

From formulas (3.1)-(3.5) the following properties of Cherenkov radiation can be derived that are relevant for particle identi£cation :

1. for a particle of mass m and given refractive index, n, there is a *threshold* velocity β_{th} (i.e. momentum $p_{th} = m\beta_{th}/\sqrt{1-\beta_{th}^2}$) below which no radiation is emitted:

$$\beta_{th} = 1/n \quad \text{i.e.} \quad p_{th} = \frac{m}{\sqrt{n^2-1}} \tag{3.6}$$

2. for a given refractive index, the cone over which surface the emitted radiation is distributed has a *maximum* angle, hereafter called *saturated* angle. It is reached when the velocity of the moving particle is close to the speed of light in vacuum:

$$\cos\theta_c^{max} = 1/n \quad \text{for} \quad \beta \simeq 1 \tag{3.7}$$

3. the number of emitted photons is proportional to the sine squared of the Cherenkov angle, which is itself a function of particle momentum. It is also proportional to the path length of the particle in the medium :

$$N_{ph} \propto L \sin^2\theta_c \tag{3.8}$$

4. the angle θ_c depends on the frequency of the Cherenkov radiation, since n is wavelength-dependent, due to chromatic dispersion.

The Ring-Imaging Cherenkov technique, using UV-photon ($E_\gamma \simeq 7$ eV) detectors was £rstly proposed by Ypsilantis and Séguinot [19]. It initiated the development of the DELPHI RICH detectors. The design principle as illustrated in Figure 3.1 is the same for Barrel and Forward RICHs. It can be divided into two parts: photon *production* and photon *detection*.

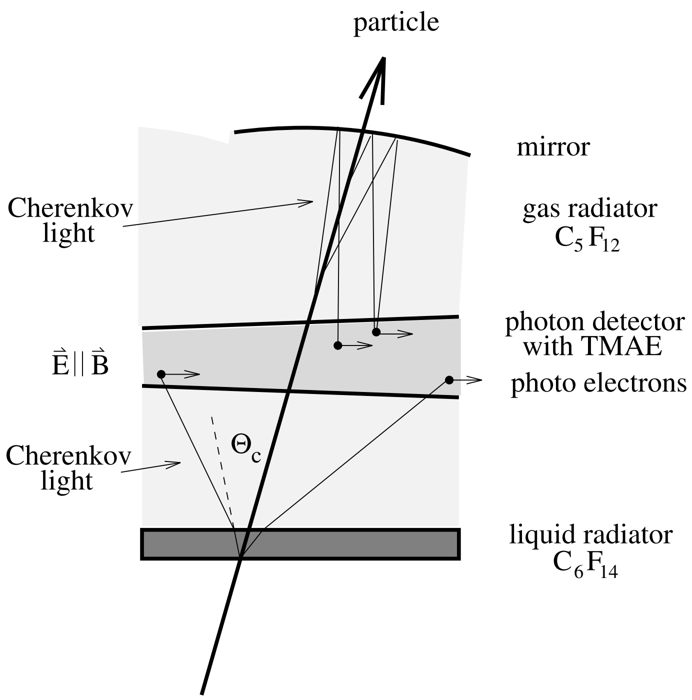

Figure 3.1: *The working principle of the Barrel RICH*

Photon production

In order to perform particle identi£cation over a large momentum range of $0.7 < p < 45.6$ GeV/c, the RICH contains two different radiator media. One is a liquid per¤uorhexane, C_6F_{14}, that is used as the liquid radiator for both RICHs, while per¤uoropentane, C_5F_{12}, and per¤uorobutane, C_4F_{10}, are used for the gas radiators in the Barrel and Forward RICH, respectively. The properties of these substances are given in Table 3.1.

Radiator	Boiling temp. $[°C]$	n at 7 eV	$\frac{\Delta n}{n-1}$ 6.5-7.5 eV	p_{thr} [GeV/c] $\pi^{\pm}$	K$^{\pm}$	p$\overline{\text{p}}$	θ_c^{max} [mrad]
C_4F_{10}	-2	1.001530	3.5%	2.5	8.9	17.0	55.3
C_5F_{12}	28	1.001720(40^oC)	3.0%	2.4	8.4	16.0	58.6
C_6F_{14}	57	1.283	3.3%	0.17	0.6	1.2	677.1

Table 3.1: *Some key properties of the DELPHI radiators.*

The liquid radiators are used to identify particles with momenta below ~ 8 GeV/c. The gas radiators are used for identi£cation of the particles with momentum above $\sim$ 2.7 GeV/c. Figure 3.2 shows the Cherenkov angle as a function of the particle momentum for different types of particles, both in gas and liquid radiators. The Cherenkov light from the thin liquid radiator is projected onto a UV-sensitive photon detector, which converts UV-photons into

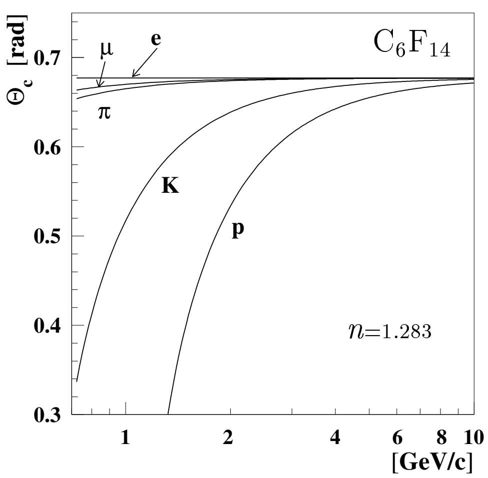

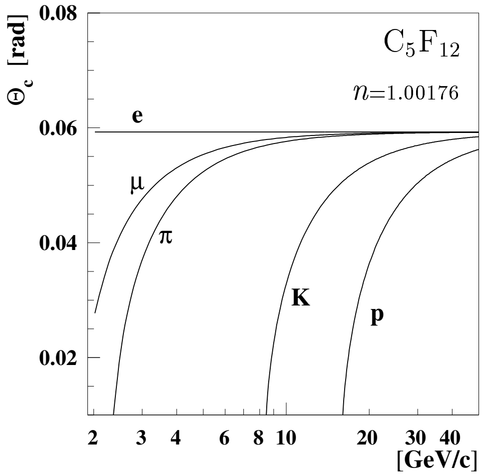

Figure 3.2: *The expected Cherenkov angle versus momentum for two different materials, liquid C_6F_{14} (n= 1.283) and gaseous C_5F_{12} at 1030 mbar.*

photoelectrons. The photoelectrons appear in ring-like or parabolic con£guration, depending on the angle of incidence of the particle. Focusing parabolic (Barrel RICH) or spherical (Forward RICH) mirrors re¤ect the Cherenkov light from the gas radiator and project it on the same photon detector (see Figure 3.1).

Photon detection

The UV-photon detector is a TPC-like device entirely made of quartz to allow UV-photon transmission from both sides. Inside the drift volume, the Cherenkov UV-photons will liberate electrons by ionization of the drift gas. The photosensitive agent in the drift gas, Tetrakis(diMethylAmino)-Ethylene (TMAE), is sensitive to photons of energies higher than $\sim$ 5.5 eV. A homogeneous electric £eld causes the electrons to drift towards the end of the photon detector, where they are detected by a Multi-Wire-Proportional-Chamber (MWPC). The UV-photon detector provides three-dimensional positional information on the UV-photon for each detected photoelectron. In the Barrel RICH, for instance, the MWPC gives $R\phi$ and R coordinates of the point where the Cherenkov photon liberated the photoelectron whereas the z coordinate of this point is obtained from the drift time measurement.

Since the fundamental principle of the DELPHI RICH detectors relies on the detection of UV-photons, it is of utmost importance that the key detector elements are either UV-transparent or UV-sensitive. The main parameters of the BRICH as a function of photon energy are shown in Figure 3.3. The transmission coef£cients correspond to 8 mm quartz (solid line), 1 cm liquid C_6F_{14} (dashed line) and 15 cm gaseous C_5F_{12} (dotted line). The dash-dotted line indicates the TMAE quantum ef£ciency (Q_{eff}^{TMAE}). The hashed area represents Q_{eff}^{TMAE} folded with the quartz UV-transmission coef£cients. It is a measure of the photon conversion ef£ciency of the drift tubes. The lower limit on the energy of the photons is determined by the Q_{eff}^{TMAE} at $\sim$ 5.6 eV (i.e. 160 nm).

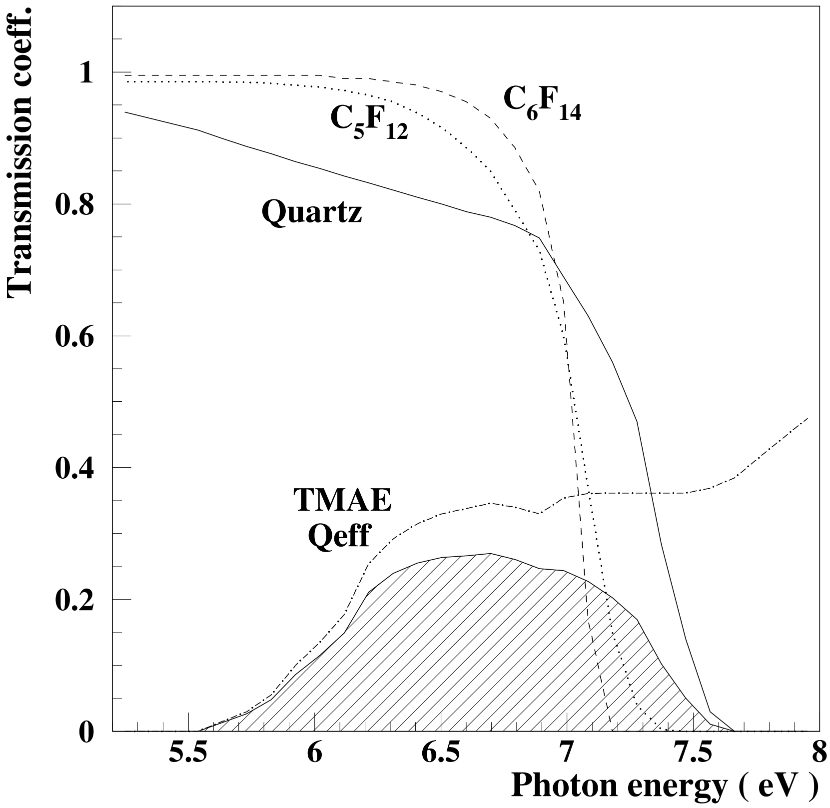

Figure 3.3: *The transmission coef£cients of the detector elements in the Barrel RICH, the quantum ef£ciency of the TMAE and (hashed area) the photon conversion ef£ciency as a function of photon energy.*

From (3.5), the number of detected photons for a particle path length L is given by:

$$N_{ph} = \frac{Q^2\alpha}{c\hbar} L \int \sin^2\theta_c \epsilon(\mathrm{E}) d\mathrm{E} = 370[\mathrm{cm}^{-1}\mathrm{eV}^{-1}] L \int \sin^2\theta_c \epsilon(\mathrm{E}) d\mathrm{E} = N_0 L \sin^2\overline{\theta}_c. \tag{3.9}$$

N_0 is the number of photons for the maximum-saturated-angle, $\overline{\theta}_c$ is the Cherenkov angle averaged over the photon energy interval (see (3.4)) and $\epsilon(\mathrm{E})$ is the ef£ciency for detection of a photon of energy E. This ef£ciency includes all the above-mentioned transmission and quantum ef£ciencies, the mirror re¤ectivity for a photon produced in the gaseous radiator and the inef£ciencies in detecting the photoelectrons.

3.3 The ring-imaging Cherenkov counters

The Barrel RICH

The Barrel RICH [20] is a 3.5 m long cylinder with inner and outer radii of 124 and 197 cm respectively. A mid-wall divides the detector into two mirror-identical halves, referred to as sides A $(\cos\theta < 0)$ and C $(\cos\theta > 0)$. It covers polar angles in the DELPHI detector ranging from $40°$ to $140°$.

Each side of the BRICH is azimuthally divided into 24 sectors. The elements of a sector are one liquid radiator, one drift tube with a wire chamber at its end, and 6 mirrors. An undivided gas radiator volume is common to all sectors (see Figure 3.4).

Particles £rst traverse the liquid radiators, which essentially consist of a 1cm thick layer of C_6F_{14}. Cherenkov photons created in this radiator leave the radiator through the quartz window closing the radiator and enter the drift tubes—the photon detectors—placed 12 cm away from it. The volume of the vessel outside the drift tubes and the liquid radiators is used as gas radiator and £lled with gaseous C_5F_{12}. The vessel is kept at a constant temperature of $40°C$ and a £xed gas pressure of 1030 mbar. Parabolic mirrors re¤ect the Cherenkov photons produced behind the drift tubes back into the drift tubes. The useful path length of particles in the gas radiator is on average 40 cm. The mirrors focus the photons into a ring-like "image" in the drift tube gas. The drift gas is an admixture of methane-ethane $(75\% CH_4 + 25\% C_2H_6)$ with $\sim$ 0.1% TMAE vapour. The TMAE is added by bubbling the main gas mixture through a TMAE bath, which is kept at a constant temperature of $28°C$. A drift £eld of 0.5 kV/cm, which is determined by the VHV = 80 kV and the 150 cm drift tube length, transports the photoelectrons towards a MWPC at the end of the drift tube. Each MWPC has 128 anode wires with an inter-distance of 2.62 mm and 8 groups of 16 cathode-strips (3.8 mm wide) perpendicular to the anode wires. The chambers are operated at a gas ampli£cation gain of about 10^5, implying that a single photoelectron induces an avalanche of in the average 10^5 electrons. Photo-conversion points are reconstructed in three dimensions: the anode wire address provides the $R\phi$ coordinate ($\Delta_{R\phi} = 1.0 - 2.0$ mm), the cathode pad address gives the R coordinate and the z coordinate is determined from drift time measurement. Using this information and the position and direction of the particle as measured by the tracking detectors of DELPHI, it is possible to calculate for each photon the Cherenkov angle.

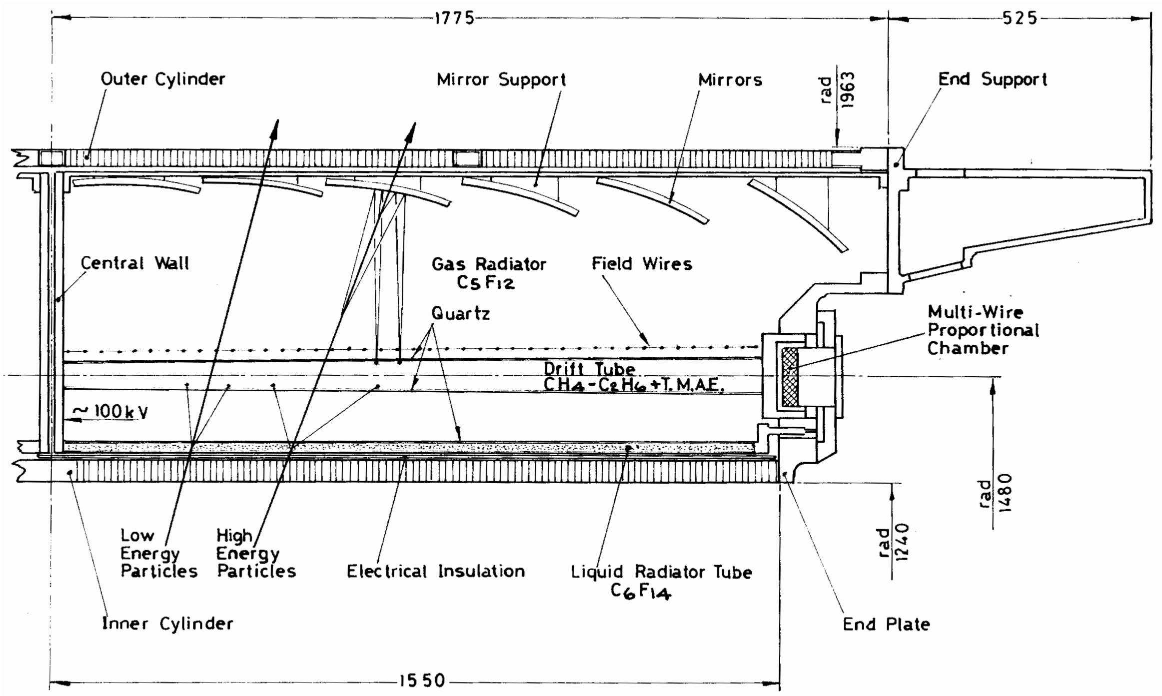

Figure 3.4: *A schematic view of the DELPHI Barrel RICH detector*

The calibration system of the BRICH consists of a UV-light source which injects UV light into each drift tube at 45 accurately known points, arranged in 5 rows of 9 £bers. It determines the drift velocity with 0.07 % accuracy ($V_d = 5.3$ cm/μs in the BRICH) and monitors the drift velocity during data taking due to variations of temperature, pressure, gas mixture etc.

The Forward RICH

The Forward RICH [21] covers both end-cap regions of DELPHI over polar angles $15° \leq \theta \leq 35°$ and $145° \leq \theta \leq 165°$, see Figure 2.1. Although very different in geometry, the Barrel and Forward RICH employ the same principles. A major practical difference is that in the Forward RICH the electric £eld in the photon detector is perpendicular to the magnetic £eld of DELPHI. It also operates with different gases.

Each Forward RICH detector consists of two $180°$ segments, which join in the vertical plane. The design is schematically shown in Figure 3.5. A segment is divided azimuthally into 6 sectors. Each sector contains one drift box with two MWPCs, three liquid radiator containers and £ve spherical mirrors. C_4F_{10} is used for the gas radiator. It £lls the remaining volume of the segment. Because of its low boiling temperature of -2^oC no heating is required. It can be used at atmospheric pressure because of its stable ($\sim$ 100%) UV-transparency over the full photon energy window of interest, 6.5 - 8.0 eV. The average path length inside the gas radiator is about 60 cm.

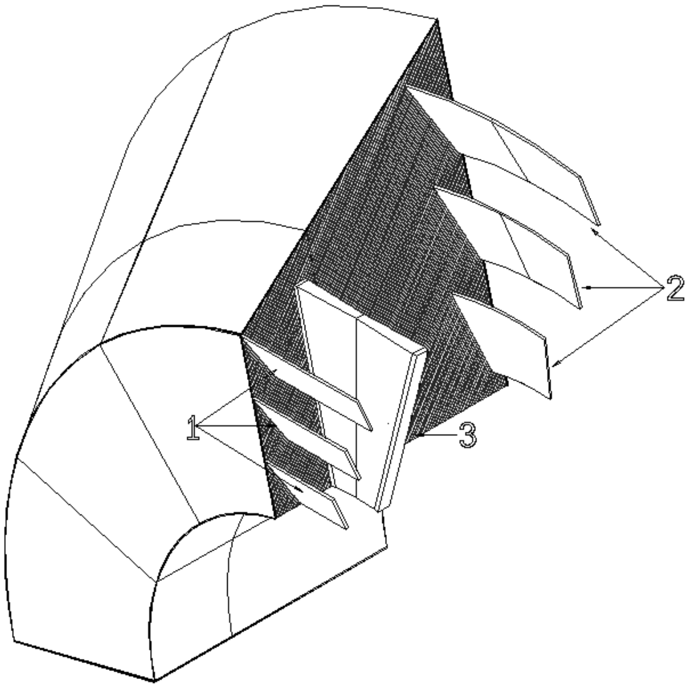

Figure 3.5: *A schematic view of a sector of DELPHI Forward RICH. 1 = liquid radiator containers, 2 = spherical mirrors, 3 = photon detector.*

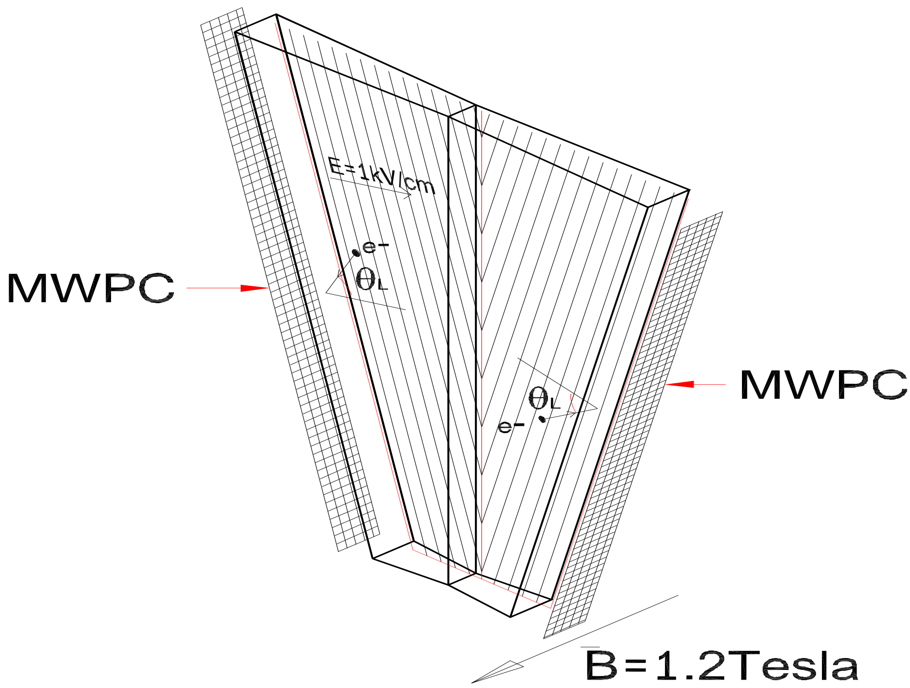

Figure 3.6: *A schematic view of photon detector in Forward RICH*

The photon detector has a trapezoidal shape, see Figure 3.6. It consists of a drift volume which is electrically divided in two symmetric halves, each read out by a MWPC. Both plain sides of the detector are made of fused quartz. The depth of the drift volume varies from 60 mm near the MWPCs to 40-54 mm along the mid-wall. The photoelectrons drift in a plane perpendicular to the 1.2 T magnetic £eld. This results in a Lorentz angle of $\sim 50^\circ$ between the drift trajectories and the electric £eld and has important consequences for the MWPC design and for the choice of drift gas. The gas used is C_2H_6, which is made photosensitive by bubbling it through liquid TMAE. The detection plane of each MWPC has 320 anode wires with a 2.62-mm pitch and 240 cathode strips, 5 mm wide and 42 mm long. The cathode strips are arranged in 20 groups of 12 strips. Each group of 12 strips is covered by 16 anode wires. The addresses of the anode wires and the cathode strip together with the drift time information allow the reconstruction in space of each photoelectron production point. The resolution $(\sigma_x, \sigma_y, \sigma_z)$ is about (0.8, 0.8, 1.5) mm. It is the dominant error in the determination of the angle of the Cherenkov photon in the gas radiator.

With the UV-calibration system, both drift velocity and Lorentz angle are measured precisely.

Cherenkov photoelectrons

The potential of the RICH to identify particles is given by measuring the separation between the particle bands in Figure 3.2 in units of the resolution on the Cherenkov angle. The Cherenkov angle is determined from the image produced by the Cherenkov light cone in the photon detectors. The image is the cross-section of a cone. The shape therefore can be either a ring, ellipse, parabola or hyperbola [2]. We nevertheless will use the term "ring" for all these shapes. From (3.9) it follows that the number of photoelectrons per ring varies with the Cherenkov angle. The number has a Poisson distribution with average N_{ph}. Experimental data for 45.6 GeV/c muons show an average of 18.6(7.9) and 8.3(5.2) Cherenkov photons per track for the BRICH (FRICH) liquid and gas radiators, respectively. There is a small background from other sources as one can see in Figure 3.7.

As was mentioned above, the Cherenkov angle is calculated for each detected photoelectron. Its uncertainty, σ_{ph}, is given by the quadratic sum of several contributions. For photons from the gas radiator one has:

$$\sigma_{ph}^2 = \sigma_{chrom}^2 + \sigma_{bend}^2 + \sigma_{position}^2. \tag{3.10}$$

The σ_{chrom} is the contribution due to chromatic aberration (see (3.4)). The bending of the particle trajectory in the 1.2 T magnetic £eld of DELPHI on its way through the gas radiator—it smears the Cherenkov angle in one direction—gives the term σ_{bend}. This term depends on the transverse momentum of the particle $(p \sin\theta_p)$, the track length (l) inside the gas radiator and the azimuthal position of the photon (ϕ) on the Cherenkov cone:

$$\sigma_{bend} \propto \frac{l \mid \sin\phi \mid}{p \sin\theta_p}. \tag{3.11}$$

[2]The conic-like section shape is due to internal re¤ection of the Cherenkov light inside the liquid radiator.

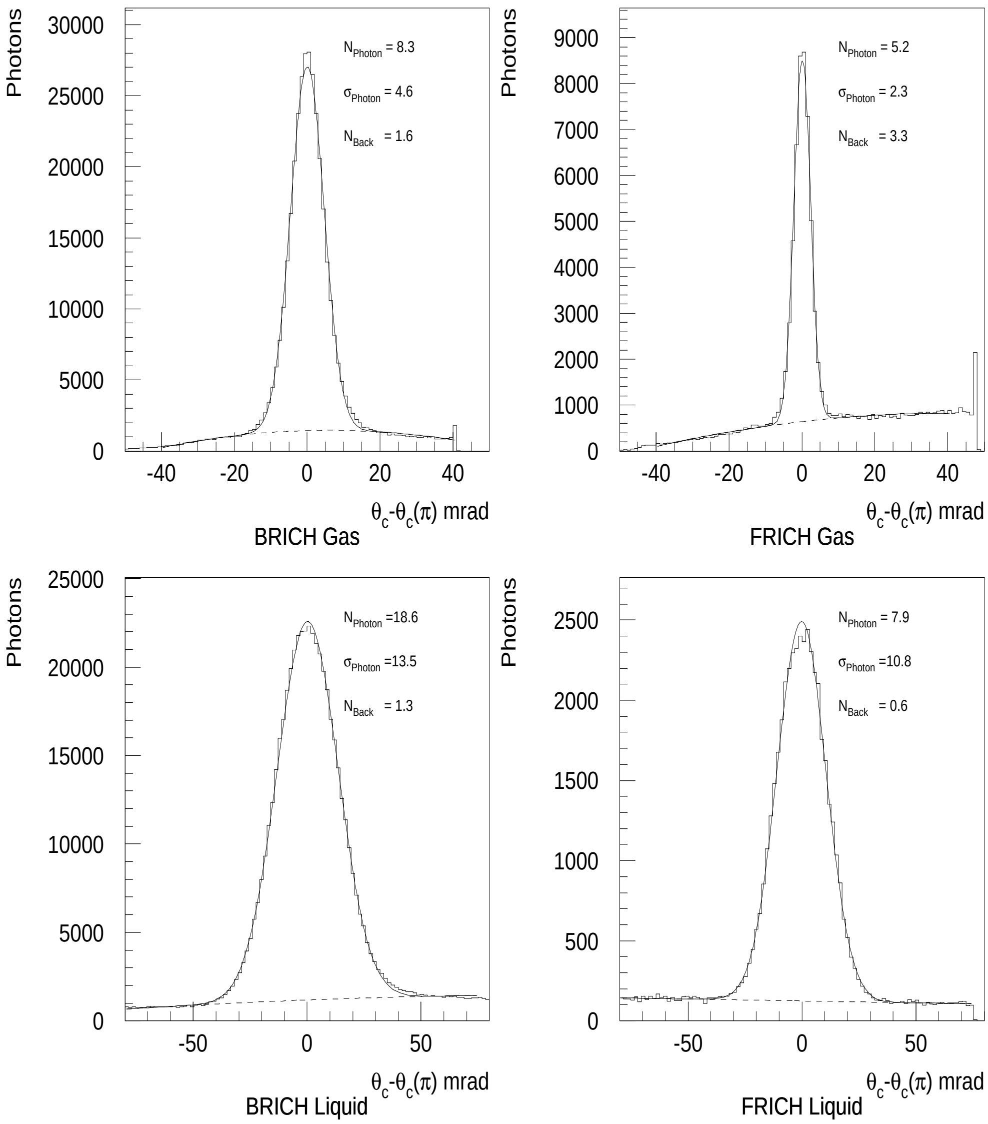

Figure 3.7: *Distributions of the photoelectron Cherenkov angles, for $Z^\circ \rightarrow \mu^+\mu^-$ events. The average number of photoelectrons and measurement precision of the Cherenkov angle for single photons are given for both radiator types, gas and liquid, in both the Barrel and Forward RICH.*

Finally, $\sigma_{position}$ is due to the £nite position resolution of the photon detector: it comprises diffusion during the drift of the photoelectron and the intrinsic resolution of the wire chamber that detects the signal from the photoelectron.

For liquid radiator photons, the term σ_{geom} replaces the term σ_{bend}. It takes into account the fact that the liquid radiator layer has a £nite depth and this gives an uncertainty on a Cherenkov photon production point.

The number of photons associated with a track and their Cherenkov angles are the input to the particle identi£cation algorithm.

3.4 Preparing of raw data for ring analysis

The simulation of the RICH data is done in great detail. It takes into account the production of Cherenkov photons, their conversion into photoelectrons, the production of background electrons from all known sources and the response of the detector to all these electrons. Therefore, the simulated data can be analysed in the same manner as the real data.

The sets of photons associated with tracks are hereafter called the raw data. This applies to both real and simulation data. In the following we describe the different steps that prepare the raw data for the ring analysis.

Background rejection

First, the signal-to-background ratio for photons should be improved in the raw data.

The RICH photon detectors detect single photoelectrons and, as a consequence, are very sensitive to background. Background sources are:
1) electronic noise and after-pulses which can imitate photoelectron signals;
2) cross-talk—one photoelectron giving a signal in two strips;
3) photon-feedback—UV-photons created during the development of the avalanche causing secondary avalanches [3];
4) ionization electrons (dE/dx) caused by the tracks passing through the drift tube;
5) δ-rays produced by tracks passing the drift tubes;
6) UV-photons produced when the particle traverses the quartz windows;
7) γ-ray conversions.

Most of these background sources lead to clusters of electrons. Figure 3.8 illustrates such a cluster of background electrons. It is a $R\phi$-cluster in local coordinates. By removing such $R\phi$ clusters we improve the signal-to-background ratio by a factor 5, while rejecting only 15% of the true signal as shown for liquid rings in Figure 3.9. Background is a more serious problem for the liquid radiator rings than for the gas radiator rings as it depends, for most sources, on the ring area. Although the background in the RICHs is complicated, it has been successfully simulated in the Monte Carlo.

[3]To absorb most of these UV-photons, UV-blinds are installed between the individual anode wires, allowing only photon-feedback on the same wire.

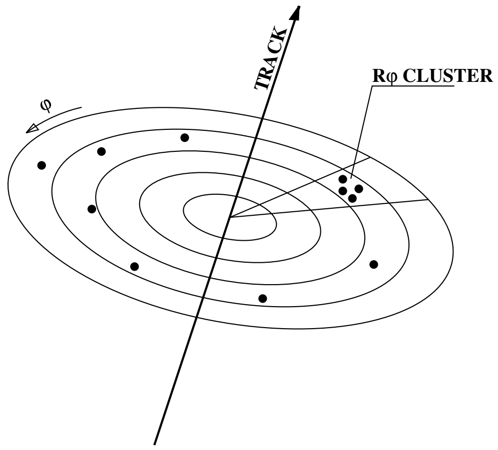

Figure 3.8: *An illustration of a background R_ϕ-cluster*

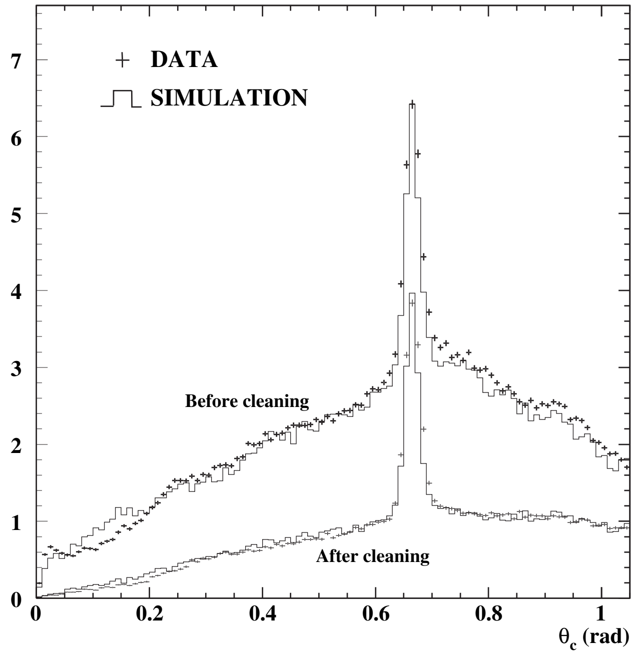

Figure 3.9: *Comparison of the BRICH real and simulated data before and after the cleaning procedure for liquid radiator rings.*

Alignment

Secondly, the off-line alignment of the RICH is performed. It adjusts the refractive indices and geometrical positions of the different detector components. For the BRICH this amounts to the adjustment of 288 mirrors, 48 radiator trays and 48 photon-detectors. It is done by minimising the width of the θ_c-distribution for the muon tracks from $Z^0 \to \mu^+\mu^-$ events. These events have well isolated tracks that produce Cherenkov rings with a very low background. The expected Cherenkov angle depends only on the refractive index whereas the measured one also depends on the position of the detector elements. For example, a 1 mm shift of the photo-detector position for the FRICH is equivalent to a decrease of 10% in the Cherenkov angle resolution for the gas radiator.

Fixing

Finally, several corrections that could not be taken into account in the previous two steps are determined and applied to the raw data in real and simulated data. It includes corrections that have been determined by comparing real and simulated data, e.g., inef£ciencies as a function of polar angle and other acceptance problems; differences in the expected resolution of the Cherenkov angle and in the expected number of photons, and the photon-feedback effect. In addition it corrects for non-uniformities in the refractive indexes of the gas radiator. All these corrections are made by the RICFIX-package [22]. The RICFIX-package obtains most of its information using $Z^0 \to \mu^+\mu^-$ events but applies the corrections to all Z^0-data.

3.5 Ring £nding procedure: RIBMEAN Algorithm

Several ring £nding algorithms [23] have been developed to combine all information from the detected photoelectrons for particle identi£cation. The RIBMEAN algorithm [24] is used in the analysis presented in this thesis. It determines the number of Cherenkov photons in the ring and their mean Cherenkov angle.

The starting point of the method is a set of photoelectrons associated with a track. Each of these photoelectrons has a Cherenkov angle θ_i, an expected error σ_{θ_i}, a depth of the conversion point in the chamber, a ϕ position of the photon on the ring, and a quality bit that re¤ects whether the photon is isolated, ambiguous or not. The photon ambiguity comes from two kinds of ring overlaps: the £rst, when the rings from different tracks are overlapping and, the second, when the rings from the gas and liquid radiators are overlapping. A non-isolated photon means that it belongs to some small $R\phi$-cluster but one can not ascertain whether it has a background origin and, therefore, was not rejected in the background rejection step.

Photons are given different weights depending on the signal-to-background ratios. Backgrounds differ considerably for different types of photons. In particular, the background is higher for

1. ambiguous than for non-ambiguous photons;
2. non-isolated photons than for isolated ones;
3. photons that have a low conversion probability (the probability is obtained from the depth of the conversion point);
4. photons near the open end of the parabola (this is the case for photons originating from the Barrel RICH liquid radiator).

Figure 3.10 shows the effect of applying weights to the single photon distribution. The solid line shows the Cherenkov angle distribution for single photons as determined for simulated pions in the liquid (gas) of the barrel (forward) RICH after applying these weights. The dashed line shows the same distributions with a weight equal to 1. The effect on photons from the liquid radiator is larger that on those from the gas radiator. This is because the liquid radiator rings have a bigger size and therefore are more in¤uenced by the above-mentioned backgrounds.

To reconstruct a ring the algorithm starts with £ve ring hypotheses corresponding to the assumption that a track is due to an electron, muon, pion, kaon or proton. For each hypothesis one tries to £nd photoelectrons that are consistent with the corresponding ring. The ring £nding starts with the photoelectron that has the smallest distance to this particular hypothesis. In the following steps other photoelectrons are sought that can be associated with the hypothesis. This is done by looking successively for a photoelectron with an angle θ_i that has a distance of less than 2.5 σ_{θ_i} to the weighted average of the angles of the previously

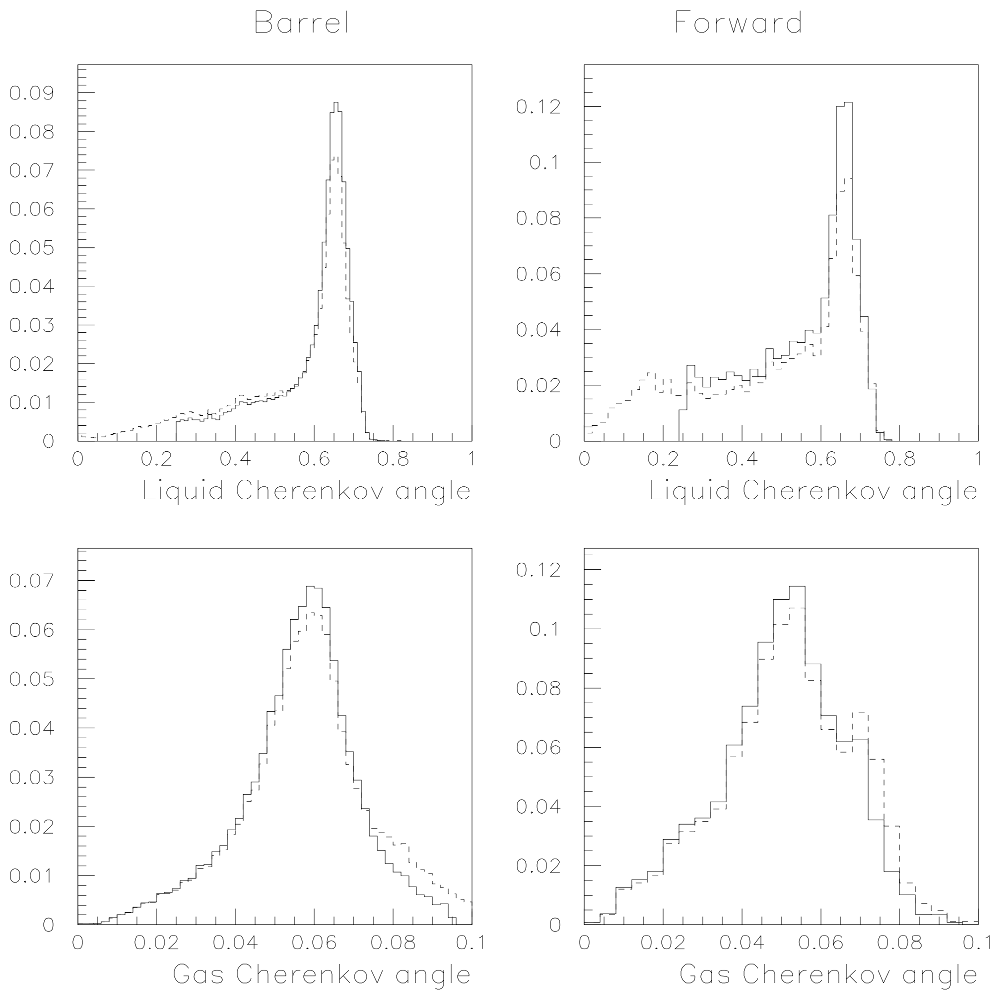

Figure 3.10: *Single photon distributions for simulated pions of momentum between 0.7-1.5 GeV/c (above 3 GeV/c for gas radiator) in the liquid (gas) radiator for the barrel (forward) RICH before (dashed line) and after (full histogram) applying weights*

found photoelectrons [4]. The search stops when no additional photoelectrons satisfying the above criterion can be found. With the remaining photons a new search is started for the same hypothesis. When no photons are left the next hypothesis is considered with the same photons. At the end we have £ve sets of rings, each set corresponding to one mass hypothesis. For each ring in a given set the following quantities are calculated :

- the weighted number of photoelectrons, $N_w = \sum_{i=1}^{N} w_i$ (N is the number of photons in this cluster);
- the average Cherenkov angle,

$$\theta_c^{mean} = \frac{\sum_{i=1}^{N} \frac{w_i \theta_i}{\sigma_{\theta_i}^2}}{\sum_{i=1}^{N} \frac{w_i}{\sigma_{\theta_i}^2}};$$

- the average expected error per photon,

$$\sigma_{photon}^{exp} = \frac{1}{\sqrt{\frac{1}{N}\sum_{i=1}^{N} \frac{w_i}{\sigma_{\theta_i}^2}}}.$$

From all the rings found the one with the largest number of weighted photons is £nally chosen and will be called the main ring of this track. Ambiguous photons have now to be resolved. If an ambiguous photon is only selected in this ring then the ambiguity is solved. A photon, however, may belong to two or more main rings associated with other tracks or the same track but different radiators. The ambiguity then can be either gas-gas, liquid-liquid or gas-liquid. The latter is resolved by comparing the conversion depth since liquid photons originate from the side of the photon detector that is closest to the liquid radiator, whereas gas photons originate from the opposite side. To solve gas-gas or liquid-liquid ambiguities the number of unambiguous photons in both rings and the χ^2 contribution of the ambiguous photon to each ring are used. After associating ambiguous photons to a ring, the parameters of the ring are recalculated. If no ring is found with more or equal than two photons, it is assumed that the track has no Cherenkov light in the medium considered. This observation is later used for the veto tag, i.e. when one looks for a mass hypothesis with no emitted Cherenkov photon.

The error per ring σ_{ring} is a function of the track momentum p, the average error per photon σ_{photon}^{exp}, and the observed number of photons N. Simulated π-data were used to parameterise the dependence of σ_{ring} on these parameters for hadronic events. The procedure to obtain this parameterisation is as follows. First, the σ_{ring} is supposed to be linearly dependent on σ_{photon}^{exp}, i.e. $\sigma_{ring} \propto \sigma_{photon}^{exp}$. To obtain the parameterisation on p and N we determine the pull distribution, where the *pull* is de£ned as :

$$\frac{\theta_c^{mean} - \theta_\pi^{exp}}{\sigma_{ring}}, \tag{3.12}$$

[4] The window of 2.5 σ_{θ_i} is used for the ring £nding in the gas radiator, whereas that of 3.5 σ_{θ_i} is used in the liquid radiator.

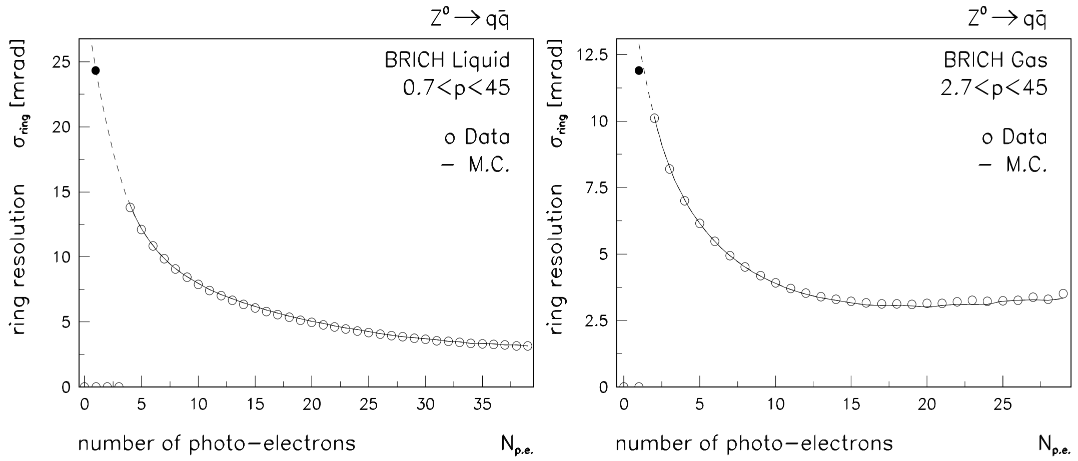

Figure 3.11: *The RIBMEAN data and Monte Carlo distributions for the number of photoelectrons versus the ring resolution. The black points indicate the mean value of the distributions for the single photoelectron resolutions. The dashed lines represent the extrapolation of the Monte Carlo.*

From this distribution one extracts the functional dependence on N and p. The r.m.s. of the pull distribution should be 1 for pions, since θ_π^{exp} is the expected angle for the π hypothesis. Starting from the assumption $\sigma_{ring} = \sigma_{photon}^{exp}/\sqrt{N}$ the p-dependence is extracted. The same is done for the N-dependence. From this analysis we £nd that the errors per ring can be parametrised for the barrel (B) and forward (F) gas radiators as

$$\begin{aligned} \sigma_{ring}^{B} &= \sigma_{photon}^{exp}(1 + \frac{0.8}{2+p})\sqrt{1/N} \\ \sigma_{ring}^{F} &= \sigma_{photon}^{exp}0.85(1 + \frac{0.8}{2+p})\sqrt{1/N + 1/12} \end{aligned} \tag{3.13}$$

and for the liquid radiators as

$$\begin{aligned} \sigma_{ring}^{B} &= \sigma_{photon}^{exp}0.56(1 + \frac{1.4}{p})\sqrt{1/N + 1/6} \\ \sigma_{ring}^{F} &= \sigma_{photon}^{exp}0.80(1 + \frac{1.4}{p})\sqrt{1/N + 1/9} \end{aligned} \tag{3.14}$$

The barrel RICH gas radiator error has the expected $1/\sqrt{N}$ term and a weak momentum dependence, whereas the liquid radiator error has a stronger dependence on p because the track errors are—by convention—not propagated into σ_{photon}^{exp}. The deviation from the $1/\sqrt{N}$ behaviour at high values of the observed number of photons is probably a consequence of the correlation of the errors due to uncertainties in the position of the track. The same is true for the forward RICH errors.

Performance of the method

An important advantage of the RIBMEAN algorithm is that its performance can be simulated rather well by Monte Carlo. This is because of its simple treatment of the available information. We will comment on it later in this section. Figure 3.11 shows that the parametrisations of the ring resolution as given by (3.13) and (3.14) correctly reproduce the N-dependence of the ring resolution. Figure 3.12 shows the Cherenkov angle distribution as obtained by RIBMEAN for the liquid and gas radiators as a function of the momentum of the particle. The three bands correspond to pions (uppermost), kaons (middle) and protons (lowest). In the next chapter we will compare real data and data from a Monte Carlo simulation relevant to the analysis presented in this thesis. A detailed comparison can be found in references [24],[25].

Some comments can be given about the features of the algorithm. In the £rst place, the weighting of photons enables us to use all the signal photons, though with different weights, and to reduce the effect of background photons. This is important for the analysis of the pion background in the tagged kaon sample presented in section 5.3. Secondly, since starting points are chosen corresponding to the £ve mass hypotheses, the best resolution per ring is obtained. Finally, the choice of the ring with the largest number of weighted photons as the £nal ring gives a small bias in favour of high Cherenkov angles because of the presence of background, see Figure 3.7.

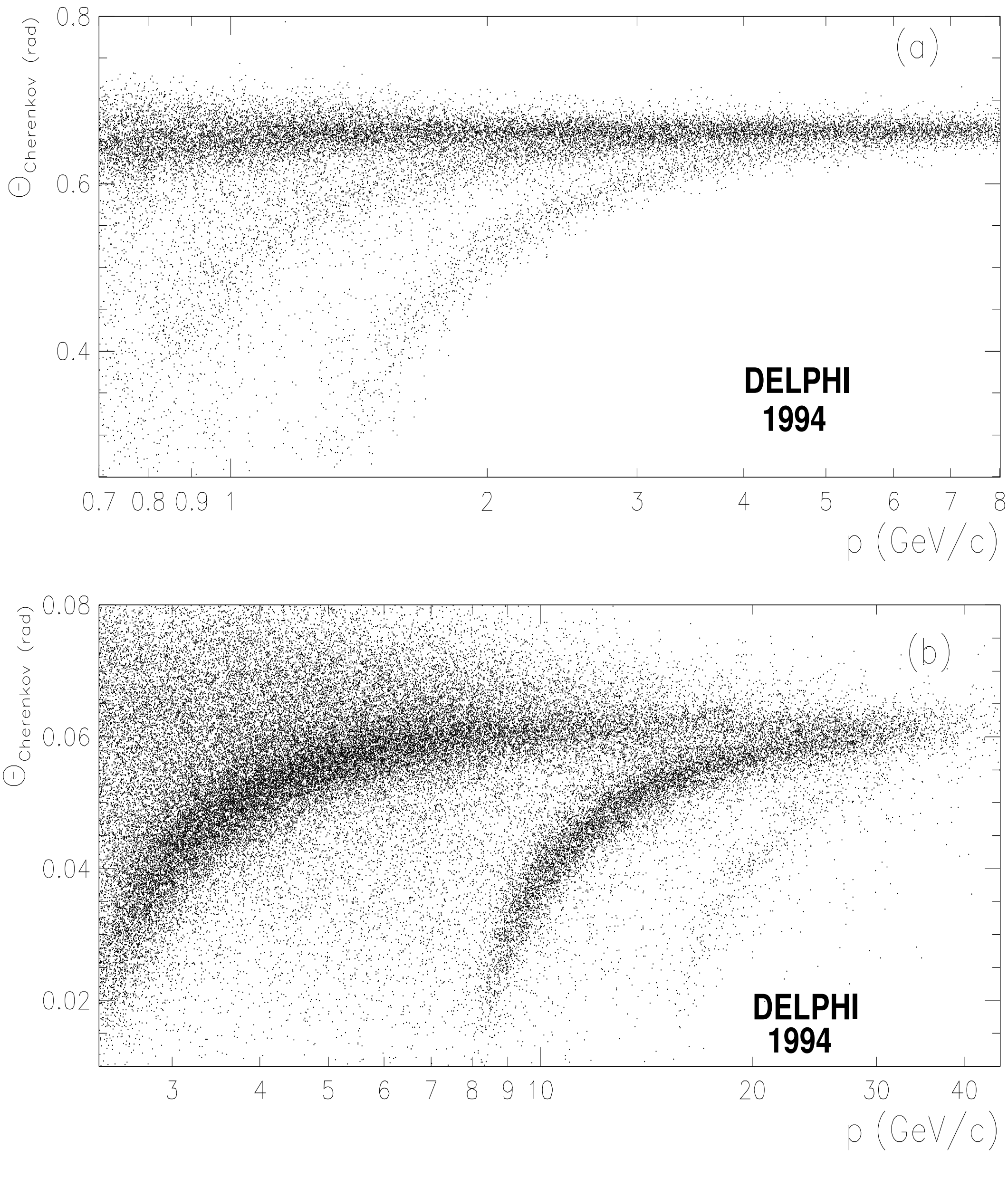

Figure 3.12: *RIBMEAN results for the average Cherenkov angle versus particle momentum for barrel RICH liquid (a) and gas (b) radiator data taken in 1994.*

Chapter 4

Event selection and high-energy kaon identi£cation

In this chapter we describe the sample of events used in the analysis. As explained in Chapter 1, we are interested in $s\overline{s}$-quark pairs from Z^0 decay. The $s(\overline{s})$ like all other quarks cannot be observed as free particles because they hadronize and appear bounded inside hadrons as jets of particles.

First, we have to select the hadronic Z^0 decays, then enrich this sample in s-quark decays. This is done by selecting events with identi£ed charged kaons with high momenta. Because high-energy kaons can also be produced in decays of b and c hadrons we will reject b-quark and, partially, c-quark decays. This is done by using information from the vertex detector (VD).

4.1 Hadronic event selection

Tracks from stable charged[1] hadrons and leptons are accepted if :

- their polar angle θ is between 20° and 160°. This interval is mainly determined by the tracking system acceptance, see Figure 4.1;
- the track length in the TPC, the main tracking device, is longer than 30 cm;
- the impact parameter[2] with respect to the interaction point is less than 4 cm in the $R\phi$ plane and less than 10 cm in $|z|$. This rejects tracks produced in beam-gas interactions and particles originating from an interaction with the detector material;

[1] We call a charged particle stable when it has $c\tau$ of a few centimetres, where c and τ are the speed of light in vacuum and the life-time of the particle, respectively. Most of these particles are produced with relativistic velocities and are able to reach the sensitive part of the detector.

[2] The track impact parameter is de£ned as the distance of the track to a reference point at the point of its closest approach. The reference point is the reconstructed primary vertex, i.e. the point where the electron and positron annihilate.

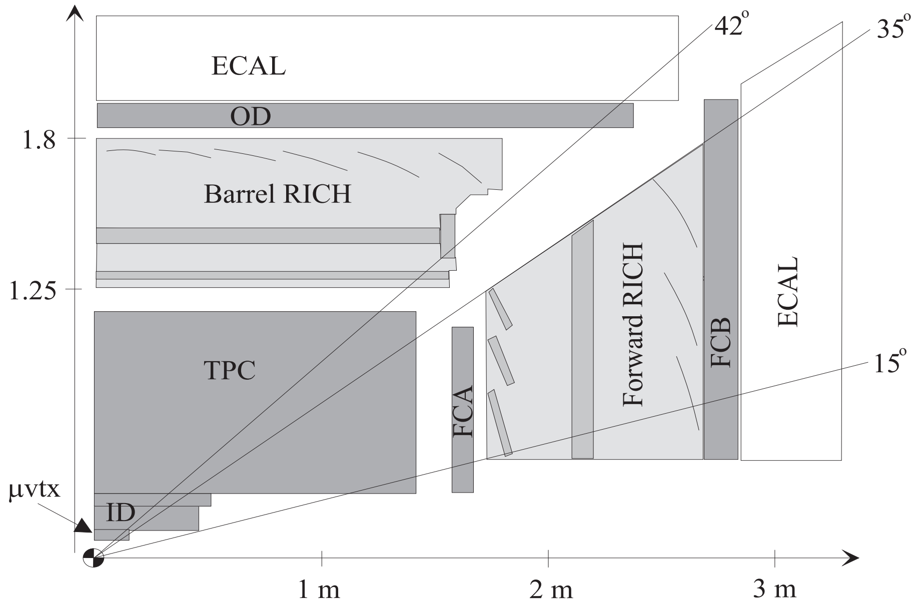

Figure 4.1: *Schematic view of the DELPHI RICH and tracking detectors.*

- the momentum p is greater than 0.4 GeV/c with an error $\Delta p/p \leq 1$.

The *thrust* quantity is de£ned as

$$T = \max_{\|\vec{n}\|=1} \frac{\sum_i |\vec{n} \cdot \vec{p}_i|}{\sum_i \|\vec{p}_i\|}$$

where $\vec{p}_i$ is the momentum of i-th particle of the event and the *thrust axis* is the direction of the vector $\vec{n}$. For the calculation of the *thrust axis* of the event neutral showers in the calorimeters not associated with charged tracks are used if the reconstructed energy has an error $\Delta E/E \leq 1$. The total longitudinal momentum takes its maximum value along this direction. The axis is associated with the direction of the s and $\bar{s}$ quark pair. An event is selected as a hadronic event if :

- the number of selected charged particles is greater than 4;

- the total energy of the charged particles, assuming all particles to be pions, is larger than 15 GeV for the whole event and larger than 3 GeV in each event hemisphere as de£ned by the thrust axis.

The £rst requirement rejects leptonic decays of the Z^0 and cosmic muons. When the Z^0 decays to $\mu^+\mu^-$ or $\mathrm{e}^+\mathrm{e}^-$ pairs the event has two charged tracks, whereas the decay into $\tau^+\tau^-$ can result in 4 charged tracks in the £nal state. This cut rejects 97% of the τ-events. The second requirement rejects beam-gas and two-photon events. These events have a strong boost along the beam axis and have a relatively low energy deposition inside the detector.

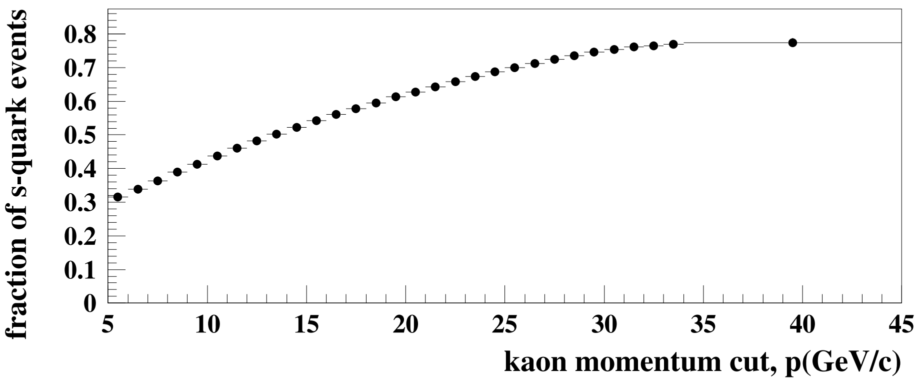

Figure 4.2: *The s-quark purity for hadronic Z^0 decays in which the highest momentum kaon has a momentum larger than the value plotted on the horizontal axis. The plot is based on a sample of 2 million Monte Carlo hadronic events.*

A total of 3.2 M hadronic events has been selected with the above cuts. The residual contamination from $Z^0 \to \tau^+\tau^-$ and $\gamma\gamma$ events is below 0.3%, and from beam-gas interactions it is below 0.1%.

To compare theory with experiment, data are simulated according to the theory, folding in the detector response. Hadronic events are generated with the JETSET 7.3 Monte Carlo program [9] with parameters tuned by the DELPHI Collaboration [14]. This Monte Carlo program uses different functions to describe the fragmentation of light (u, d, s) and heavy (c, b) quarks (see section 1.5). The Lund symmetric fragmentation function (1.28) describes the light quark hadronisation process, while the Peterson function (1.29) is used for the fragmentation of bottom and charm quarks. The detector response is simulated with the DELPHI program DELSIM [26]. The simulated data have the same format as the real data, and will be analysed by the same analysis programs. A sample of 10.7 M simulated hadronic events is used. These Monte Carlo events are also used to evaluate detector-related characteristics of the analysis, e.g. acceptances, ef£ciencies and so on.

4.2 s quark tagging

Hadronic events for which the thrust axis has a polar angle in the range $|\cos\theta_{thrust}| \leq 0.7$ are considered for the barrel analysis. For the forward analysis, the thrust axis has to be in the angular range $0.8 \leq |\cos\theta_{thrust}| \leq 0.95$. These requirements are necessary to keep the whole event inside the active part of the tracking system of the detector and to be able to identify the high energy kaons with the BRICH and FRICH, see Figure 4.1.

The production of a high momentum strange hadron is a likely signature for a primary

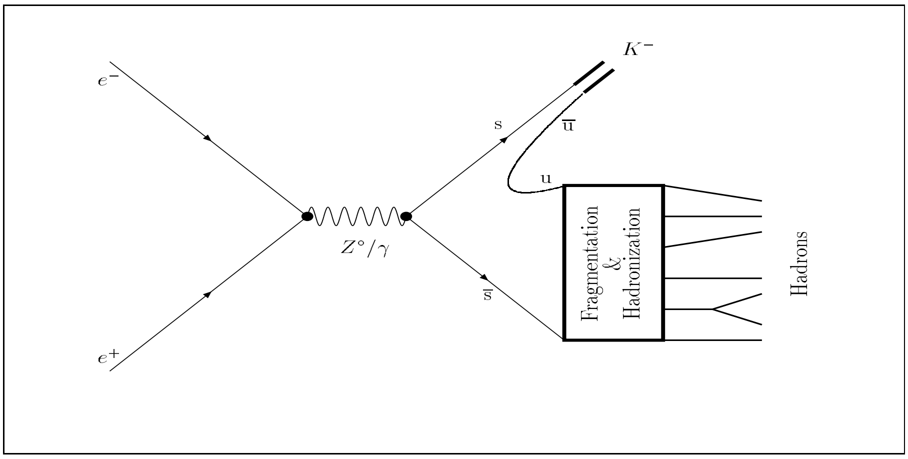

Figure 4.3: K *production as a leading particle.*

s quark. Figure 4.2 shows the s-quark purity as a function of the momentum of the most energetic charged kaon in an event. The purity does not reach 100% because the kaons can be the result of the decay of b, c quarks. A kaon can also be produced in the fragmentation of u, d quarks. One can see that the purity increases for increasing momenta. The electric charge of the kaon carries information on the charge of the initial primary quark and thus allows the s quark to be separated from the $\overline{s}$. This is illustrated in Figure 4.3. Monte Carlo events con£rm that the ¤avour of a leading hadron can be associated with the ¤avour of the primary quark. The leading particle is the one with the highest momentum. In our analysis we will use high-energy charged kaons. These kaons can be identi£ed with the DELPHI RICH detectors.

The particles to be identi£ed as kaons are required to lie inside the RICH acceptance and should have momenta between 10 GeV/c and 24 GeV/c. The lower momentum limit is determined by the Cherenkov threshold ($p \sim 8.5$ GeV/c) of the gas radiators of both RICHs. The upper limit corresponds to a one-sigma separation between the Cherenkov angles of pions and kaons. If more than one kaon satis£es these constraints, the kaon with highest momentum is selected. The kaon is not necessarily the highest momentum particle in the event. The ¤avour may be tagged, for instance, by a kaon which is the decay product of a $\mathrm{K}^*(892)$. When decaying into $\mathrm{K}^\pm\pi^\mp$ the $\mathrm{K}^*(892)$ can produce a kaon, which, although it correctly tags the primary quark, has a momentum lower than that of the pion.

The quark direction is estimated using the thrust axis, which is later oriented parallel (anti-parallel) to the $\mathrm{K}^-(\mathrm{K}^+)$ projection along this axis, see Figure 4.4. Later in this chapter real and Monte Carlo data are compared for leading particles.

High-energy kaon identi£cation

Charged K mesons are identi£ed by determining the average Cherenkov angle for a reconstructed ring and comparing it with the angle predicted for a K-meson. The clustering

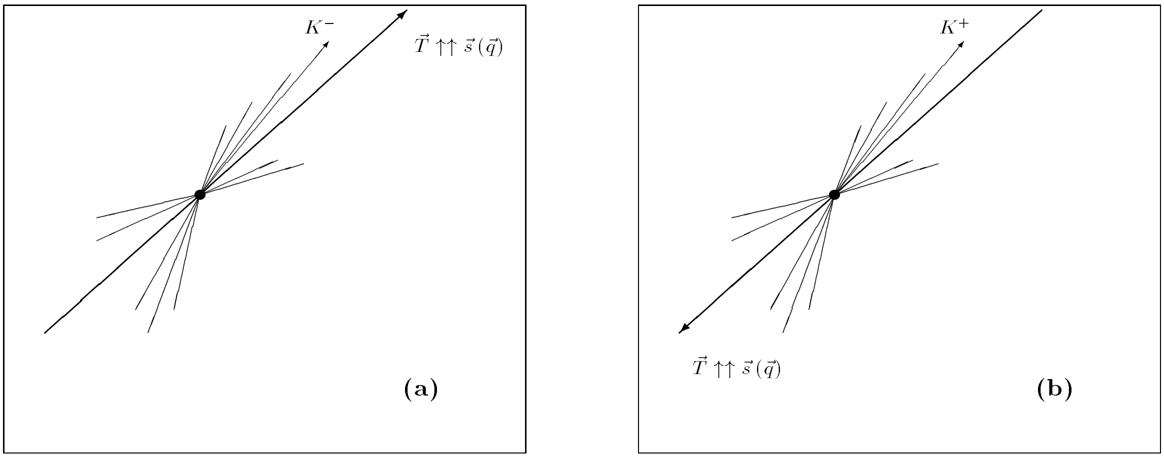

Figure 4.4: *The direction of the quark is de£ned by the trust axis, which is later oriented parallel (anti-parallel) to the* K^- *(*K^+*) projection along this axis.*

algorithm described in Chapter 3 estimates the Cherenkov angle θ_c, the expected error σ_{θ_c} and the number of photons in the ring. Using this information kaons are identi£ed on a track-by-track basis. The reconstructed average Cherenkov angle in the gaseous radiators of the BRICH and the FRICH respectively as a function of the particle momentum is shown in Figure 4.5. The expected angles are different because of the different gases used in the barrel and forward RICHs.

Charged particles are considered when they pass the track selection criteria, have a momentum between 10 and 24 GeV/c, and lie within the RICH acceptance. The latter implies that tracks have polar angles in the range $0.04 < \cos\theta < 0.68$ in the barrel region and $0.82 < |\cos\theta| < 0.94$ in the forward one. Only data from those data-taking runs are used where the gas RICH was fully operational.

Furthermore, a kaon candidate has to satisfy the following criteria:

- the OD or FCB has to be used in the track £t. This ensures that the particle that crosses the RICH is well reconstructed, see Figure 4.1 ;

- at least 2 photoelectrons have to be found in the ring to measure the mean Cherenkov angle ;

- the measured and the expected Cherenkov angles have to satisfy the following conditions in order for a particle to be identi£ed as kaon [27] :

$$\frac{|\theta_c - \theta_c^K|}{\sigma_{\theta_c}} < 2.5 \quad (4.1)$$

$$\frac{|\theta_c - \theta_c^\pi|}{\sigma_{\theta_c}} > 2 \quad (4.2)$$

where θ_c^K, θ_c^π are the expected angles for the K and π hypothesis for a given momentum. The espected error on the Cherenkov angle σ_{θ_c} is σ_{ring} de£ned in (3.13).

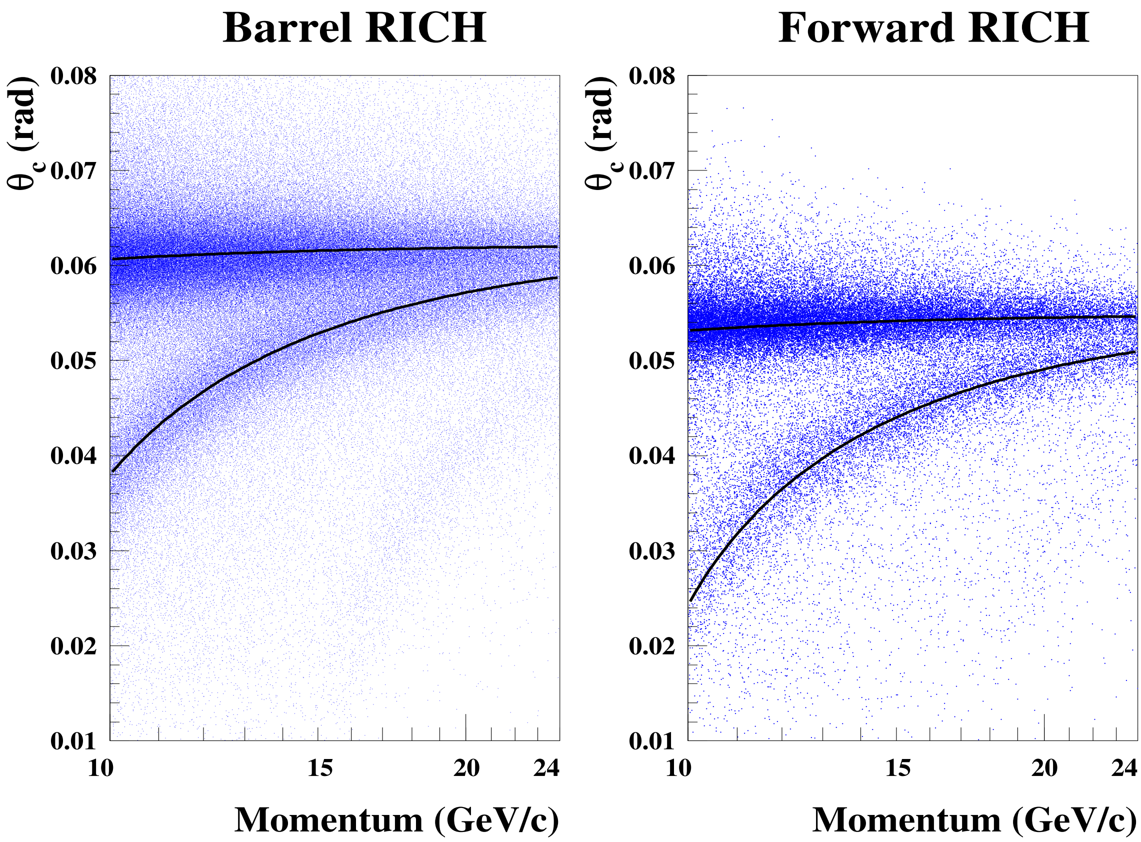

Figure 4.5: *For the 1994 data the reconstructed average Cherenkov angle in the gaseous radiator of the BRICH (left) and the FRICH (right) as a function of the particle momentum (10 GeV/c $< p <$ 24 GeV/c). The two solid lines show the expected Cherenkov angle for pions and kaons.*

In the forward region, an additional cut on the polar angle of the particle is applied when rings happen to lie in a dead zone of the drift volume of the photon detectors. Each half of the FRICH is divided into 6 azimuthal sectors, while each sector has one drift volume which is electrically divided in two. The electric £elds in these halves cause photoelectrons to move towards oppositely positioned MWPCs, see Figure 3.6. Because of the DELPHI magnetic £eld drifting electrons experience a Lorentz force. As a result, the electrons drift under a Lorentz angle of $50°$. This creates two dead zones in the drift volume: in the upper part of one half of the volume (odd-chamber) and in the lower part of the second half (even-chamber). The dead zone in the lower parts of even-chambers does not affect the analysis because the row of FRICH mirrors closest to the beam pipe is not used. In the so-called odd-numbered chambers, the full Cherenkov ring can not be reconstructed for tracks with a polar angle in the region $0.82 < |\cos\theta| < 0.87$. In this region the acceptance is different for positively and negatively charged particles. This is due to the fact that the trajectories of positively and negatively charged particles turn in opposite directions. The Cherenkov light produced along these curved trajectories ($\sim$ 60 cm) in the gas radiator is projected by the spherical mirrors onto slightly different locations in the photon detector for oppositely charged particles. For negatively charged particles the ring lies more inside the dead zone than for positively charged ones. This effect is purely geometrical and well reproduced by the simulation. In the analysis, events are rejected when a tagged kaon touches an odd-chamber and has a polar angle in the region $0.82 < |\cos\theta| < 0.87$. About 20% of the particles are lost with this cut in the forward analysis[3].

According to the simulation the average identi£cation ef£ciency for selected $\mathrm{K}^{\pm}$ is 53% in the Barrel region and 42% in the Forward region. Figures 4.6 and 4.7 demonstrate that the performance of the particle identi£cation algorithm in the gas radiators of the Barrel and Forward RICH is fairly well reproduced by the simulation. The discrepancies are corrected for in the analysis.

[3]Because the effect is purely geometrical and can be accounted for in the simulation, exclusion of the dead zones does not affect the forward-backward asymmetry of the kaons (see the next chapter). It increases, however, the statistical error.

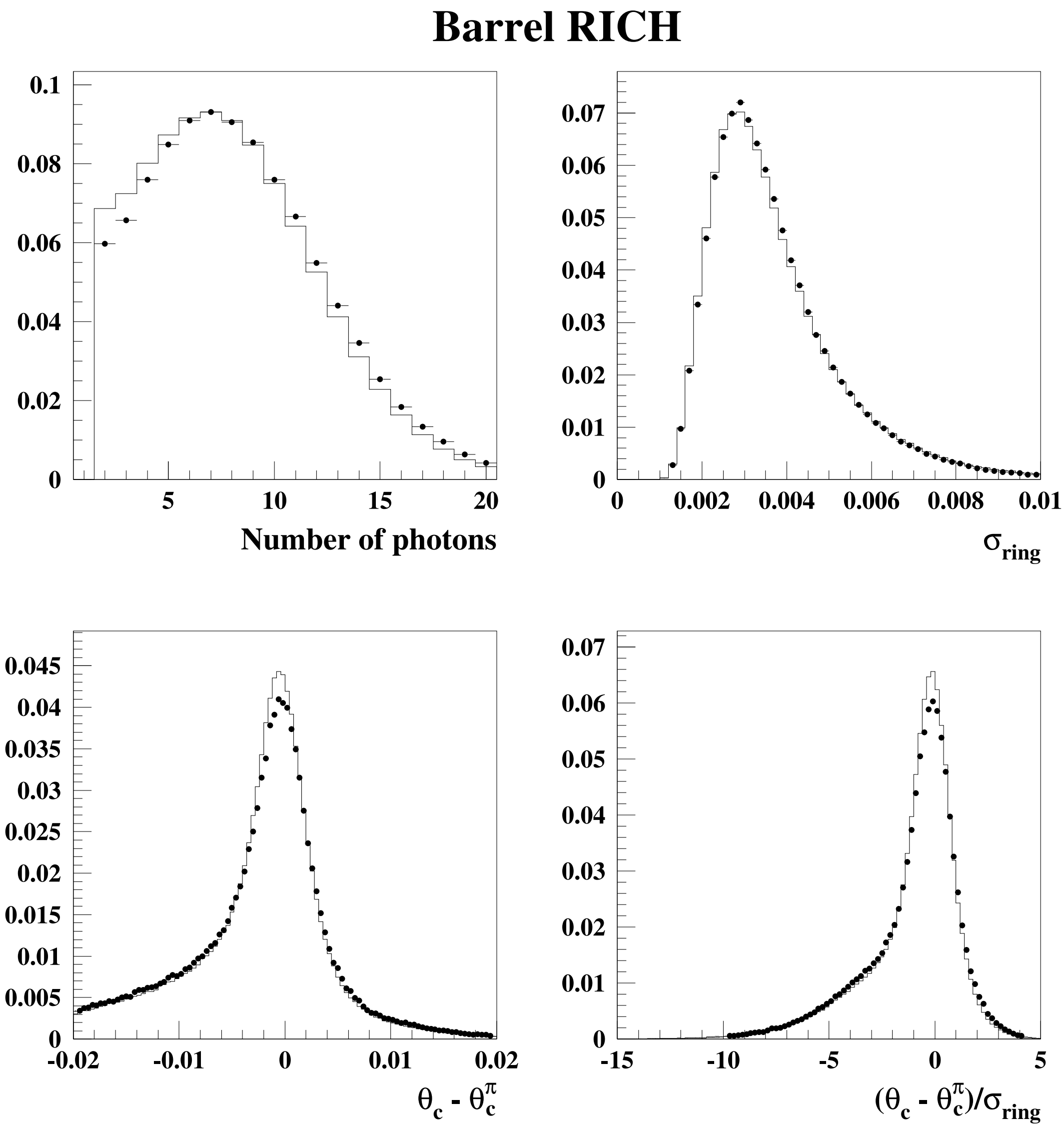

Figure 4.6: *Normalised distributions of the Cherenkov ring parameters for charged particles (with momentum between 10 GeV/c and 24 GeV/c) in the gas radiator of the Barrel RICH for 1994 data (dots) and simulated data (histograms) for the observed number of photons, the expected error per ring, the difference between the measured Cherenkov angle and the expected one in the pion hypothesis, and the pull for the pion hypothesis.*

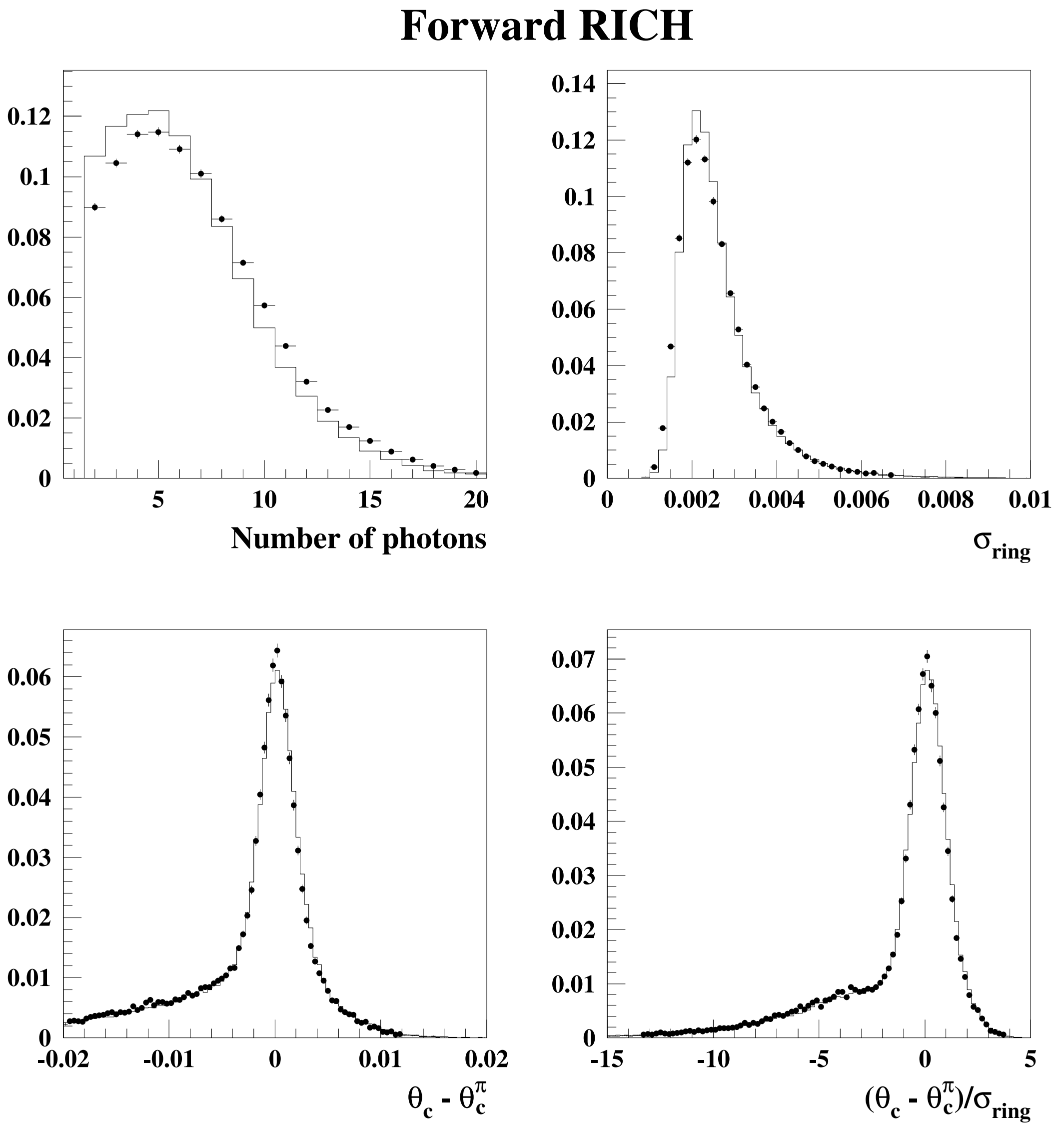

Figure 4.7: *Same as Figure 4.6 for the Forward RICH.*

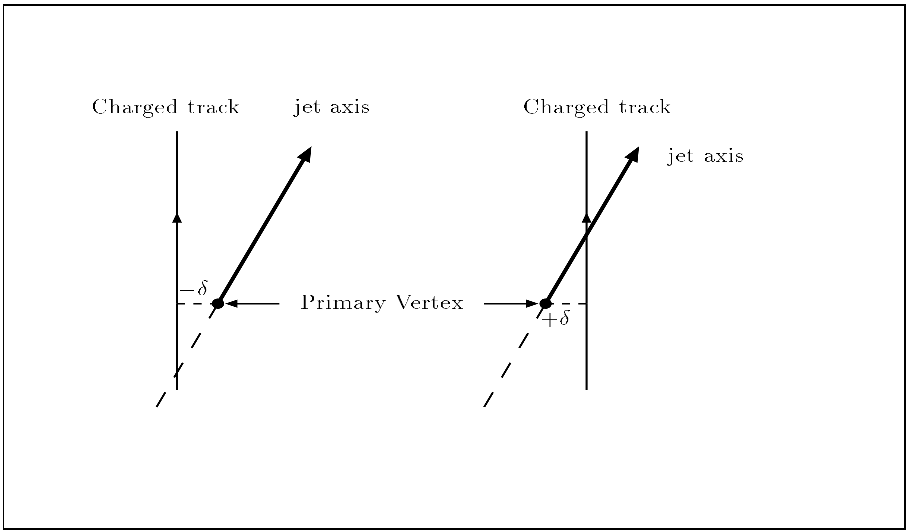

Figure 4.8: *De£nition of the sign of the impact parameter* δ.

4.3 Rejection of heavy quarks

With the identi£cation of high momentum $\mathrm{K}^{\pm}$ as described in the previous section an event sample is selected for which the fraction of events with a primary s quark (s-events) is determined from the simulation to be 43%. To improve this fraction b-tagging information is used for the barrel region ($|\cos\theta_{thrust}| \leq 0.7$) to reject kaons from bottom and charm quark decays.

The b-tagging algorithm is based on the precise measurement of the impact parameter of tracks using the micro-vertex detector [28]. The impact parameter is de£ned as the minimum distance between the charged particle trajectory and the reconstructed primary vertex. It is positive if the intersection of the track with its jet [4] axis is in front of the primary vertex, see Figure 4.8. The ratio of the impact parameter and its error is called signi£cance (S). Hadrons containing a heavy quark (b, c) decay weakly. They have relatively long lifetimes and, because of their large mass, large transverse momenta of the decay products. Their decay products, therefore, will have relatively large impact parameters with respect to the primary vertex. Figure 4.9 illustrates the fact that for the relatively low mass c-hadrons (~ 1.8 GeV/c^2) the impact parameters are smaller than for the high mass b-hadrons (~ 5 GeV/c^2). It, therefore, is more dif£cult to identify (and remove from the analysis) c-events than b-events.

Negative values of the signi£cance are a consequence of detector resolution effects. This part of the S-distribution is therefore used to compute from the real data, a probability density

[4] A jet represents a group of tracks that represents a certain ¤ow of event momentum. Different algorithms can be used to group particles together. They use variables that are related to the (virtual) mass of the object that could decay into these particles. A jet can be b-, c-hadron or high-energy parton (gluon or quark), see Figure 4.9.

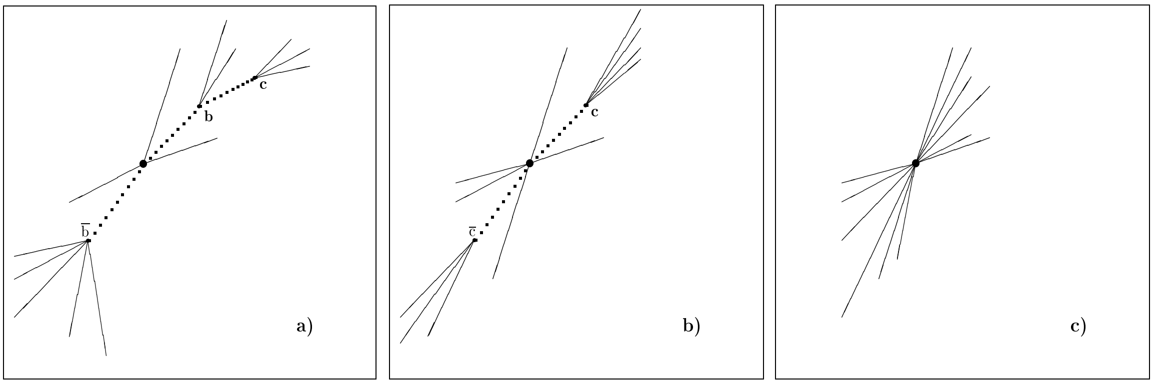

Figure 4.9: *Different topologies of heavy and light quark events: a) b-event, b) c-event, and c) u-,d-,s-event*

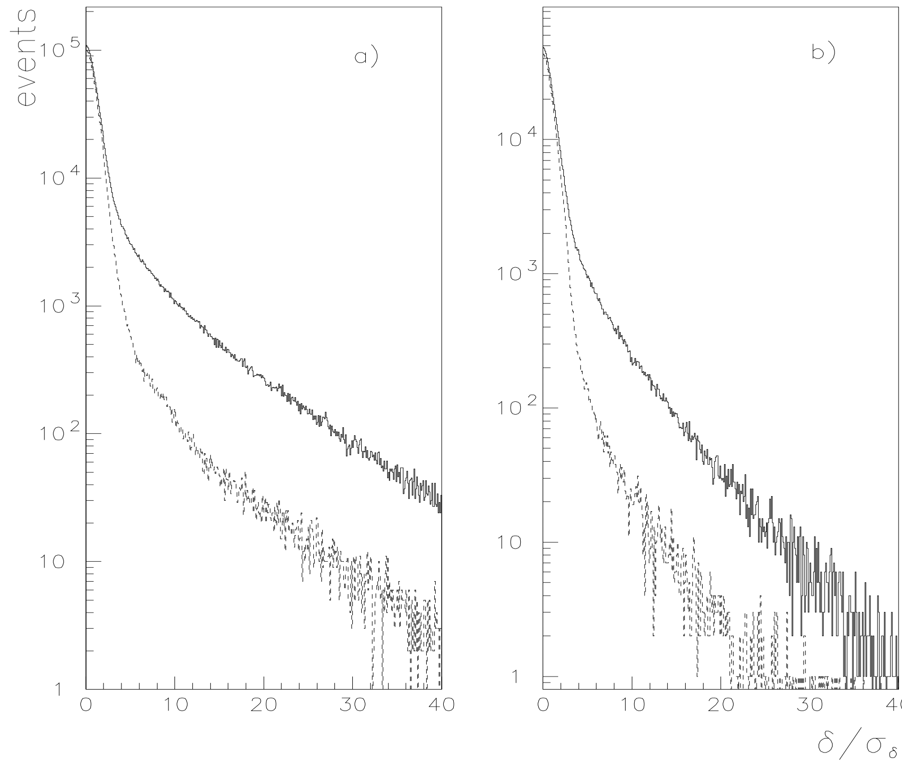

Figure 4.10: *Distribution of the absolute value of the signi£cance in $R\phi$ (a) and Rz (b) for tracks from real data measured in the Vertex Detector with negative (dashed line) and positive (solid line) impact parameter*

distribution of S for tracks coming from the primary vertex. Figure 4.10 shows the negative and positive part of the signi£cance distribution. The distribution corresponding to negative values of the signi£cance falls well below that of the positive one for high absolute values. This is what we expect for secondary vertices.

The distribution of tracks with negative impact parameter is used to determine the resolution function $f(S)$, which is the probability density function of the signi£cance for tracks originating in the primary vertex. In particular a sample of events is used, where the contribution of B hadrons is suppressed. Using $f(S)$ the probability that a single track with an absolute value of the signi£cance larger than S_i comes from the primary vertex is

$$P(S_i) = \int_{|S|>|S_i|} f(S)\mathrm{d}S$$

When the tracks from the primary vertex have non-correlated impact parameters one can write the probability for N selected tracks to come from the primary vertex in the form:

$$P_N \equiv \Pi \cdot \prod_{j=0}^{N-1} \frac{(-\ln \Pi)^j}{j!}, \quad \text{where} \quad \Pi \equiv \prod_{i=1}^{N} P(S_i). \tag{4.3}$$

This probability has a ¤at distribution for tracks coming from the primary vertex, while it is peaked at small values for tracks coming from secondary decay vertices.

The discriminant variable that will be used to reject events containing heavy quarks is the probability P_N^+. It is computed according to (4.3) on an event-by-event basis for all tracks which have hits in the VD and have a positive signi£cance. All events with $P_N^+ > 0.15$ are accepted. This value is a compromise between rejecting as much as possible the charm contamination and keeping the s tagging ef£ciency above 80%. As a result of this cut, the fraction of s-events in the data sample increases from 43% to 55%, whereas the fractions of b-(c-) events decreases from 13.6% (23.3%) to 0.9% (16.0%). These numbers are obtained from Monte Carlo data and are for real kaons identi£ed with the RICH and with momenta between 10 GeV/c and 24 GeV/c. Figure 4.11 shows the P_N^+ distributions for bottom, charm and light quark MC events with a high energy $\mathrm{K}^{\pm}$ selected as described in sections 4.1 and 4.2. The peak at zero probability for light quark events is due to the presence of particles from secondary interactions in the detector material or from the decays of long-lived particles (mainly K_s^0 and $\Lambda(1116)$).

By removing most of the bottom and charm quarks, the s-quark asymmetry measurement becomes less sensitive to systematic uncertainties in the production of kaons from heavy quarks. In the forward region this heavy quark rejection cannot be applied because the FRICH has little overlap with the acceptance of the micro-vertex detector.

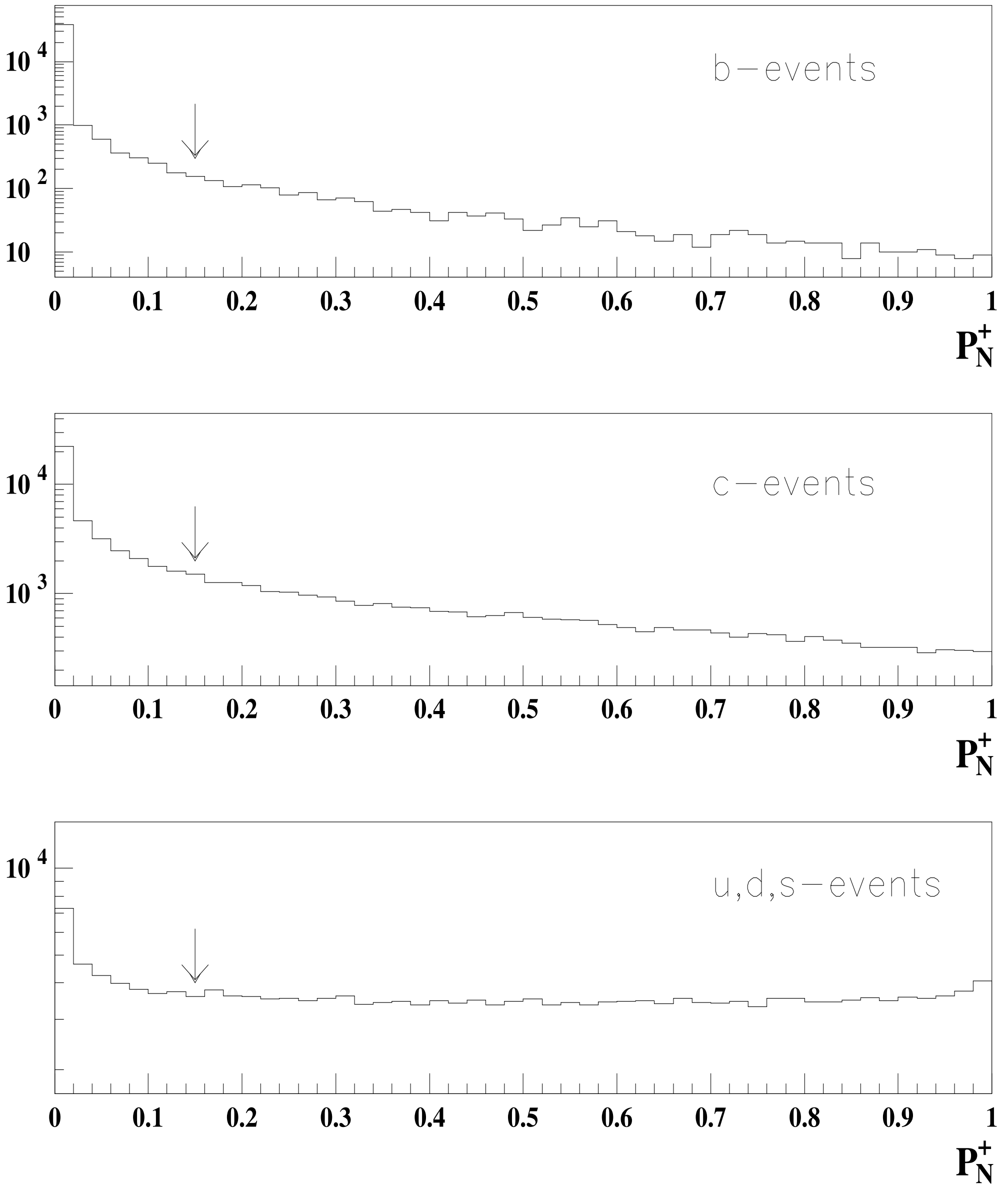

Figure 4.11: *Event probability P_N^+ for bottom-quark, charm-quark and up-down-strange-quarks events. The arrows show the applied cut.*

4.4 Studying the leading pions and kaons

Real and Monte Carlo data are compared to study the properties of leading pions and kaons. The sample of events is obtained after removal of heavy quark events as described in section 4.3.

The momentum spectrum of the highest momentum kaon in a given hemisphere, i.e. leading kaon is well reproduced by the simulation (Figure 4.12). The average purity of the kaons is 80%. Pions are mainly responsible for the other 20%. In a similar way we compare the momentum spectra of identi£ed pions in real and Monte Carlo data. The leading pion is the one with the highest momentum among all identi£ed pions in a given hemisphere. The result is shown in Figure 4.12b and indicates again a good agreement between real and Monte Carlo data. The average purity of the pions is 96%. Figures 4.12c and Figures 4.12d show that the angle between the leading kaon (pion) and the thrust axis is also well reproduced by the simulation. This is important because we use this axis as an approximation for the direction of the primary quark.

In reference [27] the K/π ratio is measured for b-quark and light-quark (u, d, s) events over the full momentum spectrum. The fractions of kaons and of pions itself and the momentum dependence of these fractions are well reproduced by the event generator (JETSET) that was used in the simulation. In the analysis we will look in more detail at, in particular, the leading particles of events tagged by a high-energy kaon. For that the leading particle is required to be in the opposite hemisphere to that of the kaon. Figure 4.13a shows that the probability as well as the momentum spectrum of the leading charged particle are fairly well reproduced by the simulated events. Figure 4.13b and 4.13c show respectively the kaon and pion spectrum.

In order to check that indeed the charge of the high-energy meson carries information about the charge of the primary quark, double-tagged events are selected. These events should either have two high-momentum [5] kaons or two high-momentum pions in opposite hemispheres. Two samples of 2431 double-tagged kaon and 13817 double-tagged pion events are selected. The probability that the mesons have opposite electric charges is compared for real and Monte Carlo data. The probability for the kaon and pion tags in the real data are 0.645 ± 0.021 and 0.539 ± 0.008 respectively. This agrees well with the Monte Carlo values of 0.686 ± 0.012 and 0.535 ± 0.004 [6]. The leading pion carries almost no information about the charge of the primary quark. For kaons we see a strong indication that the charged kaon can separate the s quark from $\overline{s}$.

[5] all through this section high energy means that the particle has a momentum in the range 10 GeV/c $<$ p $<$ 24 GeV/c

[6] The Monte Carlo value of 0.686 ± 0.012 for the probability for the kaon tag must be corrected for the fact that the kaon purity is lower in the real data than in the simulated data, see section 5.3. Accounting for this effect lowers the Monte Carlo value to 0.667 ± 0.012.

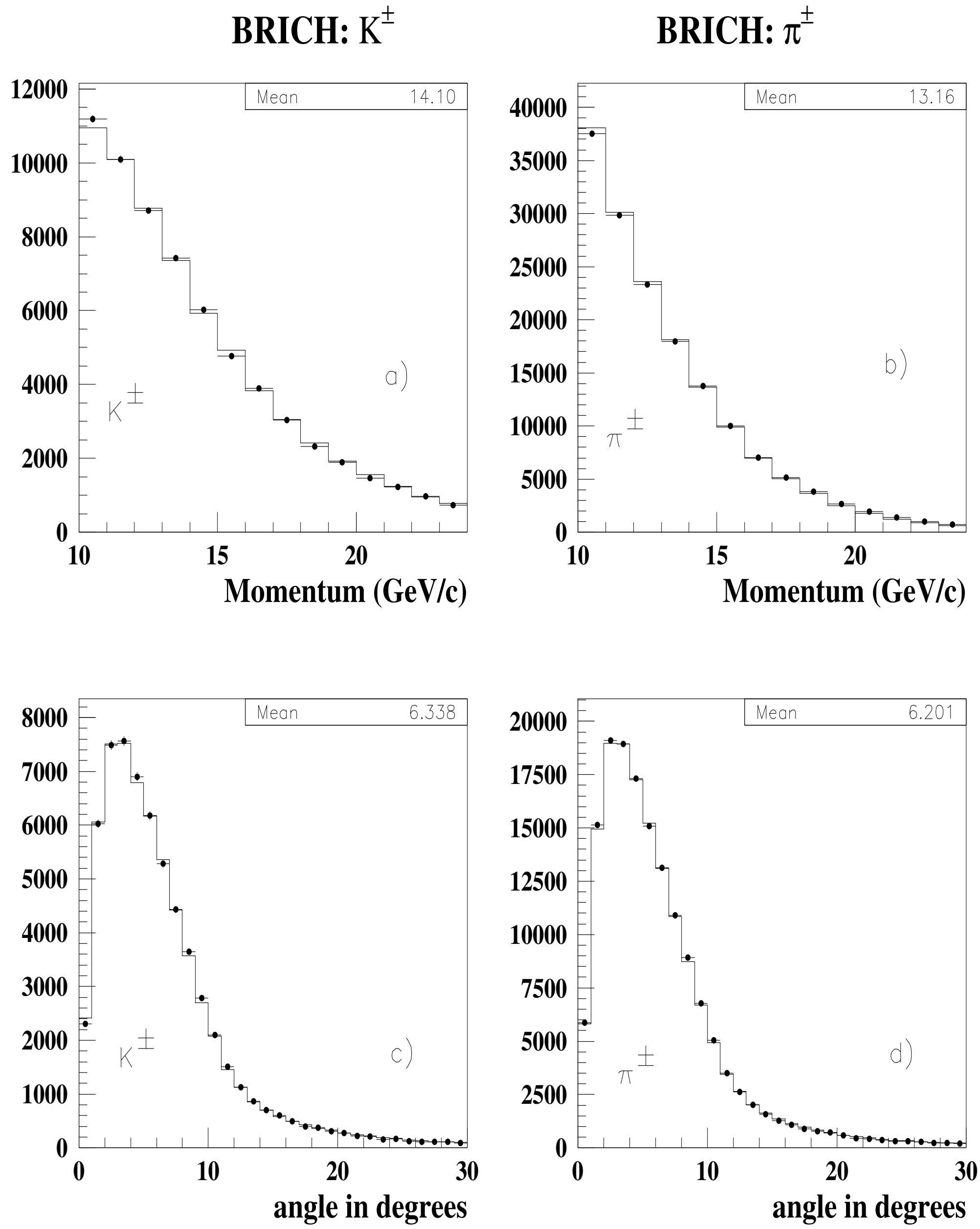

Figure 4.12: *Comparison for the momentum of the leading particle and the angle between the particle and the thrust axis for kaon (a,c) and pion (b,d) in real (dots) and Monte Carlo (histograms) data.*

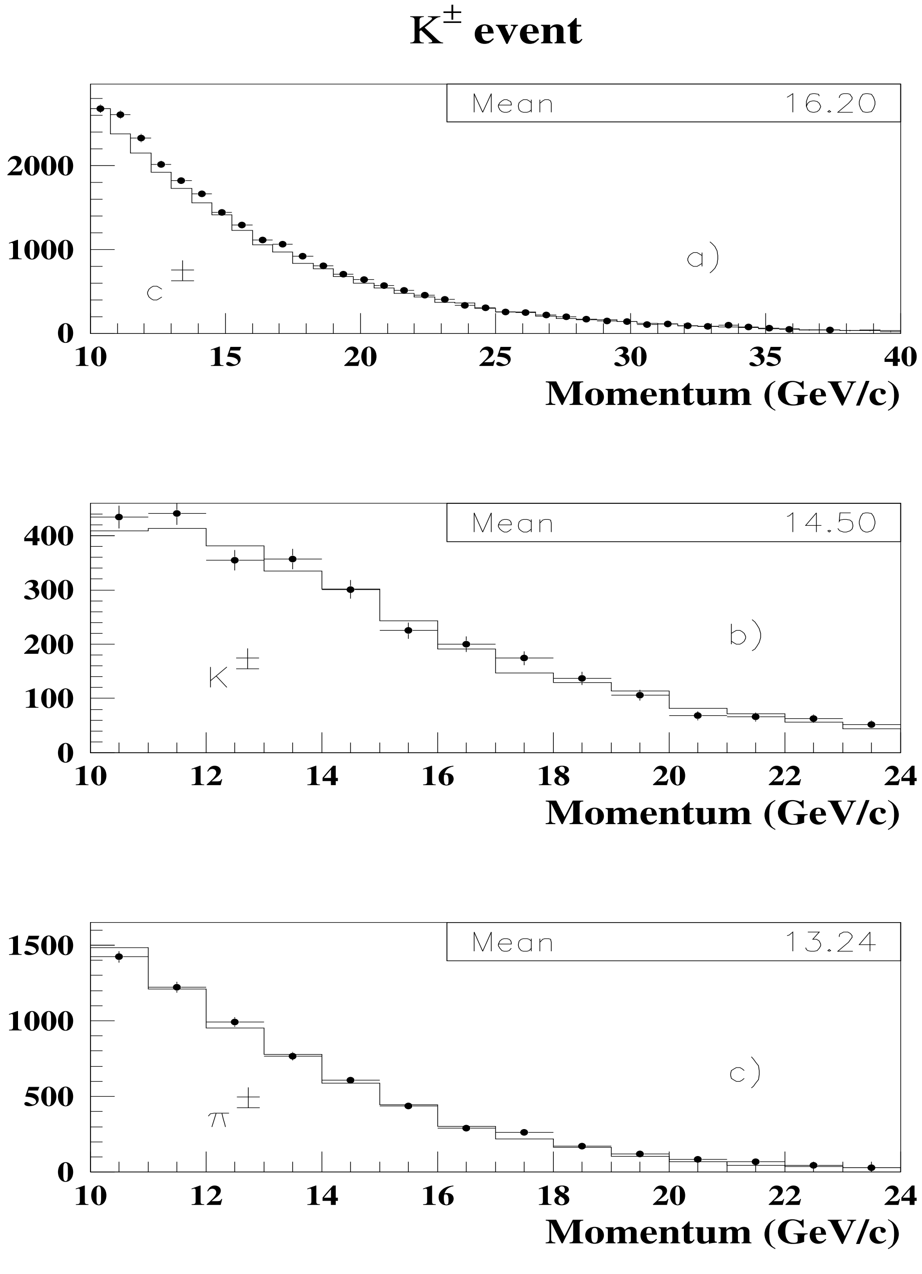

Figure 4.13: *The momentum spectra of leading particles in* K*-events: a) leading charged particle, b) leading particle identi£ed as kaon, and c) leading particle identi£ed as pion. The data sample for simulated events is twice as large as that for real events (1994).*

Chapter 5

Charged kaon asymmetry

To determine the s quark forward-backward asymmetry A_{FB}^{s} one £rst has to measure the polar angular distribution of events with a negatively and positively charged kaon. The asymmetry A_{FB}^{K} derived from these events is referred to hereafter as the charged kaon asymmetry. It can be written as :

$$A_{FB}^{K} \;=\; \sum_{q} \alpha_q (2c_q - 1) A_{q\bar{q}} \qquad (q = d, u, s, c, b). \tag{5.1}$$

The coef£cient α_q is the fraction of selected events with primary quark q, while the coef£cient c_q is the probability that the kaon charge corresponds to the charge of the primary quark q. In particular, a $K^{-}(K^{+})$ in a given hemisphere tags a primary $s(\bar{s})$ quark. $A_{q\bar{q}}$ is the q quark forward-backward asymmetry. The α_q in the barrel region are different from those in the forward region because heavy quarks can only be rejected in the barrel region, see section 4.3. This implies that the kaon asymmetry A_{FB}^{K} has to be determined in these regions independently.

In this chapter the measurement of A_{FB}^{K} is discussed, while the details of the extraction of A_{FB}^{s} are described in the next chapter.

5.1 Experimental procedure

The measurement of A_{FB}^{K} assumes the following behaviour of the asymmetry as a function of the thrust polar angle θ :

$$\frac{N_{K^-} - N_{K^+}}{N_{K^-} + N_{K^+}}(\cos\theta) \equiv A^{K}(\cos\theta) \;=\; \frac{8}{3} A_{FB}^{K} \frac{\cos\theta}{1+\cos^2\theta} \tag{5.2}$$

The thrust axis is oriented parallel (anti-parallel) to the K^{-} (K^{+}) projection along the axis itself. It is assumed that the thrust axis represents the quark direction, which is a reasonable assumption given the fact that the difference between the quark and thrust polar angles is on average zero, independently of the quark polar angle. Another satis£ed condition is that the r.m.s. spread for the difference between these polar angles does not change with the polar angle in the barrel region, while its variation is negligible small in the forward region. The quark asymmetry is given by Formula 1.19.

Every selected event has one leading charged kaon (see section 4.2). For this sample of selected events the asymmetry:

$$A_i^K = \frac{N_{K^-} - N_{K^+}}{N_{K^-} + N_{K^+}} \quad (5.3)$$

between the number of events with K^- and K^+ falling in a given angular interval i is determined. The angular interval corresponds to kaon polar angles $\cos\theta_K$. Because positively and negatively charged kaons are compared per bin of $\cos\theta_K$, possible differences in the acceptance for the forward and backward hemispheres cancel.

The measured A_i^K values have £rst to be corrected to take into account the kaon purity of the sample (due to misidenti£ed pions) and the asymmetry resulting from the difference in the K^- and K^+ cross-sections for interactions with the detector material. Both corrections depend on the $\mathrm{K}^\pm$ polar angle. The $\cos\theta_K$ bins are chosen in such a way that the corrections needed vary only slightly over the width of the bin, so that an average correction factor can be used for all the events in a given bin. The natural choice for the bin is the angular range covered by a RICH mirror (see Figures 3.4, 3.5, 4.1).

We de£ne A_i^{obs} as the kaon asymmetry after applying the above corrections. With corrections A_i^{obs} takes the following form

$$A_i^{obs} = \frac{(1-r_i) + A_i^{corr}(1+r_i)}{(1+r_i) + A_i^{corr}(1-r_i)} \simeq A_i^{corr} + \frac{1}{2}(1-r_i) \quad (5.4)$$

$$\text{with} \quad A_i^{corr} = \frac{A_i^{\mathrm{K}} - (1-P_i)A_i^{bckg}}{P_i}, \quad (5.5)$$

P_i is the purity of the kaon sample for a given $\cos\theta_{\mathrm{K}}$ bin. A_i^{corr} is accordingly the kaon asymmetry corrected only for the kaon purity. A_i^{bckg} is the asymmetry for the misidenti£ed particles (not kaons) as kaons. We present the method and the results of the A_i^{bckg} determination later in this section. The effect of different cross-sections for K^- and K^+ interactions is represented by the second term in (5.4). We de£ne a ratio $r_i = \epsilon_{\mathrm{K}^-}/\epsilon_{\mathrm{K}^+}$ for a given $\cos\theta_{\mathrm{K}}$ bin, where ϵ_{K^-} (ϵ_{K^+}) is the probability for a $\mathrm{K}^-(\mathrm{K}^+)$ to reach the tracking detector positioned behind the RICHs—i.e., the OD in the barrel region or the FCB in the forward region—without interacting with the detector material. The asymmetry from interactions with the material A_i^{mat} then becomes $\frac{1}{2}(1-r_i)$, and is described in more detail in section 5.2.

The distribution of the A_i^{obs} is £tted to the function (5.2) to extract A_{FB}^K. A binned χ^2 £t is used to extract A_{FB}^K: we minimise the χ^2 function :

$$\chi^2 = \sum_{i=1}^{m} \left(\frac{w_i A_{FB}^K - A_i^{obs}}{\sigma_i} \right)^2, \quad (5.6)$$

where σ_i is the statistical error on the asymmetry A_i^{obs}, and i runs over the m bins in $\cos\theta_{\mathrm{K}}$, 12 for the Barrel region and 4 for the Forward region[1]. The weight w_i takes into account

[1] In the analysis the row of FRICH mirrors closest to the beam pipe is not used, see also section 4.2.

the fact that the A_i^{obs} is determined in a $\cos\theta_K$ bin, while A_{FB}^K is the forward-backward asymmetry of the charged kaon as a function of the thrust polar angle, see equation (5.2). For a given bin i with n_i events the weight w_i is calculated according to (5.2):

$$w_i = \frac{8}{3}\frac{1}{n_i}\sum_{j=1}^{n_i}\frac{\cos\theta_j}{1+\cos^2\theta_j}, \tag{5.7}$$

where θ_j is the thrust angle of the j-th event with a $\mathrm{K}^{\pm}$ polar angle falling in bin i. This weight w_i also takes into account the fact that the asymmetry has an angular dependence inside the bin.

After the weights w_i are determined, the asymmetry for misidenti£ed particles A_i^{bckg} is equal to

$$A_i^{bckg} = w_i A_{FB}^{bckg} \tag{5.8}$$

$$\text{with} \qquad A_{FB}^{bckg} = \sum_q \alpha_q^{bckg}(2c_q^{bckg}-1)A_{q\bar{q}} \qquad q = d,u,s,c,b, \tag{5.9}$$

where α_q^{bckg} is the fraction of $q\bar{q}$ events with a particle misidenti£ed as K, c_q^{bckg} is the probability that the primary quark charge is correctly tagged by the particle misidenti£ed as K and $A_{q\bar{q}}$ are the quark asymmetries.

A_{FB}^{bckg} is computed directly from the full detector simulation. The dominant background is due to pions misidenti£ed as kaons. In order to reduce the statistical error on our estimate of A_{FB}^{bckg}, tracks have been identi£ed as pions in the RICHs. The pion momentum spectrum is re-weighted to make it similar to the spectrum of misidenti£ed kaons. The coef£cients α_q^{bckg} and c_q^{bckg} are computed for these events. All the quark asymmetries are £xed to the Standard Model values calculated by ZFITTER [7] with $M_{\mathrm{Z}} = 91.1866$ GeV/c^2, $m_t = 173$ GeV/c^2, $m_H = 115$ GeV/c^2, $\alpha_s = 0.122$ as input parameters. The background asymmetries computed for the three centre-of-mass energies (see Table 5.1) have statistical errors which are small compared to the systematic ones. The systematic error on A_{FB}^{bckg} is obtained by recalculating the α_q^{bckg} and c_q^{bckg} coef£cients by changing the relevant parameters in the simulation (listed in Table 6.6) for charm, bottom and light quark events. The results are summarised in Table 5.1.

$\sqrt{s}$ (GeV)	A_{FB}^{bckg}	
	Barrel	Forward
89.5	0.0104	0.0122
91.2	0.0020	0.0046
93.0	−0.0037	−0.0056
syst.error	0.0016	0.0030

Table 5.1: *The background asymmetry for different centre-of-mass energy and the systematic error on it.*

5.2 Asymmetry from interactions with the detector material

We use 2.4 M simulated hadronic events to extract the asymmetry from interactions of the charged kaons with the detector material. The fraction of positively charged kaons that interact with the material in front of the OD/FCB, α_{K^+}, is evaluated in bins of the kaon θ_{K}; α_{K^+} is corrected for kaons decaying on their way to the OD/FCB. The quantity $1-r_i$, which is equal to $2A_i^{mat}$, is evaluated as a function of α_{K^+}. The result is shown in Figure 5.1. The distribution of $2A^{mat}$ versus α_{K^+} is £tted using a parametrisation derived in Appendix A :

$$2A_i^{mat} = 1 - r_i \quad = \quad 1 - (1 - \alpha_{\mathrm{K}^+})^{\varepsilon_+} \tag{5.10}$$

The relative difference of K^- and K^+ cross-sections with the detector material in front of OD or FCB, ε_+, is found to be $0.089 \pm 0.005(\mathrm{stat.})$. The systematic error on ε_+ is 0.011 and is mainly (90%) coming from uncertainties in the difference in the nuclear cross-sections of $\mathrm{p(n)K^+}$ and $\mathrm{p(n)K^-}$. Using the parametrisation (5.10) and the values α_{K^+} obtained from the full simulation, the ratios r_i are extracted per mirror. The asymmetry A^{mat} as a function of the cosine of the polar angle is shown in Figure 5.2; it ranges from about 0.7% at small absolute values of $\cos\theta_K$ to 2% at values close to 1. The same parametrisation (5.10) is used to propagate the systematic error on ε_+ to the charged kaon forward-backward asymmetry. The overall effect on the kaon forward-backward asymmetry is very small due to the fact that the asymmetry from interactions with the detector material is symmetric in $\cos\theta$.

In deriving the parametrisation (5.10) or (A.5) we made two assumptions; £rstly, that one can average over the material and secondly, that one can average over the kaon momentum spectra for different mirrors. In order to check that the averaging over the material is justi£ed, a fast analytical calculation is done using the DELPHI materials database and the nuclear interaction cross-sections for a grid of points in the 3-dimensional space of K momenta, polar and azimuthal angles. The kaon momentum spectrum is considered to be the same for all polar angles. A weighted-mean according to the distributions of these three variables is computed for every mirror. The statistical error in this procedure is negligible. The points obtained in this method perfectly lie on the curve (5.10) with $\varepsilon_+ = 0.089$. The systematic error on ε_+ due to the averaging over the kaon momentum spectra, which are slightly different for different mirrors, amounts to 0.004.

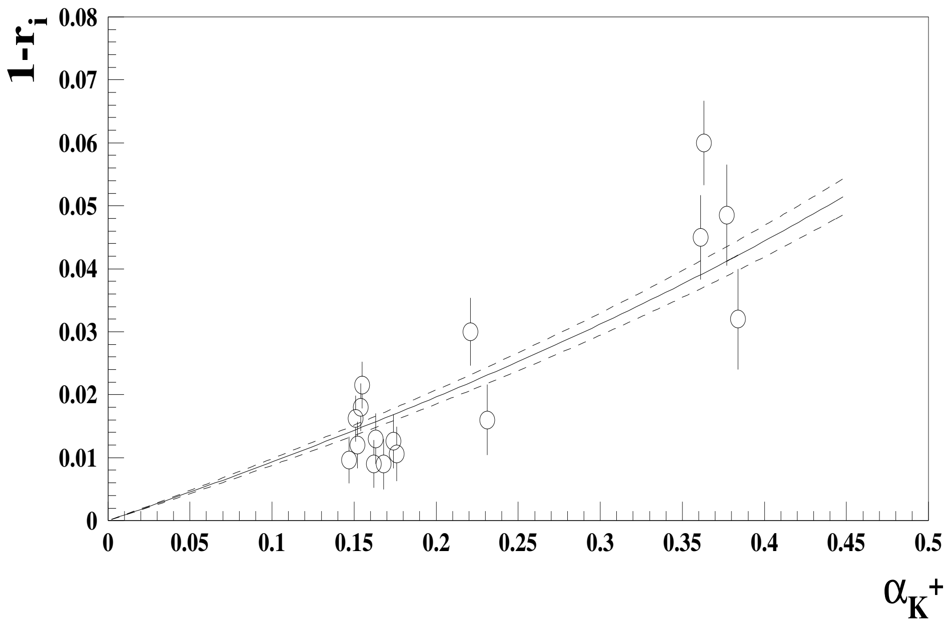

Figure 5.1: *The asymmetry from interactions with the material ($2A_i^{mat} = (1 - r_i)$) versus the fraction of stopped* K^+ *due to the interaction with the detector material. The superimposed curve represents the result of the £t; the dashed curves correspond to one standard deviation.*

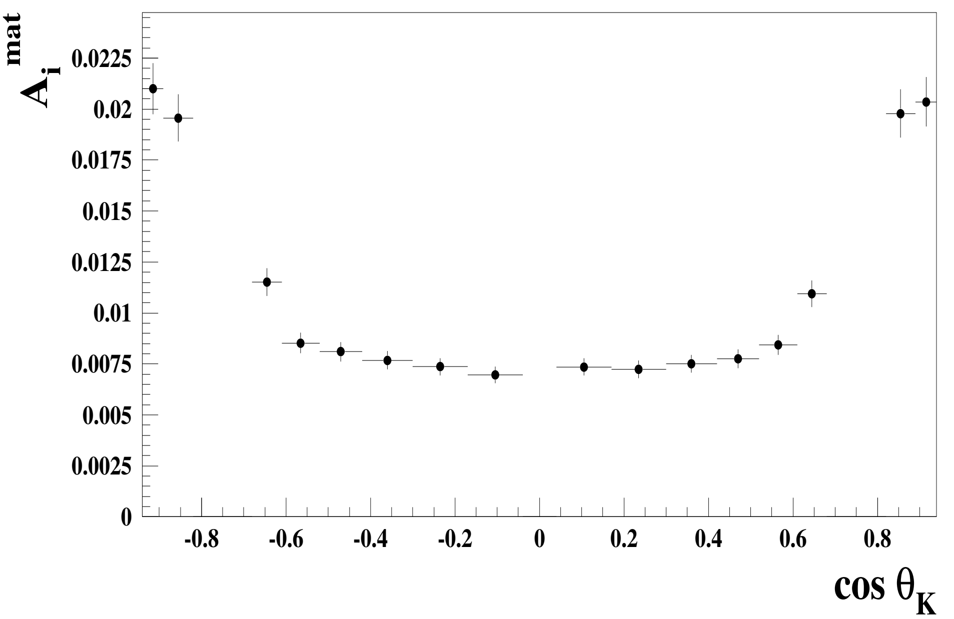

Figure 5.2: *The asymmetry from interactions with the material ($A_i^{mat} = \frac{1}{2}(1 - r_i)$) as a function of the* $\cos\theta$ *of the kaon. The errors are statistical only.*

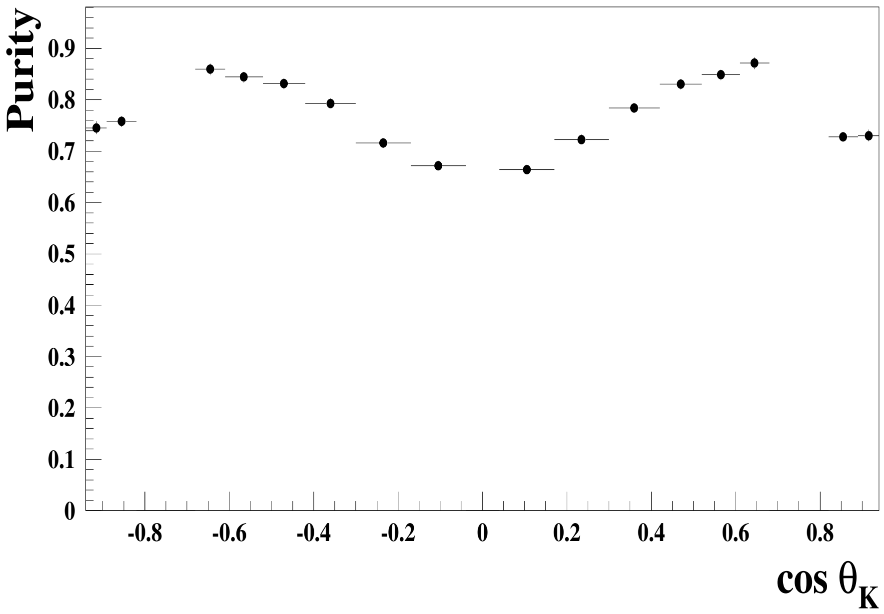

Figure 5.3: *For the 1994 data the charged kaon purity in the momentum range* $10 < p < 24$ *GeV/c in both RICHs is plotted as a function of the* $\cos\theta$ *of the kaon.*

5.3 Purity evaluation

The kaon purity is de£ned as the fraction of true kaons in the tagged kaon sample. It is obtained in two steps. In the £rst step the full DELPHI simulation is used to give the purity of the tagged kaon sample as a function of the kaon polar angle. In the second step a correction on these purity estimates is obtained. This accounts for small residual discrepancies between real and simulated data as become apparent from Figures 4.6 and 4.7 in Chapter 4. These discrepancies suggest that there is a correction to the $\pi^{\pm}$ misidenti£cation rate.

The distribution for the kaon purity in the real data is shown in Figure 5.3. On average it is 80% in the barrel region and 74% in the forward region, almost constant in the entire momentum window. The misidenti£ed particles are mainly pions and only 20% of the misidenti£ed particles are protons.
Two methods are used to estimate the correction to the MC kaon purity to obtain the purity for the real data.

In the £rst method the ratio of the $\pi^{\pm}$ misidenti£cation ef£ciencies in real and simulated data is found assuming that the kaon identi£cation ef£ciency is the same in real and simulated data. In the barrel region samples of high purity muons and of pions identi£ed in the TPC [2] are used to compare the $\pi^{\pm}$ misidenti£cation ef£ciency in real and simulated data for tracks with momenta between 10 and 24 GeV/c. The particle is selected as a pion (muon) candidate if its ionisation loss dE/dx is measured in the TPC using at least 80 wires and when the following conditions are satis£ed :

$$\frac{(\frac{dE}{dx})_{meas} - (\frac{dE}{dx})_{\pi,\mu}}{\sigma(\frac{dE}{dx})} > 0$$
$$\frac{(\frac{dE}{dx})_{meas} - (\frac{dE}{dx})_{K}}{\sigma(\frac{dE}{dx})} > 3$$

where $(\frac{dE}{dx})_{\pi,\mu,K}$ is the expected ionisation loss for the corresponding particle hypothesis. Furthermore, the muon candidate has to be tagged in the muon chambers in order to be put into the muon sample. The residual kaon contamination estimated from the simulated data is 0.35% in the muon and 2.0% in the pion samples. The results for different years are shown in Table 5.2.

The statistics in the μ-sample after kaon identi£cation by the RICH is very small and no momentum or angular dependence of the correction to the μ misidenti£cation ef£ciency is therefore possible. For muons the average ratio of the misidenti£cation rates in real and simulated data amounts to 1.41 ± 0.12(stat.) with a systematic error of 10%. The systematic error is due to the possible difference in the probability of a charged kaon to reach the muon chambers between real and simulated data. The simulated data indicate that the kaon contamination in the $\pi^{\pm}$-sample after kaon identi£cation by the RICH is 25%. Therefore only a rough estimation of the $\pi^{\pm}$ misidenti£cation ef£ciency can be made. For pions the average ratio of misidenti£cation rates amounts to 1.34 ± 0.02(stat.) with a systematic uncertainty of 20%. There is a good agreement between results of different years (see Table 5.2). This method can not be used in the forward analysis, as the pion (muon) sample can not be selected with a reasonable pion (muon) purity and statistics.

The second method, which is the method actually used to correct the purity, is based on the mean Cherenkov angle distribution. The Cherenkov angle distribution has two components: one Gaussian component centred around the expected Cherenkov angle for a given particle hypothesis, and one background term which is approximately a linear function of the Cherenkov angle (see section 3.5). Particles can be misidenti£ed either because of the small minimum separation—only two standard deviations—from the pion hypothesis, or because of the presence of background. To estimate these effects, particles with a Cherenkov angle θ_c outside the pion and kaon bands are selected in real and simulated data. Two regions are de£ned in which the number of particles is counted for the real and simulated data :

[2] The $m_{\pi} - m_{\mu}$ mass difference cannot be resolved by the TPC and the RICHs, see Figure 2.2 and 3.2.

Year	1992		1993	
	Data	Monte Carlo	Data	Monte Carlo
π sample	10598	84791	9685	86651
$\pi \to K$	575	3177	468	3309
$P_{\pi\to K}$ = Prob($\pi \to K$) %	5.42 ± 0.23	3.75 ± 0.07	4.83 ± 0.23	3.82 ± 0.07
$P_{\pi\to K}$ (Data) / $P_{\pi\to K}$ (MC)	1.45 ± 0.07		1.26 ± 0.06	
μ sample	781	5862	734	6074
$\mu \to K$	18	110	13	107
$P_{\mu\to K}$ = Prob($\mu \to K$) %	2.30 ± 0.55	1.88 ± 0.18	1.77 ± 0.50	1.76 ± 0.17
$P_{\mu\to K}$ (Data) / $P_{\mu\to K}$ (MC)	1.22 ± 0.32		1.0 ± 0.3	
Year	1994		1995	
	Data	Monte Carlo	Data	Monte Carlo
π sample	48570	281258	20783	60071
$\pi \to K$	2641	11182	1082	2509
$P_{\pi\to K}$ = Prob($\pi \to K$) %	5.44 ± 0.11	3.98 ± 0.04	5.21 ± 0.16	4.18 ± 0.09
$P_{\pi\to K}$ (Data) / $P_{\pi\to K}$ (MC)	1.37 ± 0.03		1.25 ± 0.05	
μ sample	3623	21521	1517	4381
$\mu \to K$	116	413	48	104
$P_{\mu\to K}$ = Prob($\mu \to K$) %	3.20 ± 0.30	1.92 ± 0.10	3.16 ± 0.46	2.37 ± 0.24
$P_{\mu\to K}$ (Data) / $P_{\mu\to K}$ (MC)	1.67 ± 0.18		1.33 ± 0.24	

Table 5.2: *Comparison of the misidenti£cation rate in the barrel RICH for real and simulated data of pions and muons samples.*

$$\text{region } R_1 : \quad \frac{\theta_c - \theta_c^\pi}{\sigma_{ring}} > 2.5$$

$$\text{region } R_2 : \quad \frac{\theta_c - \theta_c^K}{\sigma_{ring}} > 2.5 \text{ and } \frac{\theta_c - \theta_c^\pi}{\sigma_{ring}} < -2.5.$$

Figure 5.4 shows the ratios of the number of particles in these regions for the 1994 data. A small Monte Carlo program described in the next paragraph shows that at most 10% of the total number of tracks in each of these regions can be attributed to the Gaussian tail. Background photons, accordingly, have to play a dominant role in the misidenti£cation. The results for the ratios and the fact that the Cherenkov angle distribution for background photons depends almost linearly on this angle imply that the number of background photons per track in the simulated data has to be increased with a scaling factor that for the 1992-5 data amounts to 1.4 ± 0.1 in the barrel region, and 1.05 ± 0.1 in the forward region. The scaling factors are similar for regions R_1 and R_2. The misidenti£cation rates ratio for pions and for muons shown in Table 5.2 is compatible with this result.

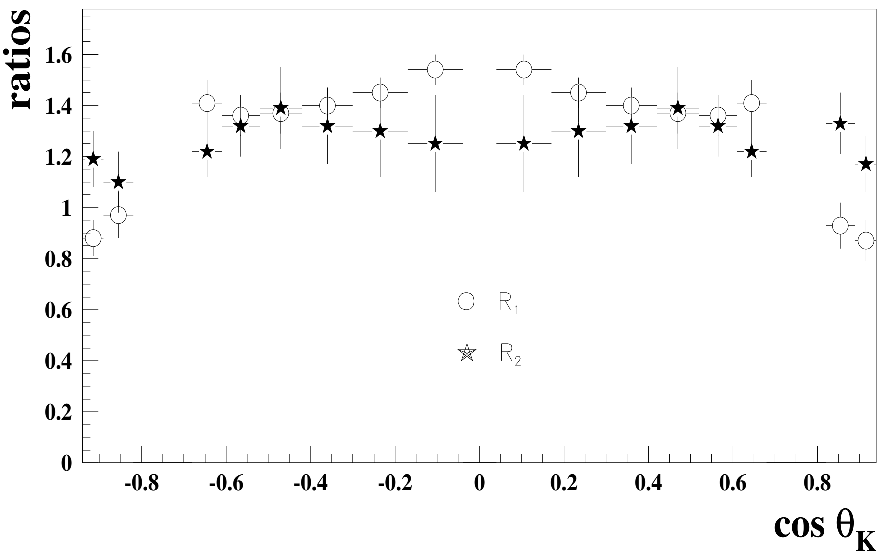

Figure 5.4: *The ratios of data to Monte Carlo backgrounds in the regions R_1 and R_2. This £gure corresponds to the 1994 data.*

A small simulation program was written to understand these results. This is done in the following way :

1. π's, K's and p's are generated with the proper momentum spectra, according to the measured fractions, with momenta p between 10 and 24 GeV/c.

2. A number of Cherenkov photons is generated according to a Poisson law with mean N_{signal}. The average number of signal photons N_{signal} is according to equation (3.9), a function of the expected Cherenkov angle. Moreover, it varies as a function of the mirror number because the track length in gas radiator and the detection ef£ciency of photoelectrons are different for different mirrors.

3. A number of background photons is generated according to a Poisson law with mean N_{bckg}. The average number of background photons varies as a function of the mirror number because the background conditions vary from mirror to mirror.

4. For each photon an expected error on the angle, σ^{exp}_{photon}, is generated according to a Gaussian distribution:
$$\propto \exp(-\frac{(\sigma - \sigma_p)^2}{2\sigma_r^2}).$$
The momentum dependence of the error for a given mirror is described by $\sigma_p = A + B \cdot \sqrt{1 + C/p}$. The σ_r re¤ects the fact that tracks of the same mirror can have different

σ^{exp}_{photon} regardless of their momentum due, for example, to a dependence on the polar angle of the track. The coef£cients A, B, C and the σ_r must be determined per mirror.

5. The background photons are generated according to a linear distribution: $\theta^{max}_c \cdot \sqrt{r}$, where r is a random number between 0 and 1, and $\theta^{max}_c = 0.09\,\mathrm{rad}$ is the maximal allowed Cherenkov angle. This corresponds to a uniformly distributed background in space.

6. The Cherenkov angle for a Cherenkov photon is generated according to a Gaussian distribution with mean equal to the expected Cherenkov angle of the corresponding particle hypothesis $\theta^{exp}_{\pi,\mathrm{K},p}$ and with a r.m.s. of σ^{exp}_{photon}.

7. The RIBMEAN clustering algorithm is applied to combine photons into a ring and determine the average Cherenkov angle θ^{mean}_c. It gives also the number of photons for this ring N.

8. The expected error per ring σ_{ring} is de£ned as $\sigma^{exp}_{photon}/\sqrt{N}$.

9. No ambiguous photons are generated.

The unknown parameters in this Monte Carlo, which cannot be directly determined, are the expected numbers of Cherenkov photons in the real and simulated data (N^{RD}_{signal}, N^{MC}_{signal}) and the average numbers of background photons in the real and simulated data (N^{RD}_{bckg}, N^{MC}_{bckg}). For the average numbers of photons in the real and simulated data we use the following constraint: $N^{RD}_{bckg} = N^{MC}_{bckg} \cdot R$. Where R for a given mirror corresponds to the weighted average of the ratios R_1 and R_2 of tracks in real and simulated data in the regions R_1 and R_2, respectively (see Figure 5.4). Three unknowns are therefore left. Four observables are used to determine these free parameters, they are the average numbers of observed photons per track in the real and simulated data and the observed values of R_1 and R_2. These observables de£ne the χ^2-function as a function of the three variables (N^{RD}_{signal}, N^{MC}_{signal}, N^{MC}_{bckg}). For one degree of freedom the χ^2 equals approximately unity at the minimum. For different values of these variables two sets of 100k tracks were generated. One set is generated with the parameters A, B, C, σ_r determined from the real data and the other with the parameters A, B, C, σ_r determined from the simulated data. For each set of tracks the kaon purity was determined by identifying kaons using the criteria on the average Cherenkov angle θ^{mean}_c (see section 4.2, Equations (4.1)-(4.2)).

For the minimization the algorithm described in Appendix B was used. For the numerical calculation of the derivatives a step of 0.2 was used for each variable. This guarantees a correct sign for the function derivatives. The £t is done separately for each of the six mirrors in the Barrel (we consider the BRICH to be symmetric in $\cos\theta_K$) and for each of the four mirrors in the Forward (the forward and backward halves of the FRICH are considered separately for the purity analysis). For all mirrors the χ^2 is well behaved. As an example, for one of the BRICH mirrors a χ^2 minimum of about 1 is obtained for values ($N^{RD}_{signal} = 7.6 \pm 0.1, N^{MC}_{signal} = 7.8 \pm 0.1, N^{MC}_{bckg} = 1.4 \pm 0.1$). We have used different starting points, $\chi^2(7,9,2) = 45$, $\chi^2(9,7,2) = 54$, $\chi^2(7,7,2) = 16$, $\chi^2(9,9,2) = 37$, to verify the convergence of the £t. In all cases the above minimum is successfully reached after 6-12 steps. The parameters found at the minimum have errors due to the limited statistics of the Monte Carlo function. After the £t is done, the £nal difference between the kaon purities is obtained. These purities correspond to the two Monte Carlo samples. One sample was generated with the input parameters A, B, C, σ_r for the simulated data and with £tted values of N_{bckg}^{MC}, N_{signal}^{MC}; the other was generated with the input parameters A, B, C, σ_r for the real data and with £tted values of N_{bckg}^{RD}, $N_{signal}^{RD} = R \cdot N_{signal}^{MC}$. The shift in the kaon purity is the correction to the purity obtained from the simulated data in order to estimate the kaon purity in the real data.

An increase in the number of background photons that are generated according to a linear function can explain the observed scaling factors. After scaling up the background, the kaon purities extracted from the simulated data are decreased depending on the polar angle by 0.4% to 4.9% (the correction term decreases when $|\cos\theta_{\rm K}|$ increases). In Figure 5.3 the purity is shown after applying this correction. With the simulation program the systematic effect due to a shift in the mean Cherenkov angle and discrepancies in the expected error per ring can be evaluated. From the comparison between real and simulated data it was found that the Cherenkov angle can be shifted at most by 0.25 mrad and the resolution of the Cherenkov angle per ring is at most 5% larger than in the simulated data. The systematic error on the kaon purity due to the background, Cherenkov angle shift and ring resolution is 1%. The purity is evaluated for each data-taking year.

5.4 Results

The corrected kaon purities, the results for the asymmetry of misidenti£ed particles and for the asymmetry from interactions with the material are used to evaluate the asymmetry A_i^{obs} (5.4) for each θ_K bin, as explained in section 5.1. The corresponding weights w_i (5.7) are also evaluated and used to £t the χ^2 function (5.6).

Results for the on-peak measurements

In the barrel region, 73329 events are selected and used to compute the charged kaon forward-backward asymmetry.

The results of the £t minimizing the χ^2 function (5.6) are summarised in Table 5.3.

As a consistency check the asymmetries are £tted separately for each detector side, giving the compatible results :

$$\begin{aligned} A_{FB}^K(z>0) &= 0.0421 \pm 0.0068\,(\text{stat.}) \\ A_{FB}^K(z<0) &= 0.0387 \pm 0.0070\,(\text{stat.}). \end{aligned} \tag{5.11}$$

Year	Barrel		Forward	
	# events	A^K_{FB}	# events	A^K_{FB}
1992	10171	0.032 ± 0.013	—	
1993	4948	0.002 ± 0.019	—	
1994	43523	0.0450 ± 0.0063	9342	0.031 ± 0.011
1995	14687	0.047 ± 0.011	4151	0.058 ± 0.015
1992-5	73329	0.0405 ± 0.0049	13493	0.039 ± 0.009

Table 5.3: *The measurements of A^K_{FB} at 91.2 GeV for the 1992-1995 data. The errors are statistical.*

In the forward region, 13493 events are selected and the results are also summarised in Table 5.3.

Results for the off-peak measurements

The statistics and results of the £t for the off-peak measurements are listed in Table 5.4.

$\sqrt{s}$ (GeV)	Year	Barrel		Forward	
		# events	A^K_{FB}	# events	A^K_{FB}
89.5	1993	1981	0.023 ± 0.029	—	
	1995	2305	0.028 ± 0.028	719	-0.005 ± 0.037
	1993,5	4286	0.025 ± 0.020	719	-0.005 ± 0.037
93.0	1993	3020	0.010 ± 0.024	—	
	1995	3362	0.067 ± 0.023	1193	0.044 ± 0.029
	1993,5	6382	0.040 ± 0.017	1193	0.044 ± 0.029

Table 5.4: *The measurements of A^K_{FB} at 89.5 GeV and 93.0 GeV for the 1993 and 1995 data. The errors are statistical.*

A consistency check for the forward measurements

As a consistency check, the asymmetries are £tted separately for each FRICH detector side. In order to gain statistics we use the on-peak and off-peak measurements in the forward region. Since the asymmetry is a function of energy, only the difference between the measured forward-backward asymmetries can be used for the comparison. The difference is compatible with zero :

$$A^K_{FB}(z<0) - A^K_{FB}(z>0) \;=\; 0.015 \pm 0.016\,(\text{stat.}). \tag{5.12}$$

Systematic errors to the charged kaon asymmetry

The contributions to the experimental uncertainty of A_{FB}^{K}, come from the uncertainties on the kaon purities, the uncertainty in the ε_+ determination and the propagation of the systematic error on A_{FB}^{bckg}. They are the same for on and off peak measurements and are listed in Table 5.5. The parameterisation (5.10) is used to propagate the uncertainty in ε_+ into a systematic error on the charged kaon asymmetry. The systematic error on A_{FB}^{bckg} comes from the variations in the coef£cients α_q^{bckg} and c_q^{bckg}, which are evaluated by the procedure described in section 6.4. One can see that the total systematic error on A_{FB}^{K} is one order of magnitude smaller than the statistical error.

Contributions to the systematic error on A_{FB}^{K} ($\times 10^{-4}$)	Barrel	Forward
Kaon purity	1.3	2.5
K^+/K^- interactions with material	0.2	0.7
A_{FB}^{bckg}	4.6	8.2
Total	4.8	8.6

Table 5.5: *Contributions to the systematic uncertainty on the charged kaon asymmetries in the Barrel and in the Forward regions.*

Chapter 6

s quark asymmetry

In this chapter we determine the following quantities:

- the s quark forward-backward asymmetry A^s_{FB} as a function of energy;
- the s quark pole asymmetry $A^0_{s\bar{s}}$, i.e. the asymmetry at the Z^0 pole as de£ned in equation (1.24).

These quantities are derived from the charged kaon asymmetry A^K_{FB} of which the measurement was described in the previous chapter. Furthermore, a detailed evaluation of the systematic errors on these values is presented. The results are compared with the Standard Model expectation. From $A^0_{s\bar{s}}$ we obtain the effective electroweak mixing angle $\sin^2\theta^{lept}_{eff}$. In addition the parity violating coupling A_s of the s quark to the Z^0 is determined.

6.1 Procedure

The s quark asymmetry after QCD corrections and hadronisation, $A_{s\bar{s}}$, is extracted from the charged kaon asymmetry using the expression (5.1) :

$$A_{s\bar{s}}(s) = \frac{1}{\alpha_s(2c_s-1)}\times \times\left[A^K_{FB}(s) - \sum_{q=d,u,c,b}\alpha_q(2c_q-1)A_{q\bar{q}}\right] \tag{6.1}$$

The coef£cients α_q correspond to the fractions of selected events with primary quark q. They can be expressed as a product of R_q, $R_q = \Gamma_q/\Gamma_{had}$ with Γ_q the partial hadronic width for ¤avour q and Γ_{had} the total hadronic width, and the ¤avour tagging ef£ciency ϵ_q :

$$\alpha_q = \frac{R_q\epsilon_q}{\sum_{f=d,u,s,c,b}R_f\epsilon_f} \quad . \tag{6.2}$$

Flavour	Barrel		Forward	
	α_q	c_q	α_q	c_q
d	0.1425 ± 0.0013	0.328 ± 0.004	0.1038 ± 0.0021	0.329 ± 0.009
u	0.1356 ± 0.0012	0.264 ± 0.004	0.0979 ± 0.0020	0.246 ± 0.009
s	0.5523 ± 0.0029	0.868 ± 0.002	0.4290 ± 0.0048	0.878 ± 0.003
c	0.1600 ± 0.0013	0.835 ± 0.003	0.2331 ± 0.0033	0.859 ± 0.005
b	0.0091 ± 0.0003	0.809 ± 0.013	0.1359 ± 0.0024	0.809 ± 0.007

Table 6.1: *Computed values for ¤avour selected fractions (α_q) and quark charge identi£cation ef£ciencies (c_q) for the barrel and forward regions in the 1994 data. The errors are statistical only.*

The values of R_q are computed with ZFITTER while the coef£cients ϵ_q are evaluated using JETSET PS 7.3 with the full DELPHI simulation. The values are given in Table 6.1. From this evaluation we also obtain the coef£cients c_q, which are the probabilities that the kaon charge corresponds to the charge of the primary quark after the QCD parton cascade (see section 1.5).

The asymmetries $A_{q\bar{q}}$ in equation (6.1) can be expressed in terms of the the asymmetries A^q_{FB} which are the asymmetries without perturbative QCD effects and before hadronisation :

$$A_{q\bar{q}}(s) \quad = \quad A^q_{FB}(s) \cdot (1 + C^{thrust}_q). \tag{6.3}$$

The coef£cients C^{thrust}_q take into account the fact that the quark direction as estimated from the thrust axis differs from the true one. This is because of QCD gluon emission, hadronisation and decays, and experimental problems in the reconstruction of the thrust axis due to undetected particles and to the momentum and energy resolution. These coef£cients are computed using JETSET PS 7.3 and the full detector simulation :

$$C^{thrust}_q = \frac{\sum_f \left(\frac{\cos(\theta^i_q)}{1+\cos^2(\theta^i_q)} - \frac{\cos(\theta^f_q)}{1+\cos^2(\theta^f_q)} \right)}{\sum_f \frac{\cos(\theta^f_q)}{1+\cos^2(\theta^f_q)}}, \tag{6.4}$$

where θ^i_q is the initial state quark polar angle (i.e., before gluon emission) and θ^f_q the estimate of this angle using the polar angle of the thrust axis. It should be noted that when we perform the summing in (6.4) we ¤ip both the sign of $\cos\theta^f_q$ and the sign of $\cos\theta^i_q$ when $\cos\theta^f_q$ is negative. The C^{thrust}_q values are given in Table 6.2. The JETSET 7.3 program includes apart from £rst order QCD corrections also higher order ones. We refer to [29] for details.

The £nal formula that is used to determine the s quark forward-backward asymmetry is :

$$\begin{aligned} A^s_{FB}(s) = \frac{A_{s\bar{s}}}{1 + C^{thrust}_s} = \frac{1}{\alpha_s(2c_s - 1)(1 + C^{thrust}_s)} \times \\ \times \left[A^K_{FB}(s) - \sum_{q=d,u,c,b} \alpha_q(2c_q - 1)A^q_{FB}(1 + C^{thrust}_q) \right] \end{aligned} \tag{6.5}$$

Flavour	C_q^{thrust}	
	Barrel	Forward
d	-0.029 ± 0.006	-0.013 ± 0.004
u	-0.029 ± 0.006	-0.018 ± 0.005
s	-0.025 ± 0.003	-0.012 ± 0.002
c	-0.020 ± 0.005	-0.011 ± 0.003
b	-0.035 ± 0.015	-0.005 ± 0.002

Table 6.2: *Correction coef£cients C_q^{thrust} take into account effects due to QCD gluon emission, fragmentation and thrust axis reconstruction when the thrust axis direction is used as an estimator for the quark direction.*

Flavour	QED	$\sqrt{s} \neq m_Z$	$\gamma, \gamma Z^0$
d	-0.0042	0.0015	0.0003
u	-0.0109	0.0040	0.0007
s	-0.0042	0.0015	0.0003
c	-0.0109	0.0040	0.0007
b	-0.0042	0.0015	0.0003

Table 6.3: *Correction coef£cients $(\delta A_{q\bar{q}})_i$ calculated with the ZFITTER program as described in [30].*

where $A_{FB}^K(s)$ is the measured charged kaon forward-backward asymmetry listed in Tables 5.3 and 5.4. We determine the asymmetries independently in the barrel and forward regions because of the different systematic errors, in particular, due to the heavy quark rejection applied in the barrel region. To take into account possible annual variations in the heavy quark rejection, the asymmetries are determined separately for each year. In equation (6.5) the predicted asymmetries from the Standard Model for down, up, charm and bottom quarks ($A_{FB}^q(s),\ q = d, u, c, b$) are used. They are computed with ZFITTER, see Table 1.3.

To determine the s quark pole asymmetry $A_{s\bar{s}}^0$ (see Formulas (1.16) and (1.24)), we recall that A_{FB}^s includes the photon exchange contribution to quark pair production (see section 1.3 and equation (1.15)). The asymmetries $A_{q\bar{q}}$ in equation (6.1) are written in terms of the pole asymmetries $A_{q\bar{q}}^0$ according to the following expression (compare to (6.3)):

$$A_{q\bar{q}}(\sqrt{s} = 91.2\text{GeV} \simeq m_Z) \quad = \quad (A_{q\bar{q}}^0 - \sum_i (\delta A_{q\bar{q}})_i) \cdot (1 + C_q^{thrust}) \, . \tag{6.6}$$

The $(\delta A_{q\bar{q}})_i$ terms take into account corrections to the asymmetry due to QED radiative corrections coming from photon emission, the fact that the asymmetry has been measured at $\sqrt{s} \neq m_Z$, and the $\gamma, \gamma Z$ terms in the Born expression. All these coef£cients are computed with ZFITTER, see reference [30]. They are listed in Table 6.3.

In order to compute $A_{s\bar{s}}^0$ the c and b pole asymmetries are £xed to the values measured at

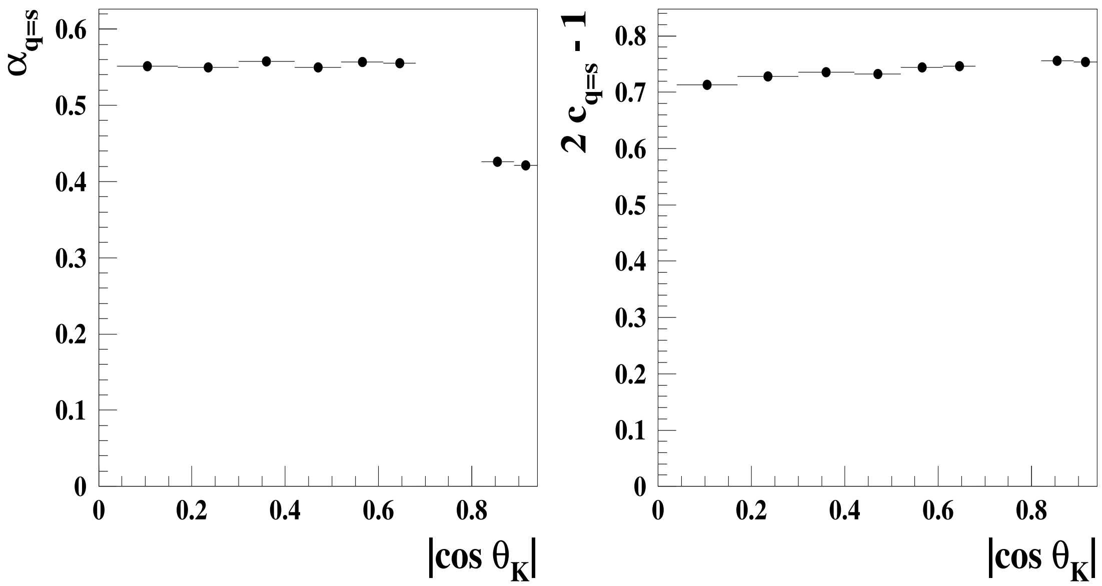

Figure 6.1: *The fraction of selected events with the primary s quark (left) and the probability that the kaon charge corresponds to the charge of the primary s quark in 1994. The errors plotted are due to the limited statistics of simulated events.*

LEP/SLD [30] :

$$\begin{aligned} A^0_{b\bar{b}} &= 0.0990 \pm 0.0021 \\ A^0_{c\bar{c}} &= 0.0709 \pm 0.0044. \end{aligned} \tag{6.7}$$

while the u and d pole asymmetries are £xed to the Standard Model values $A^0_{d\bar{d}}$=0.1031 and $A^0_{u\bar{u}}$=0.0736.

6.2 Some checks

In equation (6.5) we assume that α_q and c_q are constant as a function of the polar angle in both the barrel and forward regions. Figure 6.1 shows that the fraction of s quark events α_s indeed does not change with the polar angle within the barrel and forward regions. The fractions are different, however, in these regions. The difference is due to the heavy quark rejection in the barrel region. Figure 6.1 also shows that $c_{q=s}$ increases slightly for increasing $|\cos\theta_K|$. This is due to the fact that the kaon momentum spectrum is different for different polar angle intervals.

Barrel region

As mentioned in section 5.1 the bins of $|\cos\theta_K|$ where the charged kaon asymmetry is measured correspond to the angular ranges covered by the RICH mirrors. Because the conditions for Cherenkov photon production and detection vary with $|\cos\theta_K|$, the kaon momentum spectrum becomes harder for high values of $|\cos\theta_K|$. To illustrate this the kaon momentum spectrum for the £rst and sixth mirror in the Barrel RICH is shown in Figure 6.2a and Figure 6.2b, respectively. A good agreement between the real and simulated data for the kaon momentum spectrum is observed for all mirrors.

To £nd a correction to the s quark asymmetry obtained from (6.5) due to the dependence of the kaon momentum on polar angle, $2c_q - 1$ and α_q are parameterised as a linear function of the the polar angle and the s quark forward-backward asymmetry is determined in each polar angle bin. The asymmetries obtained in this way are combined and the resulting value is compared with the one obtained from (6.5). The difference was found to be 0.0006.

Forward region

The average number of Cherenkov photons is smaller for the FRICH than that for the BRICH, see Figure 3.7. The requirement for a Cherenkov ring to have at least 2 photons rejects kaons with momentum close to the threshold where no Cherenkov light can be produced. This effectively enhances the contribution of high momentum kaons. The kaon momentum spectrum of the FRICH is shown in Figure 6.2 c. Again, a good agreement between the real and simulated data is observed. As the momentum spectrum is similar for both FRICH mirrors, no further corrections to the s quark asymmetry obtained from (6.5) is needed.

Conclusion

We can conclude that one can use the approximate formula (6.1) in the barrel region if the asymmetry is shifted by 0.0006. In the forward region no shift has to be applied.

6.3 Results

The determination of A^s_{FB} depends on the value assumed for the strange quark suppression factor γ_s, which is the probability for the primary quark to pick up an s-quark in the fragmentation process. A value γ_s=0.307 is used in the DELPHI JETSET simulation. The DELPHI tuning of γ_s in JETSET using the K^0 and $K^\pm$ momentum spectra gave inconsistent results [14]. The s quark pole asymmetries in this analysis will therefore be evaluated using a more recent value of 0.285 for γ_s [31] with a systematic error accounting for this shift. In section 6.4.2 it will be shown that the change in the calculated s quark asymmetry due to a variation in γ_s can be parametrised as $\Delta A^0_{s\bar{s}} = 0.17\,\Delta\gamma_s$.

Using the results for the charged kaon forward-backward asymmetry A^K_{FB} in Table 5.3, the s quark pole asymmetry is computed as explained in section 6.1 for each data set. The

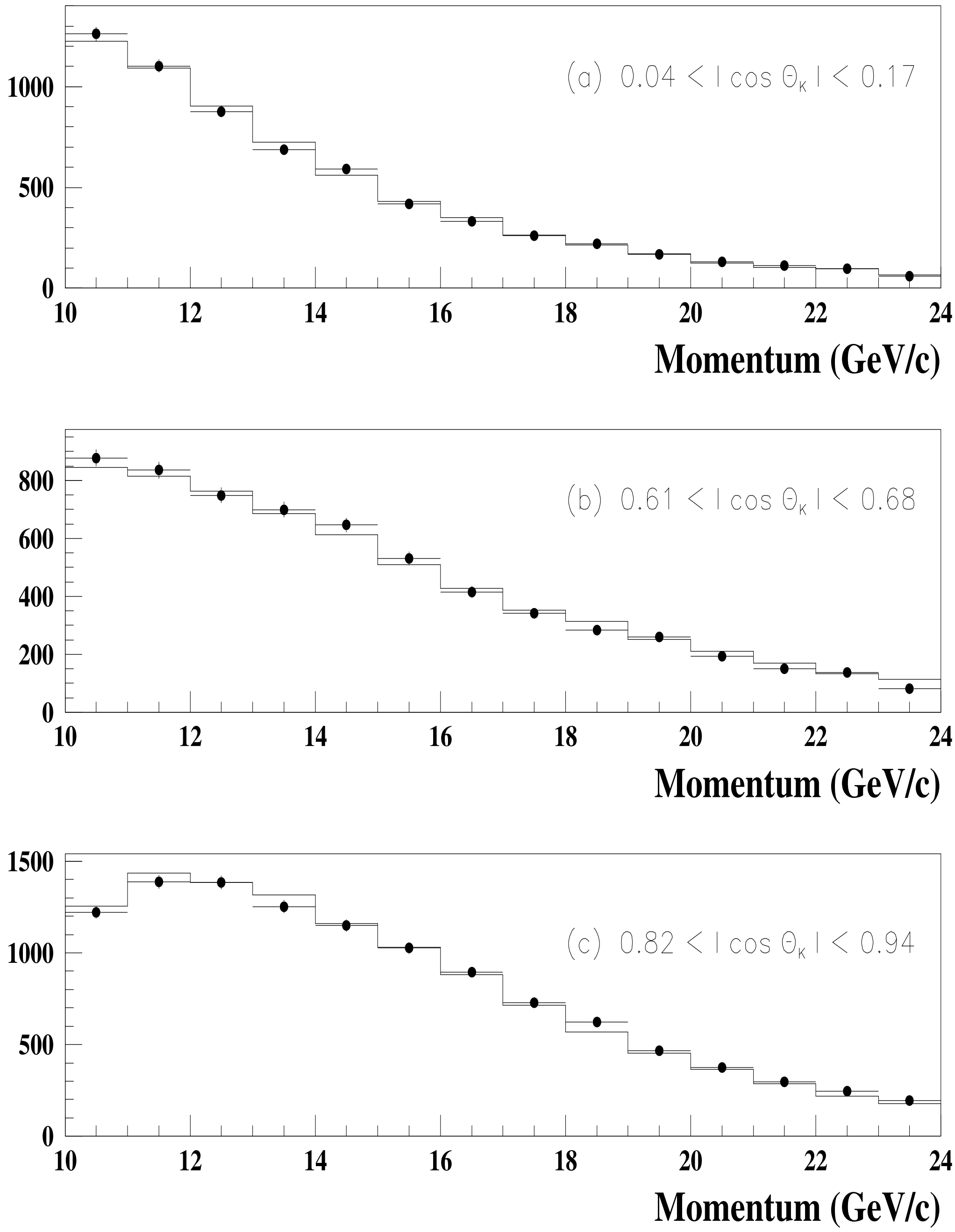

Figure 6.2: *The momentum distribution of the selected kaons for 1994 data (dots) and simulation (histograms): a) for the mirrors closest to the Central Wall of the BRICH or the so-called £rst mirrors (see Figure 3.4; b) for the mirrors that are closest to the end of the BRICH or the so-called sixth mirrors; c) for the FRICH mirrors combined.*

Year	$A^0_{s\bar{s}}$	
	Barrel	Forward
1992	0.081 ± 0.033	—
1993	0.007 ± 0.048	—
1994	0.115 ± 0.016	0.058 ± 0.034
1995	0.120 ± 0.028	0.140 ± 0.050
1992-5	0.104 ± 0.012	0.084 ± 0.028

Table 6.4: *Summary of the determination of $A^0_{s\bar{s}}$ for the 1992-1995 data. The errors are statistical only.*

$\sqrt{s}$ (GeV)	A^s_{FB}	
	Barrel	Forward
89.5	0.073 ± 0.051	-0.013 ± 0.119
91.2	0.102 ± 0.012	0.081 ± 0.028
93.0	0.095 ± 0.043	0.065 ± 0.092

Table 6.5: *Summary of the determination of A^s_{FB} for the 1992-1995 data. The errors are statistical only.*

results are summarised in Table 6.4. They are compatible for the different years.

Using the results for the A^K_{FB} in Tables 5.3 and 5.4, the forward-backward asymmetry at centre-of-mass energies of 89.5, 91.2 and 93.0 GeV are calculated. The results are summarised in Table 6.5.

6.4 Systematic errors

The systematic errors on the s quark asymmetry are due to uncertainties on the α_q and c_q coef£cients in Formula (6.1) and due to the systematic error on the value of A^K_{FB} given in Table 5.5. A detailed breakdown of all the error sources is discussed below with an estimate of their effect on $A^0_{s\bar{s}}$, see Table 6.6. The systematic errors are quite different for the barrel and forward regions due to the different event selection used. The rejection of heavy quarks in the barrel region substantially reduces the systematic error coming from charm and bottom quarks. The £rst three lines in Table 6.6 give successively the contributions to the systematic error on $A^0_{s\bar{s}}$ due to :

- the uncertainties for the charm and bottom forward-backward asymmetries as given in (6.7) taking into account a 10% correlation between these two quantities;
- the systematic error on the kaon asymmetry A^K_{FB} listed in Table 5.5;

- The effect on the s asymmetry from the £nite momentum resolution of the K was computed with the full DELPHI simulation selecting events according to the true momentum of the K instead of the reconstructed one.

The rest of Table 6.6 gives all other contributions to $\delta A^0_{s\bar{s}}$ from uncertainties in the Monte Carlo modelling. They can be split into four classes: systematic uncertainties from the charm quark, bottom quark, light quark fragmentation, and heavy quark rejection in the barrel region. They are discussed in more detail in the following subsections.

6.4.1 Systematic error due to uncertainties in the modelling of heavy quark fragmentation and decay

The contribution to the systematic error for heavy quarks comes from uncertainties in: the production fractions of charmed (bottom) hadrons; the average decay multiplicity of c (b) hadrons; the mean fraction of the energy of the primary c (b) quark taken by the $c-$ ($b-$) hadron $< x_c >$ ($< x_b >$); the branching ratios into $\mathrm{K}^{\pm}$ for D^0, $\mathrm{D}^{\pm}$, $\mathrm{D_s}$, B^0, $\mathrm{B}^{\pm}$ and b-quark decays. In the case of b-quarks there is in addition a contribution due to the uncertainty in the mixing parameter x_d for $\mathrm{B_d}$. The uncertainties on the above-mentioned quantities are listed in Table 6.6. They are taken from [29], [32], [33].

The simulated events are re-weighted according to the uncertainties in these quantities. For example to propagate the uncertainty in $f(\mathrm{D}^{\pm})$ the selected event with a kaon coming from a $\mathrm{D}^{\pm}$ decay is given a weight $\frac{f(\mathrm{D}^{\pm})+\Delta f(\mathrm{D}^{\pm})}{f(\mathrm{D}^{\pm})}$. This leads to different values of α_q and c_q which then are used to determine $\delta A^0_{s\bar{s}}$.

6.4.2 Systematic error due to uncertainties in the modelling of light quark fragmentation

Uncertainties in the parameters describing the fragmentation process of up, down and strange quarks are studied using the JETSET 7.3 PS, using as a starting point the values of these parameters obtained by a tuning procedure described in [14] for LEP data. The JETSET parameters are varied within the statistical and systematic errors given in Table 6.7 and in Table 48 of reference [14].

To determine which parameters are the most important, an analytic (quadratic) approximation is used for the variation of the asymmetry as a function of the model parameters :

$$\delta A^0_{s\bar{s}} = \sum_{i=1}^{n} a_i^{(1)} \delta p_i \; + \; \sum_{i=1}^{n} \sum_{j=1}^{n} a_{ij}^{(2)} \delta p_i \delta p_j \tag{6.8}$$

In this equation, $n = 9$ is the number of parameters considered (see Table 6.7), δp_i is the deviation of parameter i from its nominal JETSET value. To determine the $m = n + n(n+1)/2$ coef£cients $a^{(1,2)}$ of the expansion m reference samples of 2 million events are generated with different parameter settings. For each parameter three different settings were used: the

Systematic source	$\delta A^0_{s\bar{s}}$ ($\times 10^{-4}$)	
	Barrel	Forward
A^0_c and A^0_b	16.5	26.7
A^K_{FB}	11.9	25.8
$K^{\pm}$ momentum resolution	6.5	4.8
Total	21.4	37.4
$f(D^{\pm}) = 0.233 \pm 0.028$	0.2	0.4
$f(D^0) = 0.557 \pm 0.053$	7.3	15.2
$f(D_s) = 0.102 \pm 0.037$	5.6	12.0
$f(c_{barion}) = 0.065 \pm 0.029$	1.0	1.9
c hadrons decay multiplicity $= 2.35 \pm 0.06$	0.2	0.5
$< x_c >= 0.484 \pm 0.008$ (charm fragmentation)	1.2	2.3
BR$(D^0 \to K^- X) = 53 \pm 4\%$	2.5	5.0
BR$(D^0 \to K^+ X) = 3.4 + 0.6 - 0.4\%$	1.4	3.0
BR$(D^+ \to K^- X) = 24.2 \pm 2.8\%$	1.4	3.1
BR$(D^+ \to K^+ X) = 5.8 \pm 1.4\%$	2.2	4.7
BR$(D_s \to K^- X) = 13 + 14 - 12\%$	1.7	3.3
BR$(D_s \to K^+ X) = 20 + 18 - 14\%$	7.0	15.5
Total uncertainty from c quark sector	12.4	26.5
$f(B^{\pm}) = 37.8 \pm 2.2\%$	0.2	4.7
$f(B^0) = 37.8 \pm 2.2\%$	0.1	1.2
$f(B_s) = 11.2 \pm 1.9\%$	0.2	3.5
$f(b_{barion}) = 13.2 \pm 4.1\%$	0.1	2.0
b hadron decay multiplicity $= 5.73 \pm 0.35$	0.2	4.9
$< x_b >= 0.702 \pm 0.008$ (bottom fragmentation)	0.2	4.3
BR$(B^0 \to K^- X) = 0.13 \pm 0.04$	0.9	17.9
BR$(B^0 \to K^+ X) = 0.73 \pm 0.08$	0.2	6.2
BR$(B^+ \to K^- X) = 0.13 \pm 0.05$	0.5	11.7
BR$(B^+ \to K^+ X) = 0.58 \pm 0.08$	0.3	8.5
BR$(D_s \to K^- X)$ from b quark	0.3	7.9
BR$(b \to K^{\pm} X) = 88 + 12 - 19\%$	1.4	34.6
BR$(D_s \to K^+ X)$ from b quark	0.1	1.6
B_d mixing: $x_d = 0.70 \pm 0.04$	-	2.3
Total uncertainty from b quark sector	1.9	43.8
Impact parameter resolution	0.3	-
photon conversion $\pm 30\%$	1.2	-
$K^0_S(u,d,s) \pm 10\%$	0.3	-
$\Lambda(u,d,s) \pm 10\%$	0.3	-
$g \to c\bar{c} \pm 50\%$	0.5	-
$g \to b\bar{b} \pm 50\%$	0.1	-
b hadrons lifetimes	0.1	-
D mesons lifetimes	0.1	-
Total uncertainty from the heavy quark rejection	1.4	-
Statistical error on γ_s	11.9	11.9
Shift in γ_s	18.7	18.7
Variation of the K/π ratio	7.8	7.8
Total uncertainties from light quark fragmentation	23.5	23.5
Total systematic error	34.2	67.6

Table 6.6: *Summary of the systematic errors on s quark pole asymmetry using the Standard Model values for the up and down quark pole asymmetry.*

	Parameter	Name	Range gen.	Fit result [14]		
				Value	stat.	syst.
Group 1	$P(^1S_0)_{ud}$	—	0.172 - 0.372	0.272	±0.030	$^{+0.108}_{-0.008}$
	$P(^1S_1)_{ud}$	—	0.206 - 0.406	0.306	±0.049	$^{+0.006}_{-0.031}$
	γ_s	PARJ(2)	0.257 - 0.357	0.307	±0.007	$^{+0.002}_{-0.017}$
	$P(^1S_0)_s$	—	0.31 - 0.51	0.416	±0.029	$^{+0.015}_{-0.003}$
	$P(^3S_1)_s$	—	0.197 - 0.397	0.304	±0.023	$^{+0.017}_{-0.002}$
Group 2	Λ_{QCD}	PARJ(81)	0.247-0.347	0.297	±0.005	$^{+0.012}_{-0.007}$
	Q_0	PARJ(82)	0.84 - 1.84	1.34	±0.08	$^{+0.15}_{-0.09}$
	a	PARJ(41)	0.309 - 0.609	0.409	±0.020	$^{+0.009}_{-0.013}$
	σ_t	PARJ(21)	0.361 - 0.441	0.401	±0.006	$^{+0.003}_{-0.013}$

Table 6.7: *Parameter settings, range of parameter variation and parameter errors as in [14] for JETSET 7.3 PS with DELPHI decays. The parameters a, σ_t and γ_s are also de£ned in section 1.5.*

nominal value and the two extreme values of the range given in Table 6.7. The coef£cients $a^{(1,2)}$ are determined by £tting equation (6.8) to the set of the m values of $\Delta A^0_{s\bar{s}}$.

It is found that the parameters describing the fragmentation process of light quarks (u, d, s) can be divided in two groups. The £rst group includes the parameters that are related to primary quark fragmentation, the second one includes parameters related to the fragmentation in general (perturbative and non-perturbative QCD processes). The most important parameters for kaon production in the £rst group are the s-quark suppression factor (γ_s) and the probability that a strange meson will have spin 1, $P(^1P_0)_s$. In the second group the most important are $\Lambda_{\rm QCD}$ and Q_0 (cut off of gluon/quark virtualities in the perturbative QCD process). The uncertainties on parameters of the last group give a negligible contribution to the systematic error because the extra kaons created due to changes in these parameters carry no information about the charge of the primary quark independently of the ¤avour. The corresponding changes in $A^0_{s\bar{s}}$ are less than 10^{-4}. The second parameter from the £rst group, the probability that a strange meson will have spin 1, gives a shift in the momentum spectrum of kaons which is approximately the same for all light quarks. The contribution to $\delta A^0_{s\bar{s}}$ is about 0.0002.

Since the most important contribution to the systematic error comes from γ_s, the s suppression factor, several data sets were generated with values of γ_s ranging from 0.257 till 0.357. The effect on the asymmetry can be parametrised as

$$\Delta A^0_{s\bar{s}} \equiv A^0_{s\bar{s}}(\gamma_s = 0.307 + \Delta\gamma_s) - A^0_{s\bar{s}}(\gamma_s = 0.307) = 0.17\,\Delta\gamma_s\,.$$

In the DELPHI JETSET 7.3 simulation a nominal value of $\gamma_s = 0.307$ was used. This value was obtained by a tuning procedure described in reference [14], giving γ_s = 0.307 $\pm$ 0.007 (stat) $^{+0.002}_{-0.017}$ (syst). In the tuning procedure inconsistent $\mathrm{K}^{\pm}$ and K^0 data were used, which resulted in an asymmetric error on γ_s. Redoing the tuning of JETSET using more recent data [27] and replacing the inconsistent kaon data gives γ_s = 0.285 [34], consistent with results obtained by the ALEPH collaboration [31]. The systematic error on γ_s is taken as half the difference between the values 0.307 and 0.285. The error on the ALEPH result for γ_s is consistent with this.

The variation of the fragmentation parameters listed in Table 6.7 leads to a change in the $\mathrm{K}^{\pm}/\pi^{\pm}$ ratio, which is related to the kaon purity. The variation of the $\mathrm{K}^{\pm}/\pi^{\pm}$ ratio is at most 5%, which gives a systematic error on the s quark pole asymmetry of 0.0008.

Thus the combined error on the s quark pole asymmetry from light quark fragmentation is 0.0024. This error happens to be the same for the barrel and forward analyses.

6.4.3 Systematic error due to uncertainties in the heavy quark rejection

Heavy quark rejection in the barrel region also contributes to the uncertainties in $A^0_{s\bar{s}}$. Because of secondary vertices from, for example, photon conversion, and $\mathrm{K}^0_{\mathrm{S}}$ and hyperon decays P^+_N (see section 4.3) is peaked towards lower values. The rate of photon conversion is allowed to vary by $\pm 30\%$ and that of $\mathrm{K}^0_{\mathrm{S}}$ and Λ decays by $\pm 10\%$ in the simulation. The simulated events are re-weighted according to these uncertainties in photon conversion, $\mathrm{K}^0_{\mathrm{S}}$ and Λ rates. From the resulting changes in the coef£cients α_q and c_q the contribution to $\delta A^0_{s\bar{s}}$ is determined.

Another source of errors is gluon splitting. This results in pairs of c and b quarks in the fragmentation process. The gluon splitting rate $\mathrm{g} \to \mathrm{c\bar{c}}$ and $\mathrm{g} \to \mathrm{b\bar{b}}$ are measured to be $(2.38 \pm 0.48)\%$ [35] and $(0.33 \pm 0.13)\%$ [36], respectively. The $\mathrm{g} \to \mathrm{c\bar{c}}$ and $\mathrm{g} \to \mathrm{b\bar{b}}$ rates are conservatively varied by $\pm 50\%$ in order to evaluate the effects on $A^0_{s\bar{s}}$. Also, the uncertainty in the lifetimes of b and c hadrons can change the fraction of rejected b and/or c events.

The simulation may not reproduce correctly the observed resolution on the impact parameter. As a result also the distribution of the probability P^+_N is different in the simulated data from that in the real data. To estimate the contribution to the systematic error on the asymmetry we are £rst computing a probability P^-_N for tracks with negative impact parameters in the sample which has been selected by a cut $P^+_N > 0.15$. In this sample of events the contribution of heavy ¤avours and secondary decay vertices to P^-_N is highly suppressed as described in section 4.3. The difference between the selection ef£ciencies using the cut $P^-_N > 0.15$ for real and simulated data is determined. This difference is used to estimate the uncertainty on α_q and subsequently to $A^0_{s\bar{s}}$.

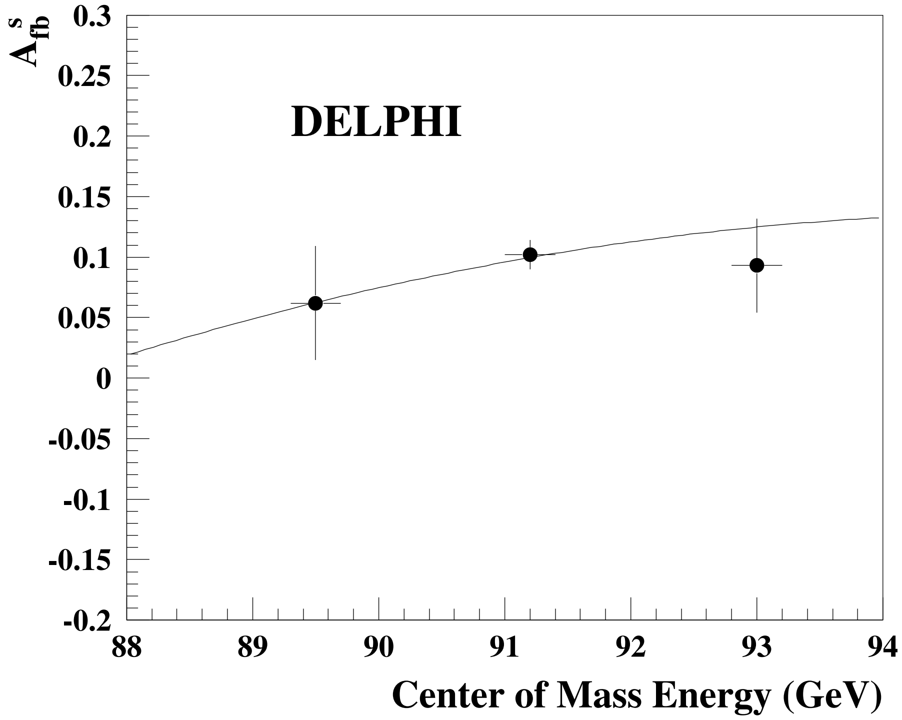

Figure 6.3: *The s quark forward-backward asymmetry as a function of the centre-of-mass energy. The points correspond to the data, the curve to the Standard Model expectation (ZFITTER: $M_Z = 91.1866$ GeV/c^2, $m_t = 173$ GeV/c^2, $m_H = 115$ GeV/c^2)*

6.4.4 Total systematic error

Summing all contributions discussed above, the total systematic error on the s quark pole asymmetry, $A^0_{s\bar{s}}$, is 0.0034 for the barrel region and 0.0068 for the forward region. The systematic errors on the forward-backward asymmetry for the points on and off the Z^0 peak are the same.

6.5 Combined results

The combined results of the barrel and forward analyses for A^s_{FB} are shown in Figure 6.3 and listed in Table 6.8. Correlations between the errors for the barrel and forward regions are taken into account. They are compared with the Standard Model prediction.

The s asymmetry at a centre-of-mass energy of 91.2 GeV as a function of the polar angle

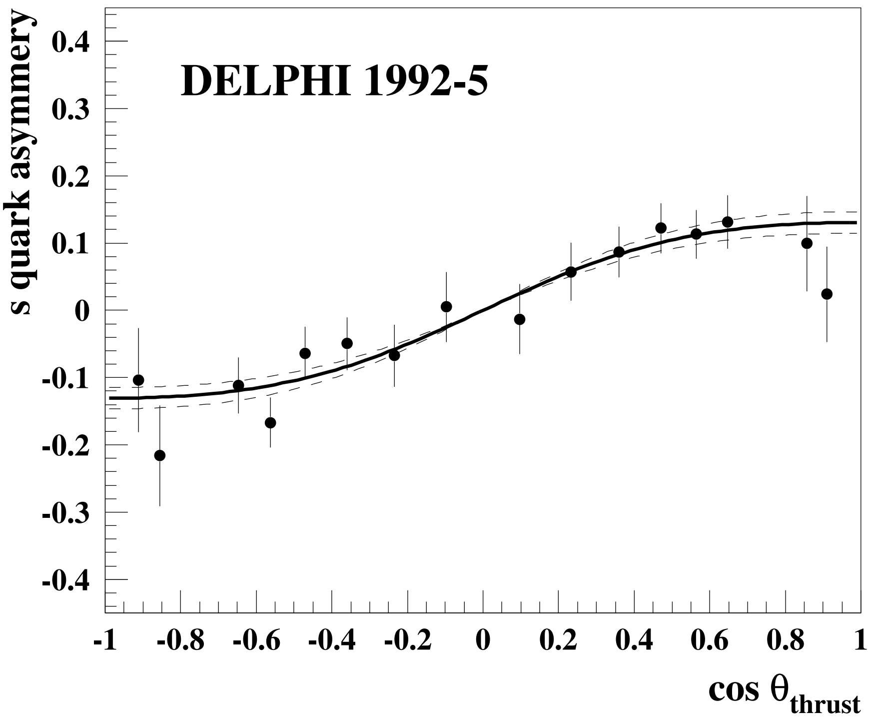

Figure 6.4: *The s quark asymmetry as a function of $\cos\theta_{thrust}$. The data points are the values computed in bins of $\cos\theta_{thrust}$ for the asymmetry between s and $\bar{s}$ quarks. The errors are statistical only. The superimposed curve represents the result on A^s_{FB} at 91.2 GeV listed in Table 6.8. The dashed curves correspond to the one standard deviation from this value.*

is shown in Figure 6.4.

Fixing $A^0_{d\bar{d}}, A^0_{u\bar{u}}$ to the Standard Model values of 0.1031 and 0.0736 respectively and $A^0_{b\bar{b}}$ and $A^0_{c\bar{c}}$ to the measured values, gives for the s quark pole asymmetry: $A^0_{s\bar{s}} = 0.1008 \pm 0.0113\,(\text{stat.}) \pm 0.0040\,(\text{syst.})$. The s quark pole asymmetry as a function of the up and down quark asymmetries can be written as

$$\begin{aligned} A^0_{s\bar{s}} &= 0.1008 \pm 0.0113\,(\text{stat.}) \pm 0.0040\,(\text{syst.}) \\ &+0.0121\frac{A^0_{d\bar{d}} - 0.1031}{0.1031} + 0.0115\frac{A^0_{u\bar{u}} - 0.0736}{0.0736} \end{aligned} \tag{6.9}$$

To determine the effective electroweak-mixing angle $\sin^2\theta^{lept}_{eff}$ de£ned in section 1.4.1, the experimental result given in equation (6.9) is used as the observable. The asymmetries $A^0_{s\bar{s}}$, $A^0_{d\bar{d}}$ and $A^0_{u\bar{u}}$ are expressed in terms of $\sin^2\theta^{lept}_{eff}$ using Equations (1.23) and (1.24). The

$\sqrt{s}$ (GeV)	89.5	91.2	93.0
A_{FB}^{s}	0.060 ± 0.047	0.098 ± 0.012	0.090 ± 0.039

Table 6.8: *Summary of A_{FB}^{s} values obtained from the 1992-1995 data. The quoted errors combine statistical and systematic errors.*

effective electroweak-mixing angle is determined in this way to be :

$$\sin^2 \theta_{eff}^{lept} = 0.2321 \pm 0.0029 \tag{6.10}$$

To determine the parity violating coupling of the s quark to the Z^0 (A_s), we use the expression for the pole asymmetry obtained in section 1.4.1 (see equation (1.23)):

$$A_{s\bar{s}}^{0} = \frac{3}{4} A_s A_e \ .$$

Taking for $A_{s\bar{s}}^{0}$ the value obtained by assuming the values for the up and down quark asymmetries from the Standard Model and using for A_e the measured value of 0.1479 ± 0.0051 [30], the coupling is determined to be :

$$A_s = 0.909 \pm 0.102\,(\text{stat.}) \pm 0.036(\text{syst.}). \tag{6.11}$$

Chapter 7

Conclusions and Interpretation

Charged kaons with a momentum between 10 and 24 GeV/c are identi£ed on a track-by-track basis using the ring imaging Cherenkov detectors of DELPHI—the Barrel and Forward RICH. A total of 3.2 M hadronic events were selected, from which 99402 events had at least one kaon within this energy range. These kaons are used to obtain an enriched sample of strange quark Z^0 decays. Information from the silicon micro-strip vertex detector (VD) was used to reject heavy quark events in the barrel region. The events with a high-energy kaon are used to determine the charged kaon asymmetry in the barrel and forward regions at the Z^0 peak:

$$\begin{aligned} A_{FB}^{K}(\text{barrel}) &= 0.0405 \pm 0.0049\,(\text{stat.}) \pm 0.0005\,(\text{syst.}) \\ A_{FB}^{K}(\text{forward}) &= 0.0390 \pm 0.0090\,(\text{stat.}) \pm 0.0009\,(\text{syst.}) \end{aligned}$$

Although the statistics for the forward analysis is 5.4 times smaller than that for the barrel analysis (see Table 5.3), the forward measurement for A_{FB}^{K} has only a factor 1.84 times larger error than that of the barrel one in contrast to the factor 2.3 expected from statistics. This is because the sensitivity to the asymmetry measurement is higher in the forward region than that in the barrel one.

The A_{FB}^{K} measurements are used to extract the strange quark asymmetry for the Barrel and Forward regions. For the simulation of the fragmentation of quarks JETSET 7.3 was used, tuned to LEP data. The systematic error is estimated including contributions from the uncertainties on the tuned JETSET parameters. The asymmetry measurements in the barrel and forward regions are combined taking into account their correlated systematic errors to obtain the s quark asymmetry. It was found that the dominant systematic error in the barrel analysis comes from the uncertainty in the modelling of the fragmentation of light quarks, while in the forward analysis it comes from the uncertainty in kaon production in heavy quark decays. The total systematic error in the barrel and forward analyses is 0.0034 and 0.0068 respectively. The total error on the s quark asymmetry is still dominated by the statistical error, which is three times larger than the systematic one.

The s quark forward-backward asymmetry, A_{FB}^{s}, measured at three centre-of-mass energies combining statistical and systematic errors is :

$$A^s_{FB}(\sqrt{s} = 89.5\text{GeV}) = 0.060 \pm 0.047$$
$$A^s_{FB}(\sqrt{s} = 91.2\text{GeV}) = 0.098 \pm 0.012$$
$$A^s_{FB}(\sqrt{s} = 93.0\text{GeV}) = 0.090 \pm 0.039$$

The asymmetry A^s_{FB} at 91.2 GeV close to the pole energy $\sqrt{s} = m_Z$ is used to extract the strange quark pole asymmetry. It is found to be :

$$A^0_{s\bar{s}} \quad = \quad 0.1008 \pm 0.0113\,(\text{stat.}) \pm 0.0040\,(\text{syst.})$$

The s quark pole asymmetry as a function of the up and down quark asymmetries is :

$$A^0_{s\bar{s}} = 0.1008 \pm 0.0113\,(\text{stat.}) \pm 0.0040\,(\text{syst.})$$
$$+0.0121\frac{A^0_{d\bar{d}} - 0.1031}{0.1031} + 0.0115\frac{A^0_{u\bar{u}} - 0.0736}{0.0736}$$

The s quark pole asymmetry can be compared to the pole asymmetry for the b quark measured by the four LEP collaborations [30] :

$$A^0_{b\bar{b}} = 0.0990 \pm 0.0021.$$

The Standard Model predicts the same asymmetries (see section 1.3) for strange and bottom quarks as they are both down-type quarks. This measurement is compatible with the hypothesis of the ¤avour independence of the asymmetry for bottom and strange quarks.

The result on the s quark asymmetry is the most precise measurement of the s quark asymmetry and is compatible with the previous result measured by the DELPHI collaboration [37]

$$A^0_{s\bar{s}} = 0.131 \pm 0.035\,(\text{stat.}) \pm 0.013\,(\text{syst.})$$

which is based on the statistics collected during 1992. It is also compatible with the s quark forward-backward asymmetry measured by the OPAL collaboration:

$$A^0_{s\bar{s}(d\bar{d})} = 0.068 \pm 0.035\,(\text{stat.}) \pm 0.011\,(\text{syst.})$$

The latter result is based on 4.3 M hadronic events collected between 1990 and 1995. In our analysis the statistical and systematic errors are both smaller than those of the "model-independent" analysis from OPAL [38]. A preliminary result for the parity violating coupling of the s quark to the Z^0, A_s, has been presented at the HEP-99 (Tampere, Finland) conference by the SLD collaboration. The coupling A_s in this experiment is obtained from a measurement of the left-right-forward-backward production asymmetry in polar angle of the tagged s quark, as the SLC (Stanford Linear Collider) has polarised electron and positron beams. Since this result is a preliminary one and its statistical and systematic errors are still under study, a comparison with our data is premature.

The measured s quark forward-backward asymmetries at different centre-of-mass energies agree with the Standard Model expectations. The change in the asymmetry near the Z^0 peak is proportional to the axial-vector coupling a_s (1.18). The $\mathrm{d}A^s_{FB}/\mathrm{d}(\sqrt{s})$ is measured to be 0.006 ± 0.017 GeV^{-1}, which is compatible with the Standard Model value of 0.0184 GeV^{-1} as calculated by ZFITTER. Assuming the absolute values of the axial-vector (a_s) and vector (v_s) couplings of s quark to be as predicted by the Standard Model, the flipping of the sign of a_s is excluded at 90% CL.

The result for the effective electroweak-mixing angle of

$$\sin^2\theta^{lept}_{eff} = 0.2321 \pm 0.0029$$

contributes to the world average value of

$$\sin^2\theta^{lept}_{eff} = 0.23157 \pm 0.00018$$

which has been determined from various asymmetries measured at LEP and SLD [30]. This angle is a very important parameter of the Standard Model as it sets, in combination with other electroweak observables, a constraint on the Higgs mass m_H, see reference [30].

The parity violating coupling of the s quark to the Z^0 is determined to be :

$$A_s = 0.909 \pm 0.102\,(\text{stat.}) \pm 0.036(\text{syst.}).$$

It agrees well with the Standard Model expectation of 0.935. This is the most precise measurement of this quantity.

The results presented in this thesis are published in reference [39].

Appendix A

Relation between A_i^{mat} and α_{K^+}

De£ne N^+ (N^-) as the number of K^+ (K^-) produced inside the beam pipe and n^+ (n^-) as the number of K^+ (K^-) that reach the tracking detector positioned behind the RICHs—the OD in the barrel region and the FCB in the forward region. The relations between n^+ (n^-) and N^+ (N^-) will be

$$\begin{aligned} n^+ &= N^+ \cdot \exp(-\frac{\sigma_+ l}{L}) \cdot \exp(-\frac{l}{\gamma c \tau}) \\ n^- &= N^- \cdot \exp(-\frac{\sigma_- l}{L}) \cdot \exp(-\frac{l}{\gamma c \tau}) \end{aligned} \tag{A.1}$$

where L is the amount of the material in front of the OD or the FCB; l is the kaon track length averaged over the kaon momenta; σ_+ (σ_-) is the cross-section with the detector material of K^+ (K^-), which is averaged over the kaon momenta and over the material in front of OD or FCB. c is the speed of light in vacuum, τ is the lifetime of the charged kaon and $\gamma = 1/\sqrt{1 - v^2/c^2}$ is averaged over the kaon momenta. Then the probabilities for K^+ and K^- to reach the OD and the FCB are

$$\begin{aligned} \epsilon_{\mathrm{K}^+} = \frac{n^+}{N^+} &= \exp(-\frac{\sigma_+ l}{L}) \cdot \exp(-\frac{l}{\gamma c \tau}) \\ \epsilon_{\mathrm{K}^-} = \frac{n^-}{N^-} &= \exp(-\frac{\sigma_- l}{L}) \cdot \exp(-\frac{l}{\gamma c \tau}) \end{aligned} \tag{A.2}$$

and the ratio of these probabilities is

$$r = \frac{\epsilon_{\mathrm{K}^-}}{\epsilon_{\mathrm{K}^+}} = \exp\left(-\frac{l}{L}(\sigma_- - \sigma_+)\right) \tag{A.3}$$

Furthermore

$$
\begin{aligned}
1 - r &= 1 - \left(\exp(-\frac{l\sigma_+}{L})\right)^{\frac{\Delta\sigma}{\sigma_+}} \\
&= 1 - \left(\frac{n_+}{N_+} \cdot \exp(\frac{l}{\gamma c\tau})\right)^{\frac{\Delta\sigma}{\sigma_+}} \\
&= 1 - (1 - \alpha_{K^+})^{\varepsilon_+}
\end{aligned}
\tag{A.4}
$$

with

$$
\varepsilon_+ = \frac{\Delta\sigma}{\sigma_+} = \frac{\sigma_- - \sigma_+}{\sigma_+}\ ; \qquad \alpha_{K^+} = 1 - \frac{n_+}{N_+} \cdot \exp(\frac{l}{\gamma c\tau})
$$

α_{K^+} is the fraction of positively charged kaons stopped only by interaction with detector material in front of the OD or the FCB; ε_+ is the relative difference of the K^- and K^+ cross-sections. The £nal relation is

$$
\boxed{2A_i^{mat} = 1 - r_i \quad = \quad 1 - (1 - \alpha_{K^+})^{\varepsilon_+}}
\tag{A.5}
$$

Appendix B

Conjugate Directions Method

In this appendix we describe the Manevich's conjugate direction method. This algorithm is found to be the most powerful among the various methods for unconstrained (quadratic and non-quadratic) function minimization. The method is elegant as it does not require extensive knowledge of higher mathematics to derive it. This is shown below.

B.1 Single variable quadratic function

Consider a quadratic function of a single variable: $f(x) = c + bx + \frac{1}{2}Ax^2$. For any two points, x_1 and x_2, the following expression is valid:

$$f'(x_2) - f'(x_1) = A(x_2 - x_1) \tag{B.1}$$

where $f'(x_i), i = 1, 2$ is the derivative of $f(x)$ at $x = x_i, i = 1, 2$.
For three points x_1, x_2, x_m one has:

$$\left\{ \begin{array}{l} f'(x_2) - f'(x_1) = A(x_2 - x_1) \\ f'(x_2) - f'(x_m) = A(x_2 - x_m) \end{array} \right.$$

If x_m is the point where the function has its minimum, then $f'(x_m) = 0$ and the point can be found as follows:

$$\begin{aligned} x_m &= x_2 - (x_2 - x_1)\frac{f'(x_2)}{f'(x_2) - f'(x_1)} \\ &= x_1 + \underbrace{(x_2 - x_1)}_{h_1} + \underbrace{(x_1 - x_2)\frac{f'(x_2)}{f'(x_2) - f'(x_1)}}_{h_2} \end{aligned} \tag{B.2}$$

One can see that the minimum of a single variable quadratic function can be found after two steps: the £rst step is an arbitrary non-zero step ($\forall h_1 \neq 0$), the second step h_2 is de£ned by formula (B.2).

B.2 N-variable quadratic function and conjugate directions

Consider a quadratic function of N variables

$$f(\vec{x}) = c + (\vec{b}, \vec{x}) + \frac{1}{2}(\vec{x}, \mathbf{A}\vec{x}) \,, \tag{B.3}$$

where $\vec{x}$ is the vector of function variables and $\mathbf{A}$ is the positive-de£nite matrix. The equivalent expression to (B.1) for the N-variable quadratic function will be:

$$\vec{f'}(\vec{x}_2) - \vec{f'}(\vec{x}_1) = \mathbf{A}(\vec{x}_2 - \vec{x}_1) \tag{B.4}$$

where $\vec{f'}(\vec{x}_i)$ is the gradient of the function at the point $\vec{x}_i$.

Conjugate vectors

The set of vectors $\{\vec{p}_i\}_{i=1,N}$ is called a conjugate vector set, if the vectors are conjugate with respect to the matrix $\mathbf{A}$, i.e. for any pair of the vectors the following relation is valid:

$$\{(\vec{p}_i, \mathbf{A}\vec{p}_j) = 0\} \qquad i \neq j,\ i,j = 1,\ldots,N \tag{B.5}$$

Any vector $\vec{x}$ can be represented as $\vec{x} = \sum_{i=1}^{N} \xi_i \vec{p}_i$, and the function $f(\vec{x})$ reduces to a sum of independent single-variable quadratic functions that have to be minimised to obtain the minimum of $f(\vec{x})$:

$$\begin{aligned} f(\vec{x}) &= c + \sum_{i=1}^{N} (\vec{b}, \xi_i\vec{p}_i) + \frac{1}{2}\sum_{i,j=1}^{N} (\xi_i\vec{p}_i, \mathbf{A}\xi_j\vec{p}_j) \\ &= c + \sum_{i=1}^{N} \xi_i(\vec{b}, \vec{p}_i) + \frac{1}{2}\sum_{i,j=1}^{N} \xi_i\xi_j(\vec{p}_i, \mathbf{A}\vec{p}_j) \\ &= c + \sum_{i=1}^{N} \xi_i(\vec{b}, \vec{p}_i) + \frac{1}{2}\sum_{i=1}^{N} \xi_i^2(\vec{p}_i, \mathbf{A}\vec{p}_i) \\ &= c + \sum_{i=1}^{N} g_i(\xi_i) \end{aligned}$$

where $g_i(\xi_i) = \xi_i(\vec{b}, \vec{p}_i) + \frac{1}{2}\xi_i^2(\vec{p}_i, \mathbf{A}\vec{p}_i)$ are single variable functions.

The function minimization when the set $\{\vec{p}_i\}_{i=1,N}$ is known

If the set of conjugate vectors $\{\vec{p}_i\}_{i=1,N}$ is known then the function minimum can be found after two steps. To demonstrate this, we write the equivalent of formula (B.2) :

$$\vec{x}_m = \vec{x}_1 + \underbrace{(\vec{x}_2 - \vec{x}_1)}_{\vec{h}_1} + \underbrace{\sum_{i=1}^{N} \frac{(\vec{x}_1 - \vec{x}_2, \vec{p}_i)}{\|\vec{p}_i\|} \frac{(\vec{f}'(\vec{x}_2), \vec{p}_i)}{(\vec{f}'(\vec{x}_2) - \vec{f}'(\vec{x}_1), \vec{p}_i)} \frac{\vec{p}_i}{\|\vec{p}_i\|}}_{\vec{h}_2} \tag{B.6}$$

which was obtained by using the following equivalences in the expression of $\vec{h}_2$ (compare (B.2) and (B.6)):

$$\begin{aligned} x_1 - x_2 \quad &\longrightarrow \quad \frac{(\vec{x}_1 - \vec{x}_2, \vec{p}_i)}{\|\vec{p}_i\|} \\ \frac{f'(x_2)}{f'(x_2) - f'(x_1)} \quad &\longrightarrow \quad \frac{(\vec{f}'(\vec{x}_2), \vec{p}_i)}{(\vec{f}'(\vec{x}_2) - \vec{f}'(\vec{x}_1), \vec{p}_i)} \end{aligned}$$

One can see that after the £rst step that has non-zero projections on each conjugate vector ($\frac{(\vec{x}_1 - \vec{x}_2, \vec{p}_i)}{\|\vec{p}_i\|} \neq 0, i = 1, \ldots, N$), the second step $\vec{h}_2$ gives the function minimum.

De£ne

$$\begin{aligned} f'_{p_i}(\vec{x}) &= (\vec{f}'(\vec{x}), \vec{p}_i) \\ \alpha_i^{(2)} &= \frac{(\vec{x}_1 - \vec{x}_2, \vec{p}_i)}{\|\vec{p}_i\|} \frac{(\vec{f}'(\vec{x}_2), \vec{p}_i)}{(\vec{f}'(\vec{x}_2) - \vec{f}'(\vec{x}_1), \vec{p}_i)} \end{aligned}$$

then Formula (B.6) can be rewritten as

$$\vec{x}_m = \vec{x}_1 + (\vec{x}_2 - \vec{x}_1) + \sum_{i=1}^{N} \alpha_i^{(2)} \frac{\vec{p}_i}{\|\vec{p}_i\|} \tag{B.7}$$

B.3 Algorithm description

Take some particular point $\mathbf{P}$ as the origin of the coordinate system with coordinates $\vec{x} = (x_1, \ldots, x_N)$. Then any function $f(\vec{x})$ can be approximated by its Taylor series

$$\begin{aligned} f(\vec{x}) &= f(\mathbf{P}) + \sum_i \frac{\partial f}{\partial x_i} x_i + \frac{1}{2} \sum_{ij} \frac{\partial^2 f}{\partial x_i \partial x_j} x_i x_j + \cdots \\ &\simeq c + (\vec{b}, \vec{x}) + \frac{1}{2}(\vec{x}, \mathbf{A}\vec{x}) \end{aligned} \tag{B.8}$$

where

$$c \equiv f(\mathbf{P}) \qquad \vec{b} \equiv \vec{f}'(\mathbf{P}) \qquad [\mathbf{A}]_{ij} \equiv \frac{\partial^2 f}{\partial x_i \partial x_j}(\mathbf{P})$$

The matrix $\mathbf{A}$ whose components are the second partial derivative matrix of the function is called *Hesse matrix* of the function at $\mathbf{P}$.

First N+1 steps

Assume that the conjugate vector set, $\{\vec{p}_i\}_{i=1,N}$, for the matrix $\mathbf{A}$ is known, but we will collect only one vector per step: one adds one new vector to the set of the conjugate vectors collected on preceding steps, performs a step, and then repeats the procedure.

Then, our steps are:

Step 1

We have $\vec{x}_1$ as a start point, $\vec{f}'(\vec{x}_1)$ as the gradient at this point, and take the £rst vector $\vec{p}_1$. The step is

$$\vec{x}_2 = \vec{x}_1 + \underbrace{h_1 \frac{\vec{p}_1}{\|\vec{p}_1\|}}_{\vec{h}_1}$$

where $\forall h_1 \neq 0$.

Step 2

We calculate $\vec{f}'(\vec{x}_2)$, and take the next vector $\vec{p}_2$. The step is

$$\begin{aligned} \vec{x}_3 &= \underbrace{\vec{x}_1 + \vec{h}_1}_{\vec{x}_2} + \vec{h}_2 \\ \vec{h}_2 &= \frac{(\vec{x}_1 - \vec{x}_2, \vec{p}_1)}{\|\vec{p}_1\|} \frac{f'_{p_1}(\vec{x}_2)}{f'_{p_1}(\vec{x}_2) - f'_{p_1}(\vec{x}_1)} \frac{\vec{p}_1}{\|\vec{p}_1\|} + H_1^{(2)} \frac{\vec{p}_2}{\|\vec{p}_2\|} \end{aligned}$$

where $\forall H_1^{(2)} \neq 0$. In the case of a quadratic function and in absence of computer rounding errors, the component of this step along the direction $\vec{p}_1$ leads to the function minimum along this direction. If rounding errors are present then that minimum will be approximate.

Step 3

We calculate $\vec{f'}(\vec{x}_3)$, and add the next vector $\vec{p}_3$. The step is

$$\begin{aligned}\vec{x}_4 &= \vec{x}_3 + \vec{h}_3 \\ \vec{h}_3 &= \sum_{i=1}^{2} \frac{(\vec{x}_2 - \vec{x}_3, \vec{p}_i)}{\|\vec{p}_i\|} \frac{f'_{p_i}(\vec{x}_3)}{f'_{p_i}(\vec{x}_3) - f'_{p_i}(\vec{x}_2)} \frac{\vec{p}_i}{\|\vec{p}_i\|} + H_2^{(3)} \frac{\vec{p}_3}{\|\vec{p}_3\|}\end{aligned}$$

where $\forall H_2^{(3)} \neq 0$. Again, in a case of the quadratic function and in the absence of rounding errors, the components of this step along the directions $\vec{p}_1$ and $\vec{p}_2$ lead to the function minima along these directions. If rounding errors are present then those minima will be approximate, but the minimum along $\vec{p}_1$ will also be improved.

Step k

We calculate $\vec{f'}(\vec{x}_k)$ and add the next vector $\vec{p}_k$. The step is

$$\boxed{\begin{aligned}\vec{x}_{k+1} &= \vec{x}_k + \vec{h}_k \\ \vec{h}_k &= \sum_{i=1}^{k-1} \frac{(\vec{x}_{k-1} - \vec{x}_k, \vec{p}_i)}{\|\vec{p}_i\|} \frac{f'_{p_i}(\vec{x}_k)}{f'_{p_i}(\vec{x}_k) - f'_{p_i}(\vec{x}_{k-1})} \frac{\vec{p}_i}{\|\vec{p}_i\|} + H_{k-1}^{(k)} \frac{\vec{p}_k}{\|\vec{p}_k\|} \\ &= \sum_{i=1}^{k-1} \alpha_i^{(k)} \frac{\vec{p}_i}{\|\vec{p}_i\|} + H_{k-1}^{(k)} \frac{\vec{p}_k}{\|\vec{p}_k\|}\end{aligned}} \qquad \text{(B.9)}$$

where $\forall H_{k-1}^{(k)} \neq 0$. The $\alpha_i^{(k)}$ $(i = 1, \ldots, k-1)$ represent the projections on the conjugate vectors $\vec{p}_i$ $(i = 1, \ldots, k-1)$ of the step from the point $\vec{x}_k$; each of these projections leads to the minimum along the corresponding direction in case of the quadratic function without rounding errors. In the case of rounding errors, the function minima along the vectors $\vec{p}_i$ $(i = 1, \ldots, k-2)$ will be improved.

Step $N+1$

We calculate $\vec{f'}(\vec{x}_{N+1})$, and the last conjugate vector has been collected on the preceding step. The last step for quadratic function will be:

$$\begin{aligned}\vec{x}_{N+2} &= \vec{x}_{N+1} + \vec{h}_{N+1} \\ \vec{h}_{N+1} &= \sum_{i=1}^{N} \frac{(\vec{x}_N - \vec{x}_{N+1}, \vec{p}_i)}{\|\vec{p}_i\|} \frac{f'_{p_i}(\vec{x}_{N+1})}{f'_{p_i}(\vec{x}_{N+1}) - f'_{p_i}(\vec{x}_N)} \frac{\vec{p}_i}{\|\vec{p}_i\|}\end{aligned}$$

Note, that there are no arbitrary projections along any conjugate vector; the point $\vec{x}_{N+2}$ is the minimum of the quadratic function (e.g., if the function f in (B.8) would be quadratic),

$\vec{x}_{N+2} \equiv \vec{x}_m$. One can easily see that we do not need the line minimization, which is required in the Fletcher-Reeves conjugate gradient method [40]. This became possible because we will construct the set of required conjugate vectors without any reference to whether the function minima are reached along the searched vectors.

Construction of the conjugate vector set

Consider the point $\vec{x}_k$ that was reached after $k-1$ steps and assume that on those steps we were able to calculate one conjugate vector per step. We made the steps using the above procedure. Thus we have the vectors $\{\vec{p}_i\}_{i=1,k-1}$, and we are going to determine the next one—$\vec{p}_k$. The vector $\vec{p}_k$ is found as a linear combination of the known vectors and the gradient at the current point $\vec{x}_k$:

$$\boxed{\vec{p}_k = -\vec{f}'(\vec{x}_k) + \sum_{i=1}^{k-1} \beta_i^{(k)} \vec{p}_i} \tag{B.10}$$

The relations $\{(\vec{p}_k, \mathbf{A}\vec{p}_i) = 0\}_{i=1,\ldots,k-1}$ should be valid. Substituting $\vec{p}_k$ by (B.10) in these relations:

$$0 = (\vec{p}_k, \mathbf{A}\vec{p}_i) = (-\vec{f}'(\vec{x}_k) + \sum_{i=1}^{k-1} \beta_i^{(k)} \vec{p}_i, \mathbf{A}\vec{p}_i)$$

and using the fact that the vectors are mutually conjugate, $\{(\vec{p}_j, \mathbf{A}\vec{p}_i) = 0\}_{i \neq j;\, i,j=1,\ldots,k-1}$, we obtain the expressions:

$$(\vec{f}'(\vec{x}_k), \mathbf{A}\vec{p}_i) = \beta_i^{(k)} (\vec{p}_i, \mathbf{A}\vec{p}_i)$$

which gives the $\beta_i^{(k)}$ coef£cients for Formula (B.10):

$$\boxed{\beta_i^{(k)} = \frac{(\vec{f}'(\vec{x}_k), \mathbf{A}\vec{p}_i)}{(\vec{p}_i, \mathbf{A}\vec{p}_i)}\;; \qquad i = 1, \ldots, k-1} \tag{B.11}$$

What do the $\{\mathbf{A}\vec{p}_i\}_{i=1,\ldots,k-1}$ equal to? To answer this question, consider Formula (B.4) for the current and preceding points, x_k and x_{k-1}:

$$\vec{f}'(\vec{x}_k) - \vec{f}'(\vec{x}_{k-1}) = \mathbf{A}(\vec{x}_k - \vec{x}_{k-1}) \tag{B.12}$$

Remember that the preceding step is:

$$
\begin{aligned}
\vec{x}_k - \vec{x}_{k-1} &= \vec{h}_{k-1} \\
&= \sum_{i=1}^{k-2} \frac{(\vec{x}_{k-2} - \vec{x}_{k-1}, \vec{p}_i)}{\|\vec{p}_i\|} \frac{f'_{p_i}(\vec{x}_{k-1})}{f'_{p_i}(\vec{x}_{k-1}) - f'_{p_i}(\vec{x}_{k-2})} \frac{\vec{p}_i}{\|\vec{p}_i\|} \\
&+ H_{k-2}^{(k-1)} \frac{\vec{p}_{k-1}}{\|\vec{p}_{k-1}\|} \\
&= \sum_{i=1}^{k-2} \alpha_i^{(k-1)} \frac{\vec{p}_i}{\|\vec{p}_i\|} + H_{k-2}^{(k-1)} \frac{\vec{p}_{k-1}}{\|\vec{p}_{k-1}\|}
\end{aligned} \tag{B.13}
$$

After substitution of this step for $(\vec{x}_k - \vec{x}_{k-1})$ in (B.12), we obtain the vector $\mathbf{A}\vec{p}_{k-1}$:

$$
\vec{f}'(\vec{x}_k) - \vec{f}'(\vec{x}_{k-1}) = \mathbf{A}(\sum_{i=1}^{k-2} \alpha_i^{(k-1)} \frac{\vec{p}_i}{\|\vec{p}_i\|} + H_{k-2}^{(k-1)} \frac{\vec{p}_{k-1}}{\|\vec{p}_{k-1}\|})
$$

thus

$$
\boxed{\mathbf{A}\vec{p}_{k-1} = \frac{\|\vec{p}_{k-1}\|}{H_{k-2}^{(k-1)}} (\vec{f}'(\vec{x}_k) - \vec{f}'(\vec{x}_{k-1}) - \sum_{i=1}^{k-2} \alpha_i^{(k-1)} \frac{\mathbf{A}\vec{p}_i}{\|\vec{p}_i\|})} \tag{B.14}
$$

On the k-th step, we calculate the vector $\mathbf{A}\vec{p}_{k-1}$ using the vectors $\{\mathbf{A}\vec{p}_i\}_{i=1,\ldots,k-2}$ that were found on the preceding steps. We use this vector to determine the coef£cients $\beta_i^{(k)}$ (see (B.11)), and, £nally, obtain the $\vec{p}_k$ conjugate vector by Formula (B.10). For the £rst step we take the anti-gradient (see Formula (B.10)) as the £rst conjugate vector; in general, the £rst vector can be taken arbitrarily. We now have a procedure that gives a new conjugate vector on every step, including the £rst one. After N steps, one can keep this set of vectors or update it by the procedure described in reference [41]. Note that the conjugate vector construction makes no use of the line minimization, while the conjugate gradient method [40] requires this.

Finally, we derive a special form of $\alpha_i^{(k)}$ (see Formula (B.9)). This form helps to understand the chosen steps' components along the conjugate vectors and is very practical for programming this algorithm into computer codes.

B.4 Practical representation of $\alpha_i^{(k)}$

Introduce $C_i^{(k)}$ as

$$\alpha_i^{(k)} = -C_i^{(k)} f'_{p_i}(\vec{x}_k) \tag{B.15}$$

then

$$C_i^{(k)} = \frac{(\vec{x}_k - \vec{x}_{k-1}, \vec{p}_i)}{\|\vec{p}_i\|} \frac{1}{f'_{p_i}(\vec{x}_k) - f'_{p_i}(\vec{x}_{k-1})}$$

But from (B.13):

$$\vec{x}_k - \vec{x}_{k-1} = \sum_{j=1}^{k-2} \underbrace{(-)C_j^{(k-1)} f'_{p_j}(\vec{x}_{k-1})}_{\alpha_j^{(k-1)}} \frac{\vec{p}_j}{\|\vec{p}_j\|} + H_{k-2}^{(k-1)} \frac{\vec{p}_{k-1}}{\|\vec{p}_{k-1}\|}$$

It gives:

$$\begin{aligned} C_i^{(k)} &= \frac{1}{\|\vec{p}_i\|(f'_{p_i}(\vec{x}_k) - f'_{p_i}(\vec{x}_{k-1}))} [(\sum_{j=1}^{k-2} (-)C_j^{(k-1)} f'_{p_j}(\vec{x}_{k-1}) \frac{\vec{p}_j}{\|\vec{p}_j\|}, \vec{p}_i) \\ &\quad + (H_{k-2}^{(k-1)} \frac{\vec{p}_{k-1}}{\|\vec{p}_{k-1}\|}, \vec{p}_i)] \; ; \quad i = 1, \ldots, k-1 \end{aligned}$$

We then £nd that the coef£cients $C_i^{(k)}$ from the current step can be derived from those of the preceding step using the gradients at the current and preceding points:

$$\boxed{\begin{aligned} C_i^{(k)} &= C_i^{(k-1)} \frac{f'_{p_i}(\vec{x}_{k-1})}{f'_{p_i}(\vec{x}_{k-1}) - f'_{p_i}(\vec{x}_k)} \; ; \quad i = 1, \ldots, k-2 \\ C_{k-1}^{(k)} &= (-)H_{k-2}^{(k-1)} \frac{1}{f'_{p_{k-1}}(\vec{x}_{k-1}) - f'_{p_{k-1}}(\vec{x}_k)} \end{aligned}} \tag{B.16}$$

B.5 Comments

There are four comments about the step's components along the conjugate vectors, which are important in the practical realization of this algorithm:

First, for the positive-de£nite matrix $\mathbf{A}$ (see (B.8)) the $-C_i^{(k)}$ represent the diagonal elements of the inverse Hesse matrix $\mathbf{A^{-1}}$ in the coordinate system with the conjugate vectors as the basis vectors. In this coordinate system the matrix is diagonal. It means that for the same conjugate vector, the $C_i^{(k)}$ do not change as the step number k runs, unless the function is non-quadratic: for a quadratic function the matrix $\mathbf{A}$ is a constant matrix. If the function is highly non-quadratic, then the coef£cients might change considerably, and the step's component $\alpha_i^{(k)}$ (along the corresponding vectors) must be constrained (see [41]) to keep the function inside the region where the quadratic approximation is valid.

Second, the above feature of the coef£cients $C_i^{(k)}$ makes that the $\alpha_i^{(k)}$ are the Newton's steps along the corresponding vectors $\vec{p}_i$. These step's components, which are independently controlled, look at minima along their directions and do not change the possible minima along the neighbouring vectors for the quadratic function. Since the step's components are independently controlled by (B.15)-(B.16), this is the way how it helps the rounding error problem.

Third, the proposed procedure of the conjugate vector construction makes no use of line minimization! This also helps the rounding error problem. Since the function minimization is performed in the increasing subspace of the known conjugate vectors (the subspace dimension increases as more vectors are found), we use the quadratic approximation of the function (B.8) only for this subspace unlike the variable metric methods (e.g. [42] or [43]) do. (The algorithm does not use the function second derivatives as well.) This enables us to make the optimal steps (in the context of the £rst two comments) and to use in the most effective way the available information about the function.

Finally, at the minimum the algorithm gives the sets of the conjugate vectors $\{\vec{p}_i\}_{i=1,\dots,N}$ and of the vectors to which they must be orthogonal $\{(\mathbf{A}\vec{p}_i)\}_{i=1,\dots,N}$! This allows us to calculate the covariant matrix $\mathbf{A^{-1}}$, which can be used in the error analysis of the obtained function parameters at the minimum.

B.6 Performance of the method for quadratic functions

We considered the following function of N variables (here the lower index is the number of the variable):

$$f(x_1,\dots,x_N)=\sum_{i=1}^{N}\frac{x_i^2}{2^{i-1}}+\sum_{i=1}^{N-1}\frac{x_i\;x_{i+1}}{2^i},$$

$$\text{with start point } x^{(0)}=(1,\dots,1) \quad \text{and minimum } f(0,\dots,0)=0$$

Results for various values of N obtained in our method and a comparison with those of the variable metric method (VMM) are given in Table B.1.

The convergence of our algorithm for quadratic functions turns out to be close to the theoretical limit—for functions of N variables minima were reached after $N+1$ steps with high accuracy (may be, plus 1 – 4 steps at large N exceeding approximately 40–60). To

	This method			VMM	
Number of variables	Number of steps	Number of funct.calls	Accuracy in F	Number of funct. calls	Accuracy in F
N=10	11	242	$0.2 * 10^{-25}$	448	10^{-25}
N=20	21	882	$0.2 * 10^{-27}$	975	10^{-22}
N=30	31	1922	$0.1 * 10^{-27}$	1658	$0.4 * 10^{-25}$
N=40	43	3526	$0.2 * 10^{-21}$	2383	$0.1 * 10^{-21}$

Table B.1: *Results for a quadratic function.*

compare this algorithm with that of VMM, the last one was required to reach approximately the same accuracy of the function at the minimum.

Both algorithms are very effective for quadratic functions. It is clear that the most ef£cient method for quadratic functions is Newton's method. As the VMM-algorithm (in the MINUIT package) calculates on the £rst iteration the Hesse matrix and then makes Newton steps, its ef£ciency is close to that of Newton's method. This conjugate direction method does not compare unfavourably with these methods. If we compare the total number of function calls of these two algorithms[1], then the VMM has some advantage over our algorithm only for $N > 25$; but still accuracy, as a rule, is higher in the proposed conjugate direction method.

B.7 Some history about gradient methods

First, there was the *Steepest descent method*. It starts at a point $\vec{x}_1$. As many times as needed, moves from the point $\vec{x}_k$ to the point $\vec{x}_{k+1}$ by minimising along the line from $\vec{x}_k$ in the direction of the local anti-gradient $-\vec{f'}(\vec{x}_k)$. Remember that the new gradient at the minimum point of any line minimization is perpendicular to the direction just traversed. This is expected to become a serious problem with minimising functions (even quadratic functions) with deep valleys.

Fletcher and *Reeves* [40] proposed not to move in the direction of the local anti-gradient, but rather in a direction that is somehow constructed to be *conjugate* to the preceding direction traversed; this way one saves the local minimum in that direction (as these two directions are conjugate). They also observed that the new conjugate vector could be found by conjugating this vector with the last found conjugate vector because the line minimization in the direction of that vector had been performed: At the point $\vec{x}_{k+1}$, any vector orthogonal to $\vec{f'}(\vec{x}_{k+1}) - \vec{f'}(\vec{x}_k)$ and the vector $\vec{x}_{k+1} - \vec{x}_k$ are conjugate in the case of a quadratic function f. It looks like one pass of N-line minimizations will result in the minimum of a N-variable quadratic function. This is the theory, but in practice, it won't be exactly at the minimum

[1]For calculations of derivatives of quadratic functions central differences were used; one call of the gradient is equivalent to $2N$ calls of the function.

because of rounding errors, so that repeated cycles of N line minimizations are required.

Manevich and *Polyanchikov* [44] went further using the following. First, for quadratic functions two steps in the direction of any conjugate vector are enough to reach the minimum along this vector; for non-quadratic functions these two steps can still have a considerable deviation from the minimum. Second, in contrast to quadratic functions, where each step in the direction of the conjugate vector up to the exact minimum lowers by one the space dimension in which the function should be minimised, this is not true any more for a non-quadratic function. Finally, the function variables are not absolutely independent, and the Fletcher-Reeves result that the new vector is automatically conjugate to all previous found vectors is not valid anymore. Hence, what is the point of spending time and efforts to £nd the linear minimum if we do not need it later? The answer is there is no point at all. The £rst idea is that the linear minimization should be cancelled. But one needs then a general procedure of conjugate vector construction that makes no use of line minimizations. This will be the second idea. At £rst glance this seems a bad idea, since nobody likes to solve the system of equations (B.5). Well, then we come up with the third idea! Let us allow each of our steps to have some projections on all conjugate vectors already found, and for example they improve the minima along the corresponding vectors, then we get the step (B.9) with the conjugate vector determination by Formulae (B.10),(B.11) and (B.14). This way the method has fewer calls to the function and is less sensitive to accumulation of rounding errors in the conjugate vectors set construction. And all what is said about it in section B.5 is valid.

In paper [41] we give further development of Manevich's algorithm for non-quadratic functions and show that it performs as good as the best variable metric methods and can even be applied, in special cases, to Monte Carlo type objective functions. We are able to extract the covariant matrix at the minimum and it is done without additional calls to the function (see section B.5), so that it is now possible to carry out the error analysis too. We think that the next step in this direction should be using the proposed algorithm as the basic optimiser in constrained optimization methods.

Bibliography

[1] S.L. Glashow, *"Partial-Symmetries of Weak Interactions"*, Nucl. Phys. **22** (1961) 579; A. Salam and J.C. Ward, *"Electromagnetic and Weak Interactions"*, Phys. Lett. **13** (1964) 168; S. Weinberg, *A Model of Leptons*, Phys. Rev. Lett. **19** (1967) 1264.

[2] P.W. Higgs, *"Broken symmetries, massless particles and gauge £elds"*, Phys. Rev. Lett. **12** (1964) 132; P.W. Higgs, *"Broken symmetries and the masses of gauge bosons"*, Phys. Rev. Lett. **13** (1964) 509.

[3] The LEP Collaborations, the LEP Electroweak Working Group and the SLD Heavy Flavour and Electroweak Groups, *"A Combination of Preliminary Electroweak Measurements and Constraints on the Standard Model"*, CERN-EP/2000-016 (2000).

[4] E. Fermi, Z. Phys. **88** (1934) 161.

[5] M. Consoli and W. Hollik, *Electroweak radiative corrections for* Z^0 *physics*. In G. Altarelli, R.Kleiss and C.Verzegnassi (eds), *"*Z^0 *physics at LEP 1"* CERN 89-08 Vol. 1 (1989) 7.

[6] M. Schmelling, Phys. Scripta **51** (1995) 683.

[7] D. Bardin et al., Z. Phys. **C44** (1989) 493; D. Bardin et al., Comp. Phys. Comm. **59** (1990) 303; D. Bardin et al., Nucl. Phys. **B351** (1991) 1; D. Bardin et al., Phys. Lett. **B255** (1991) 290; D. Bardin et al., CERN-TH 6443/92 (1992).

[8] M. Böhm and W. Hollik, *Forward-backward asymmetries*. In G. Altarelli, R.Kleiss and C.Verzegnassi (eds), *"*Z^0 *physics at LEP 1"* CERN 89-08 Vol. 1 (1989) 203.

[9] T. Sjöstrand, Comp. Phys. Comm. **82** (1994) 74.

[10] R. Field and R. Feynman, Nucl. Phys. **B136** (1978) 1.

[11] T. Sjöstrand, Int. Jour. of Modern Phys. **A3** (1988) 753.

[12] G. Marchesini and B. Webber, Nucl. Phys. **B310** (1988) 461.

[13] C. Peterson et al., Phys. Rev., **D27** (1983) 105.

[14] DELPHI Collaboration, P. Abreu et al., Z. Phys. **C73** (1996) 11.

[15] DELPHI Collaboration, P. Aarnio et al., Nucl. Instr. and Meth. **A 303** (1991) 233;
DELPHI Collaboration, P. Aarnio et al., Nucl. Instr. and Meth. **A 378** (1996) 57.

[16] P.A. Cherenkov, *"Visible Radiation Produced by Electrons Moving in a Medium with Velocities Exceeding that of Light"*, Physical Review **52** (1937) 378;
P.A. Cherenkov, C. R. Ac. Sci. U.S.S.R. **8**, (1934) 451;
P.A. Cherenkov, C. R. Ac. Sci. U.S.S.R. **12**, (1936) 413;
P.A. Cherenkov, C. R. Ac. Sci. U.S.S.R. **14**, (1937) 102;
P.A. Cherenkov, C. R. Ac. Sci. U.S.S.R. **14**, (1937) 105;
S.I. Wawilow, C. R. Ac. Sci. U.S.S.R. **8**, (1934) 457.

[17] I. Frank and Ig. Tamm, *"Coherent visible radiation of fast electrons passing through matter"*, Comptes Rendus (Doklady) de l'Académie des Sciences de l'URSS (1937) **XIV**, Nr. 3, 109-114.

[18] L. D. Landau and E. M. Lifshitz, *"Electrodynamics of Continuous media"*, **V.8** of Course of Theoretical Physics, Pergamon Press (1960).

[19] J. Séguinot and T. Ypsilantis, *"Photon-ionisation and Cherenkov Ring Imaging"*, Nucl. Instr. and Meth. **142** (1977) 377.

[20] E.G. Anassontzis et al., *"The Barrel Ring Imaging Cherenkov counter of DELPHI"*, Nucl. Instr. and Meth. **A 323** (1992) 351-362.

[21] W. Adam et al., *"The forward ring imaging Cherenkov detector of DELPHI"*, Nucl. Instr. and Meth. **A 338** (1994) 284-309.

[22] B.Erzen et al., Nucl. Instr. and Meth. **A433** (1999) 247-251.

[23] W.Adam et al., Nucl. Instr. and Meth. **A 371** (1996) 240-243.

[24] M.Battaglia and P.M.Kluit, *"The RIBMEAN Clustering Package for DELPHI RICHes"*, DELPHI-NOTE 96-133 RICH 90 (1996);
M.Battaglia and P.M.Kluit, Nucl. Instr. and Meth. **A 433** (1999) 252-256.

[25] E.Albrecht et al., Nucl. Instr. and Meth. **A 433** (1999) 47-58.

[26] DELPHI Collaboration: *"DELPHI event generation and detector simulation - User Guide"*, DELPHI Note 89-67 99 (1989).

[27] E. Schyns, *"NEWTAG -* $\pi, \mathrm{K}, \mathrm{p}$ *Tagging for DELPHI RICHes"* , DELPHI 96-103 RICH 89 (1996).
DELPHI Collaboration, P. Abreu et al., Eur. Phys. J. **C 5** (1998) 585-620
E. Schyns, Wuppertal University, PhD thesis WUB-DIS 96-22.

[28] G. Borisov, C. Mariotti, Nucl. Instr. and Meth. **A372** (1996) 181-187.

[29] The LEP/SLD Heavy Flavour Working Group, *"Electroweak Heavy Flavour Results presented at the 1999 Winter Conferences"*, LEPHF/99-01.
The LEP/SLD Heavy Flavour Working Group, *"Input parameters for the LEP/SLD Electroweak Heavy Flavour Results for Summer 1998 Conferences"*, LEPHF/98-01.
D. Abbaneo et al, Eur. Phys. J. C4 (1998) 2, 185.

[30] The LEP Collaborations, the LEP Electroweak Working Group and the SLD Heavy Flavour Group, *"A Combination of Preliminary Electroweak Measurements and Constraints on the Standard Model"*, CERN-PPE/99-15 (1999).

[31] ALEPH collaboration, R. Barate et al., Phys. Rep. 294 (1998) 1.

[32] Particle Data Group, The European Physical Journal **C3** (1998) 1.

[33] ARGUS collaboration, H. Albrecht et al., Z. Phys. **C62** (1994) 371.

[34] U. Flagmeyer, *"Eine genaue Bestimmung der Ladungsseparation: Systematische Untersuchung des Ein¤usses von Fragmentationseffekten und ihre Bescheibung durch Monte Carlo Modelle"*, Diploma thesis WUD 96-25 (1996).

[35] OPAL collaboration, R. Ackers et al., Phys. Lett. **B353** (1995) 595.

[36] DELPHI collaboration, P. Abreu et al., Phys. Lett. **B462** (1999) 425.

[37] DELPHI collaboration, P. Abreu et al., Z. Phys. **C67** (1995) 1.

[38] OPAL collaboration, K. Ackerstaff et al., Z. Phys. **C76** (1997) 387.

[39] DELPHI collaboration, P. Abreu et al., *"Measurement of the strange quark forward-backward asymmetry around the Z peak"*, CERN-EP 99-134 (1999), accepted by E. Phys. J. **C**.

[40] R. Fletcher, C.M. Reeves, *"Function minimization by conjugate gradients"*, Computer J., **7**, No.2 (1964) 149-154.

[41] A.I. Manevich and E. Boudinov, *"An ef£cient conjugate direction method without linear minimization"*, Preprint NIKHEF 99-001, submitted to Nucl. Instr. and Meth. **A**.

[42] R. Fletcher, *"A new approach to variable metric algorithms"*, Computer J., **13**, No.3 (1970) 317-322.

[43] F. James, *"MINUIT. Function Minimization and Error Analysis. Reference Manual. Version 94.1"*, CERN Program Library Long Writeup D506, CERN Geneva, Switzerland (1994).

[44] A.I. Manevich, P.I. Polyanchikov, *"Single-step method of conjugate directions"*, Izvestija of USSR Academy of Sciences. Technical Cybernetics (in Russian). (1984) Nr. 6, 41- 47. English version also exists.

Summary

This thesis describes the measurement of the s quark forward-backward asymmetry in Z^0 decays:

$$\mathrm{e}^+\mathrm{e}^- \to \mathrm{Z}^0 \to s\bar{s}$$

Parity, i.e. the symmetry w.r.t. space inversion, is violated in the electroweak interaction. This results in an asymmetric production of s and $\bar{s}$ quarks with respect to the direction of incidence of the initial electrons and positrons. The electroweak Standard Model quantitatively predicts this forward-backward asymmetry.

In the £rst chapter a general introduction to the Standard Model is given. The cross-section and forward-backward asymmetry of the fermion pairs at the LEP collider are presented. In the Standard Model one expects the same asymmetry for all down-type (or up-type) quarks. As the forward-backward asymmetries for b and c quarks have already been measured by experiments at LEP, the measurement of the s quark (a down-type quark) forward-backward asymmetry provides a test of the prediction that the down-type quark asymmetries are equal. It also shows how the forward-backward asymmetries measured at the Z^0 peak are sensitive through the electroweak corrections to the mass of the top (t) quark and to the mass of the hypothetical Higgs particle (predicted by the electroweak Standard Model).

The second chapter describes the DELPHI detector. The detector consists of many sub-detectors, which allow a precise measurement and identi£cation of particles produced in the $\mathrm{e}^+\mathrm{e}^-$ interactions. A short functional description of all detector components and their performances is given. It begins with describing the tracking system, then describes the measurement of the energy of particles, and concludes showing how these particles are identi£ed.

To identify charged particles the DELPHI detector is equipped with Cherenkov detectors, which are described in Chapter 3. The DELPHI Ring-Imaging Cherenkov detector system comprises the gaseous and liquid radiator RICHs in the central (barrel) and forward/backward regions. We give extensive details on the ring-£nding algorithm, which has been applied for the charged kaon identi£cation in this analysis.

Chapter 4 describes the selection of hadronic events in general and, in particular, the selection of the event sample that is enriched with s and $\bar{s}$ quarks produced from the Z^0 decay. Most of the heavy quark (b and c) events were removed from the sample in the barrel region using information from the vertex detector. This chapter also discusses the

identi£cation of high-energy kaons in the gaseous radiator of the forward and barrel RICHs. The charged kaons are identi£ed on a track-by-track basis. To be included in the sample it is required that the most energetic of the identi£ed kaons in the event has a momentum between 10 and 24 GeV/c.

Chapter 5 presents the experimental measurement of the forward-backward asymmetry for charged kaons A^K_{FB}. The charge of the kaon is used to separate the s quark from the $\bar{s}$ quark. The A^K_{FB} at a centre-of-mass energy of 91.2 GeV was measured to be :

$$\begin{aligned} A^K_{FB}(\text{barrel}) &= 0.0405 \pm 0.0049\,(\text{stat.}) \pm 0.0005\,(\text{syst.}) \\ A^K_{FB}(\text{forward}) &= 0.0390 \pm 0.0090\,(\text{stat.}) \pm 0.0009\,(\text{syst.}) \end{aligned}$$

The systematic error on this quantity is very small w.r.t. the statistical error.

From this measurement of A^K_{FB} the s quark forward-backward asymmetry A^s_{FB} is extracted. This is presented in Chapter 6. The dominant systematic error on A^s_{FB} comes from the uncertainty on the knowledge of how the charge and the direction of the kaon are related to that of the primary quark. A long discussion of various systematic sources is presented in this chapter. The result for the s pole asymmetry $A^0_{s\bar{s}}$, i.e. the asymmetry at the Z^0 pole, is :

$$A^0_{s\bar{s}} = 0.1008 \pm 0.0113\,(\text{stat.}) \pm 0.0040\,(\text{syst.})$$

The systematic error is about three times smaller than the statistical one. From this measurement we conclude that the asymmetry for s and b quarks ($A^0_{b\bar{b}} = 0.0990 \pm 0.0021$) are equal within the experimental errors, as it is predicted by the Standard Model. From $A^0_{s\bar{s}}$ we extract the electroweak mixing angle :

$$\sin^2\theta^{lept}_{eff} = 0.2321 \pm 0.0029$$

which is a very important parameter of the Standard Model because it is sensitive to the mass of the t quark and the mass of the hypothetical Higgs particle. The parity violating coupling of the s quark to the Z^0 (which is responsible for the violation of the parity symmetry in the electroweak interactions) was determined to be :

$$A_s = 0.909 \pm 0.102\,(\text{stat.}) \pm 0.036(\text{syst.}).$$

This value agrees well with the Standard Model expectation of 0.935. Finally the s quark forward-backward asymmetry A^s_{FB} is determined at three centre-of-mass energies.

In the last chapter we summarise and discuss the results obtained in this thesis. All results are in good agreement with the Standard Model predictions. It is the most precise measurement of the s quark forward-backward asymmetry and the parity violating coupling of the s quark A_s.

Samenvatting

Dit proefschrift beschrijft de meting van de s quark voorwaarts-achterwaarts asymmetrie in het verfal van de Z^0 :

$$\mathrm{e}^+\mathrm{e}^- \to \mathrm{Z}^0 \to s\bar{s}$$

Pariteit, de symmetrie m.b.t. ruimte inversie, is geschonden in de electrozwakke interactie. Dit levert een asymmetrische productie van s en $\bar{s}$ quarks op m.b.t. de richting van de botsing van de primaire electrons en positrons. Deze voorwaarts-achterwaarts asymmetrie wordt kwantitatief voorspeld door het electrozwakke Standaard Model.

In het eerste hoofdstuk wordt een algemene inleiding gegeven. De werkzame doorsnede en de voorwaarts-achterwaarts asymmetrie van het fermion paar bij de LEP versneller worden gepresenteerd. In het Standaard Model verwacht men dezelfde asymmetrie voor alle "down"-type (of "up"-type) quarks. De voorwaarts-achterwaarts asymmetrieën voor b en c quarks zijn al gemeten door de experimenten bij LEP, waardoor de meting van de s quark (een "down"-type quark) voorwaarts-achterwaarts asymmetrie een test levert van de voorspelling dat de "down"-type quark asymmetrieën gelijk zijn. Dit laat ook zien hoe de voorwaarts-achterwaarts asymmetrieën, gemeten bij de Z^0 piek, gevoelig zijn via de electrozwakke correctie voor de massa van het top (t) quark en voor de massa van het hypothetische Higgs deeltje (voorspeld door het electrozwakke Standaard Model).

Het tweede hoofdstuk beschrijft de DELPHI detector. De detector bestaat uit veel subdetectoren, die een nauwkeurige meting en identi£catie van de deeltjes, geproduceerd in de $\mathrm{e}^+\mathrm{e}^-$ interactie, mogelijk maken. Er wordt een korte functionele beschrijving gegeven van alle detector bestanddelen en hun uitvoeringen. Het begint met een beschrijving van het systeem van detectoren voor bepaling van geladen deeltjes, vervolgens beschrijft het de meting van de energie van deeltjes. Als laatste wordt er aangetoond hoe deze deeltjes worden geïdenti£ceerd.

Om geladen deeltjes te identi£ceren zijn in de DELPHI detector Cherenkov detectoren geïnstalleerd, die worden beschreven in hoofdstuk 3. Het DELPHI Ring-Imaging Cherenkov detector systeem bestaat uit RICHs met een gas en een vloeibare radiator in de centrale (barrel) en voorwaarts-achterwaartse gebieden. Wij geven uitgebreide details over het ringherken algoritme, dat werd gebruikt voor de geladen kaon identi£catie in deze analyse.

Hoofdstuk 4 behandelt de selectie van hadronische gebeurtenissen in het algemeen en, met name, de selectie van de verzameling gebeurtenissen die is verrijkt met s en $\bar{s}$ quarks geproduceerd in het Z^0 verval. De meeste van de zware quark (b and c) gebeurtenissen werden geëlimineerd uit de verzameling in het barrel gebied. Daarbij werd de informatie van de vertex detector gebruikt. Dit hoofdstuk behandelt ook de identi£catie van de hoge-energie kaonen in de gas-radiator van de voorwaartse en barrel RICHs. De geladen kaonen worden geïdenti£ceerd op een spoor-bij-spoor basis. Om te worden opgenomen in de verzameling is het nodig dat de meest energetische van de geïdenti£ceerde kaonen in de gebeurtenis een impuls heeft tussen 10 en 24 GeV/c.

Hoofdstuk 5 is gewijd aan de experimentele meting van de voorwaarts-achterwaarts asymmetrie voor geladen kaonen A_{FB}^{K}. De lading van het kaon is gebruikt om het s quark te scheiden van het $\bar{s}$ quark. De A_{FB}^{K} bij een zwaartepunts energie van 91.2 GeV werd bepaald als :

$$\begin{aligned} A_{FB}^{K}(\text{centraal}) &= 0.0405 \pm 0.0049\,(\text{stat.}) \pm 0.0005\,(\text{syst.}) \\ A_{FB}^{K}(\text{voorwaarts}) &= 0.0390 \pm 0.0090\,(\text{stat.}) \pm 0.0009\,(\text{syst.}) \end{aligned}$$

De systematische fout op deze grootheid is erg klein t.o.v de statistische fout.

Uit deze meting van A_{FB}^{K} is de s quark voorwaarts-achterwaarts asymmetrie A_{FB}^{s} bepaald. Dit wordt beschreven in hoofdstuk 6. De dominerende systematische fout op A_{FB}^{s} komt uit de onzekerheid over de kennis van de relatie tussen de lading en richting van het kaon met die van het primaire quark. Een uitvoerige discussie van verschillende bronnen van systematische effecten wordt gegeven in dit hoofdstuk. Het resultaat voor de s pole asymmetrie $A_{s\bar{s}}^{0}$, de asymmetrie bij de Z^0 pole, is :

$$A_{s\bar{s}}^{0} = 0.1008 \pm 0.0113\,(\text{stat.}) \pm 0.0040\,(\text{syst.})$$

De systematische fout is ongeveer drie keer zo klein als de statistische fout. Uit deze meting concluderen wij dat de asymmetriën voor s en b quarks ($A_{b\bar{b}}^{0} = 0.0990 \pm 0.0021$) gelijk zijn binnen de experimentele fouten, zoals is voorspeld door het Standaard Model. Uit $A_{s\bar{s}}^{0}$ bepalen wij de electrozwakke menghoek :

$$\sin^2\theta_{eff}^{lept} = 0.2321 \pm 0.0029$$

wat een heel belangrijke parameter van het Standaard Model is omdat die gevoelig is voor de massa van het t quark en voor de massa van het hypothetische Higgs deeltje. De pariteit-schendende koppeling van het s quark aan de Z^0 (die verantwoordelijk is voor de verstoring van de pariteit symmetrie in de electrozwakke interacties) werd bepaald als :

$$A_s = 0.909 \pm 0.102\,(\text{stat.}) \pm 0.036(\text{syst.}).$$

Dit resultaat komt goed overeen met de Standaard Model verwachting van 0.935. Als laatste is de s quark voorwaarts-achterwaarts asymmetrie bepaald bij drie zwaartepunts energieën.

De resultaten verkregen in dit proefschrift worden kort samengevat en besproken in het laatste hoofdstuk. Alle resultaten zijn in goede overeenstemming met de voorspellingen van het Standaard Model. Het is de meest nauwkeurige meting van de s quark voorwaarts-achterwaarts asymmetrie en de pariteit-schendende koppeling van het s quark A_s.

Acknowledgements

This thesis could not have been written without the support and effort of many people. First, it is my pleasure to thank all members of the DELPHI collaboration who contributed to this work in one way or another. Among them are my co-workers on the s-asymmetry analysis Fabio Cossutti, Kathy Huet and Peter M. Kluit. I enjoyed and greatly pro£ted from working in the DELPHI RICH group.

At NIKHEF the members of the computer group provided perfect computing and network support. Especially I would like to mention Paul Kuipers, who was always kind answering my ”simple” questions.

I am indebted to my co-promoter and supervisor Dr. P. M. Kluit for his valuable comment at all stages of the analysis. His clear intuition and keenness of observation always showed the way to the solution of many problems. I am grateful to Dr. J.J.M. Timmermans, who found time to read this manuscript and was generous with his critical gifts at a time when he was busy with other things. I want to express my gratitude to my promoter Prof. Dr. W. Hoogland for his valuable, critical suggestions for the improvement of this thesis.

Prof. Arkady I. Manevich introduced me into the world of optimization techniques. It was very pleasant to work with such a remarkable person and scientist.

I felt comfortable among my fellow Ph.D. students at NIKHEF. During the last three years the two of these fellows—Martijn Mulders, Ivo van Vulpen—and me were united by the same equation (1.2): Martijn was measuring the mass of the W particle, I was determining $\sin\bar{\theta}_W$ and Ivo is still busy discovering the Higgs particle.

I was very fortunate to have such good neighbours as Julia Shirokova and Alexander Shirokov. I could hardly stop Alexander's architectural imagination while he was making the Figures 3.5 and 3.6 and the cover of my thesis. If you meet a few English sentences in Appendix B, they are from Julia.

I want to thank my wife, Hanna, for her help, love and care during this restless time. She also translated the 'Summary' into the Dutch 'Samenvatting' thus proving her diploma ”Staatsexamen Nederlands als Tweede Taal Programma II” an invaluable investment. Finally I promise to play more often with my son, Ilya, as I was unjusti£ably busy with this writing.